THE MECHANICS OF CONTINUUM ROBOTS: MODEL–BASED SENSING AND CONTROL

By

Daniel Caleb Rucker

Dissertation

Submitted to the Faculty of the

Graduate School of Vanderbilt University

partial fullfillment of the requirements

for the degree of

DOCTOR OF PHILOSOPHY

in

Mechanical Engineering

December, 2011

Nashville, Tennessee

Approved:

Robert Webster III

Nabil Simaan

Michael Goldfarb

Michael Miga

George Cook

To my darling Sarah Beth,

who endured and encouraged me

throughout the creation of this dissertation.

Acknowledgments

Before beginning this dissertation, I want to first acknowledge and thank the many people that have made it possible by contributing their support in many different ways.

First, my advisor Bob Webster has invested an enormous amount of time and energy in me as his first graduate student. Without his brilliant intellectual guidance and support, I would have achieved far less in graduate school. Bob is one of the most patient and optimistic people I know, and his ability to humbly view situations from the perspective of others has made a significant impact on me. As a mentor and a friend, his selfless attitude and work-ethic are contagious, and I hope that I can follow his model of how to be an excellent researcher and teacher while simultaneously building meaningful relationships inside and outside of work.

I would like to thank my dissertation committee, Bob Webster, Nabil Simaan, Mike Miga, Michael Goldfarb, and George Cook, for patiently reading this work and giving me extremely valuable feedback as well as career advice. In addition, the National Science Foundation, the National Institutes of Health, and Intuitive Surgical, Inc. have all provided essential funding for the research, and many anonymous reviewers of my publications have contributed valuable insights that improved the content throughout this dissertation.

I give my heartfelt thanks to Myrtle, Jean, and Suzanne who have made my life much easier by helping with important logistical matters (morning coffee, travel arrangements, reimbursements, orders, registration) that an absent-minded person

like me has trouble juggling all at once. In addition to this, their many kind words to me and friendly conversations have been very encouraging.

I am grateful to the many other people who have directly contributed to the ideas and results in this dissertation. Noah Cowan, Greg Chirikjian, and Bryan Jones all contributed greatly to the work that became Chapter 3, and the things I learned from them inspired the further work in Chapters 4 and 5. I also thank my fellow laborers on the active cannula project, Jessica Burgner, Phil Swaney, and Hunter Gilbert. The work in Chapter 5 owes quite a bit to their hard work in developing theory, hardware, and software infrastructure for our active-cannula teleoperation system. Trevor Bruns, Jordan Croom, and Scott Nill also helped pioneer and test new ideas, built hardware, and gathered and processed much of the data that is presented herein.

In addition to those mentioned above, I would also like to thank all of the other members of the MED Lab (in no particular order): Ray Lathrop, Jenna Gorlewicz, Lou Kratchman, Byron Smith, Diana Cardona, Jadav Das, and Xianshi Xie. I have really enjoyed our interactions, whether digging into a problem, philosophizing about life, or having fun at movie nights and cookouts. You have defined life in the MED Lab by creating a stimulating work environment and being great friends. Others whom I want to thank for friendship, conversations, and guidance over the past few years include Kris Hatchell, Mark Jones, Robby Crouch, Mike Meyers, Eric Barth, Greg Walker, Tom Withrow, Bob Pitz, Nilanjan Sarkar, Rob Labadie, Paul Russel, and Kyle Weaver. I would like to thank all of the undergraduates I have had the privilege to know and work with, on both those on senior design and other projects.

Finally, I am especially thankful to my lovely wife Sarah Beth, who graciously

married me in the middle of my first semester of graduate school. Her gentle and creative spirit makes our home a haven that continually renews me. Many other members of my family, especially my parents Dan and Amy and my brother Jamin, have also been a source of much needed support and understanding, and my church family at Hillsboro, especially those in my life-groups, deserve many thanks for their continual prayers and encouragement throughout this process. Lastly, and most importantly, the credit for both my motivation and my ability to do this research should ultimately be given to God, the grand designer and the father of my lord Jesus, in whose kingdom I hope that this work may be of some small service.

Abstract

This dissertation addresses modeling, control, and sensing with continuum robots. In particular, two continuum robot architectures are studied: (1) concentric-tube designs, and (2) designs actuated by embedded wires, cables, or tendons. The modeling approaches and sensing and control methods developed are also applicable to many other varieties of continuum robot designs.

Concentric-tube continuum robot designs are also termed “active cannulas” because of their potential use as dexterous, needle sized manipulators for minimally invasive medical applications. These robots are composed of multiple pre-shaped tubes arranged concentrically, and their shape and pose are the result of elastic deformations, caused by interaction among the component tubes as well as external loads on the device. We derive two predictive models which describe this behavior using the principle of minimum potential energy and Cosserat-rod theory. The proposed models are each validated experimentally.

Tendon-driven continuum manipulators are also being developed for a variety of applications. The kinematics of these robots are also governed by elastic deformations resulting from tendon interactions with the backbone structure as well as external loading. We show that this behavior may be modeled by coupling the Cosserat-rod model with Cosserat-string models. This approach can be used to analyze designs in which the tendons are routed in general three-dimensional curves, as well as designs with precurved backbone structures, thus providing tools for the analysis and control of a large set of possible designs.

Model-based control of tendon-driven and concentric-tube robots is challenging because solving the kinematic and static models is often computationally burdensome. To address this, a we derive a method for obtaining Jacobians and compliance matrices for flexible robots which is computationally efficient enough to be used for real-time simulation and control. We then describe a Jacobian-based control algorithm and a deflection-based method for estimating applied forces on a flexible robot. The feasibility of these approaches is demonstrated in simulation and on robot hardware.

Contents

List of Figures

Chapter 1

Introduction

1.1 Motivation and Related Work

Continuum robots are an increasingly popular class of manipulators characterized by their ability to assume continuous curved shapes via a continuously bending, infinite-degree-of-freedom structure. They produce motion similar to the biological entities that are their inspiration, namely tentacles, trunks, tongues, snakes, and worms [40, 60, 85, 90]. Because of their compliant and dexterous structures, continuum robots offer a number of potential advantages over traditional rigid-link robots in certain applications, particularly those involving reaching through complex trajectories in cluttered environments, or where the robot must compliantly contact the environment along its length. As outlined in [90] and illustrated in Figure 1.1, continuum and hyper-redundant robots are being developed for many applications, including undersea manipulation [2], car painting, nuclear decontamination and reactor repair [14, 42], liquid transport [22], inspection of unstructured environments and pipes [56, 57, 80, 81, 87], and search and rescue [5, 86, 98].

A reviewed in [90], continuum robots can function as conventional medical tools, such as forceps [54], flexible needles [91], laparoscopic tools [57], endoscopes [41], arthroscopes [23], colonoscopes [59], laser manipulators [39], catheters [16, 55]. Con-

Figure 1.1: Many different biologically inspired continuum robot designs are being developed for medical applications, search and rescue, industrial inspection, nuclear decontamination, underwater, and outer space applications.

tinuum robots are also being developed as novel, multi-purpose, teleoperated devices for medical interventions. Examples of this approach include the multi-backbone robot of Simaan et al. [100] for applications in throat surgery, the hyperredundant cardiac manipulator of Choset et al. [26] for cardiac surgery, the tendon-driven catheter system of Salisbury et al. [15, 16], and the concentric-tube active cannula robot of Webster et al. [62, 65, 70, 92, 94] and Dupont et al. [27, 28, 72, 73].

Historically, the development of the first continuum robot designs arose from the study of hyperredundant, or serpentine designs which use a large number of discrete rigid links to approximate continuously curved shapes. Early designs include the Orm [83], and the tensor arm [2]. Pioneering work in this field was done by Hirose, and summarized in his book [40]. To plan configurations for hyperredundant, snake-like robot designs and control their motion, a "top down" approach was developed by Chirikjian and Burdick [19, 20] and subsequently adapted by several others using a variety of formulations for various purposes (see e.g. [35, 36, 43, 52]). This approach involves choosing an appropriate theoretical curve and then matching the (usually high-degree-of-freedom) physical robot to it. The properties of the curves themselves have often been based upon principles in continuum mechanics (such as minimum energy).

In contrast to hyper-redundant robots, many continuum robots have a relatively low number of *actuatable* degrees of freedom despite having a flexible structure capable of assuming a variety of continuous curves. In this case, a "bottom up" approach is often more appropriate. The goal here is to directly model the mechanics of a particular continuum robot structure in order to arrive at an accurate description of its forward kinematics and static deformation behavior. Examples of this approach include the work of Gravagne and Walker [33, 34, 37], Jones, Rahn, Trivedi, et al. [45, 49, 85], Camarillo, Salisbury et al. [15, 16], and Simaan et al. [75, 99, 102] The useful "top-down" versus "bottom up" categorization was suggested and defined in the book [74].

In this dissertation, we take the bottom-up approach, formulating models based on elastic energy and classical rod mechanics for two popular types of extrinsically actuated continuum manipulators, namely concentric-tube "active cannulas" and robots with flexible backbones actuated by embedded tendons. We review the background and related work for modeling these two particular classes in the following subsections.

1.1.1 Concentric-Tube Continuum Robots

Concentric-tube continuum robots, also called active cannulas due to their promise in interventional medicine, use the geometry and elastic interaction of precurved concentric tubes to achieve a wide variety shaft curves and end effector poses. As shown in Figure 1.2, the shape of the cannula's telescoping backbone can be changed

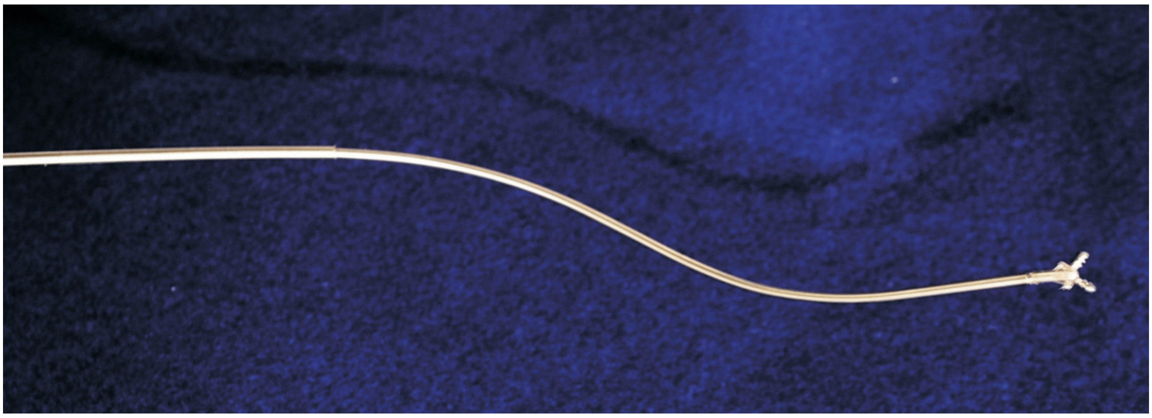

Figure 1.2: A prototype concentric-tube robot (active cannula) made of precurved superelastic Nitinol tubes. The telescoping tubes can be independently rotated and translated to achieve motion.

by axially rotating and translating each individual tube at its base. This thin, flexible, continuum robot design is mechanically simple, and has the potential ability to reach into confined or winding environments [94]. Using precurved component tubes may potentially enable a larger variety of shapes at smaller diameters than is possible with continuum robots actuated by support disks with tendon wires [23,38], elastic sleeves with embedded tendons [16], flexible push rods [76], or pneumatic actuators [18,46].

These characteristics have led to many proposed medical applications at the “meso-scale” ($\approx$ 0.1-100 mm) that require thin, dexterous manipulators, including minimally invasive surgical procedures. Specific applications for which active cannulas have been proposed include accessing the lung via the throat [93,94], transgastric surgery [92], fetal procedures [31], steering needles embedded in tissue [29,51,72], cardiac procedures [72], and transnasal skull base access [92]. An overview of several specific ways active cannulas might be used in medicine is given in [89]. It is also possible in principle to construct very small active cannulas which may be useful in cell manipulation [30, 48, 79] and other micro-surgical applications.

The idea of making a robot from counter-rotated, pre-curved concentric tubes was introduced relatively recently. Loser et al. [51] developed a steerable needle composed of two fully overlapping precurved cannulas whose bases rotate (but do not translate) relative to one another to change needle curvature. Daum [24] patented a deflectable needle assembly in which a curved “catheter” is deployed through a rigid outer cannula.

Related Kinematic Modeling Work

Despite its mechanical simplicity, finding a sufficiently accurate representation of the forward kinematic mapping (robot shape as a function of axial rotations and translations of the component tubes) for active cannulas has been a challenge, due to the complexity of the elastic interactions between the component tubes. Solving this problem is a necessary first step towards the practical implementation of concentric-tube robots and the subject of the first half of Chapter 3 of this dissertation.

The modeling frameworks that exist today have been developed in parallel by several groups. The simplest possible model of an active cannula, called a “Curved Multi Tube” (CMT) by Furusho et al. [31, 82], makes the assumption that the outermost tube in any given section of the robot has infinite stiffness compared to all tubes within it. Webster et al. [92] and Sears and Dupont [72] provided initial beam mechanics models that accounted for bending interaction between the tubes and thereby achieved better accuracy. The importance of torsional deformation was also recognized and initially modeled in straight sections of the device [93, 94]. Assuming piecewise-constant precurvature and torsional rigidity in curved sections, these models describe the robot's backbone shape by balancing moments between component tubes. Under these assumptions, the resulting robot shape becomes a series of mutually tangent circular arcs.

The recent modeling work by Webster et al. [92–94] also demonstrates the critical role of torsion in the stored elastic energy landscape, as well as in accurately predicting tip position. For the specific experimental setup reported in [94], this model predicts the location of the cannula end point with an average accuracy of 3.0 mm. However, the difference between predicted and experimental cannula tip positions was not uniform over the workspace, and was generally worse (up to 8.76 mm) in configurations where the torsional strain is highest. This suggests that, although neglected by this "lumped-parameter" model, additional torsional deformation in the curved sections may be a significant phenomenon that should be modeled. This is one motivation for the generalized forward kinematics model we present in the first half of Chapter 3 which accounts for both bending and torsion throughout a multi-tube active cannula. This model has the added benefit of being able to describe robots which use of tubes with general precurved shapes.

Related Static Modeling Work

While some of the applications listed above, such as manipulating a fiber optic laser in the lung [61], may be approachable with the free-space kinematic model developed in the first half of Chapter 3 that does not include external loading, in many more foreseeable applications it will be useful for the cannula to intentionally manipulate tissue by retracting it, cutting it, dissecting it, traveling through it like a needle, etc. Furthermore, as the cannula approaches the area in which it is to work, it is likely that tissue will contact it at one or more points along its shaft. Gravity can also cause some (albeit typically small) deflection in an active cannula. To enable accurate control of cannula position and applied forces under these conditions, it is essential to have a model that describes cannula shape under externally applied point and distributed forces and moments.

The value of modeling external loading has recently been demonstrated in larger-scale pneumatically actuated continuum robots where the robot sags significantly under the self-weight of the arm. Trivedi et al. used geometrically exact Cosserat rod theory to describe the shape of the OctArm under load, reducing model errors from 50% to 5% [84]. With respect to small-scale continuum robots for medical applications, Xu and Simaan modeled multi-backbone robot statics and accounted for strategies for shape restoration after the application of a tip load [101]. They have also have recently demonstrated intrinsic force sensing with this robot, and applied it to palpation tasks [102].

Our purpose in the last half of Chapter 4 is to extend the free-space forward kinematic model of the first half of Chapter 3 to describe the shape of an concentric-tube robots under external loading. While this work draws upon similar geometrically exact rod theory as has been used in the work cited earlier in this section, the concentric precurved tube design presents a fundamentally different problem because there are many interacting elastica to consider, rather than just one. While concentric tubes do share a common backbone shape, each can undergo torsion independent of the others, which precludes the use of any of existing robot models.

The extended model we develop is a necessary prerequisite to future development in areas such as design based on compliance, manipulation of objects, and intrinsic force sensing and control of the robot when it is interacting with tissue.

1.1.2 Tendon-Actuated Continuum Robots

The shape of most continuum robots is not only affected by actuation, but also externally applied forces and moments. A recent area of research has focused on developing kinematic models which consider both actuation and external loading. Such models have been derived for continuum robots with pneumatic actuation [84, 97], multi-backbone continuum robots [101, 102], and concentric-tube robots (see Chapter 3, and [62]).

In Chapter 4, we derive and validate such a model for the broad class of continuum robots actuated by tendons. This widely employed class of continuum robot utilizes an elastic structure (which we will often refer to as a "backbone") actuated by tendons which pass through hollow channels in the elastic structure. Example elastic structures include a flexible tube with tendons embedded in its walls [16], and an elastic rod with discs affixed along its length containing holes through which tendons pass (see e.g. [14, 33] among many others). The ends of the tendons are attached to the robot at various points, enabling base-mounted actuators to bend the backbone by pulling on the tendons.

Describing robot shape using mechanics-based models has been the subject of much prior research. Early work by Chirikjian and Burdick [17, 19, 20], used continuum models to describe and control hyperredundant robots. Recent continuum robot modeling has focused on continuously flexible structures acted on by a variety of actuators or force/torque transmission mechanisms. For tendon-actuated robots, the consensus result is that when the tendons are tensioned, the backbone assumes a piecewise constant-curvature shape. This yields analytically simple kinematics and has been experimentally demonstrated on several different robots (e.g. [16]. Li and Rahn [49] investigated this issue explicitly, using nonlinear elastica theory to determine bounds on the tendon support height and spacing such that a constant curvature approximation is valid for robots in the absence of external loading.

In addition to free space kinematic modeling, some results exist for describing the shape of tendon-actuated continuum robots under external loads. Early theoretical work toward elastica dynamics with embedded tendons is that of Davis and Hirschorn [25]. Gravagne et al. provide a comprehensive energy-based model in [32, 33, 37] for the statics and dynamics of a planar continuum robot with in-plane loads. Cosserat rod theory has also recently shown promise as a general tool for describing the spatial deformations of other (non-tendon-based) continuum designs [62,84]. Jones et al. [44] applied Cosserat theory to achieve real-time kinematics computations for tendon-actuated robots under external loads, based on modeling tendon actuation as a single point moment applied to the backbone where each tendon is attached.

In this chapter, we extend previous work on the Cosserat-rod approach by taking into account not only the attachment point moment, but also the attachment point force and the distributed wrench that the tendon applies along the length of the

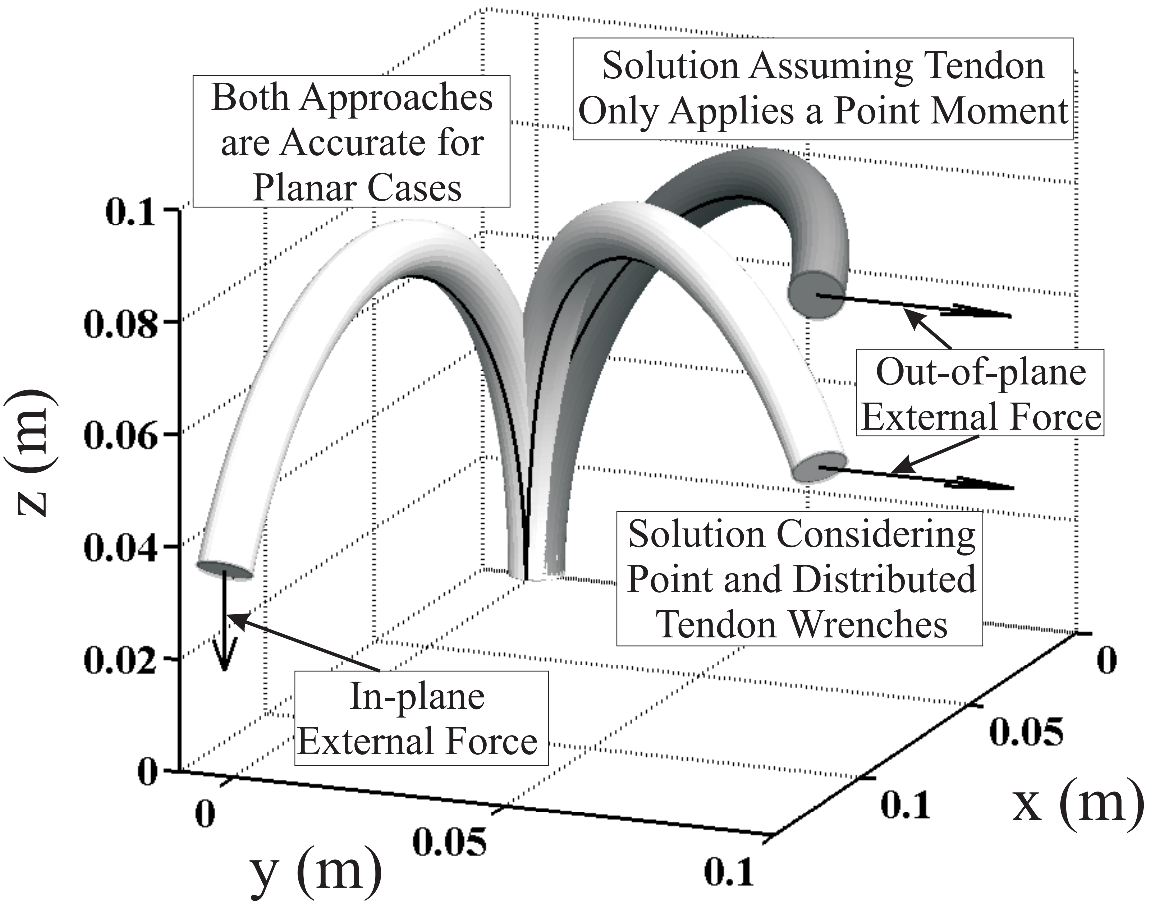

Figure 1.3: Simulations of a continuum robot with a single, straight, tensioned tendon with in-plane and out-of-plane forces applied at the tip. These plots illustrate the difference between the model proposed in Chapter 4, which includes distributed tendon wrenches, and the commonly used point moment approximation. For planar deformations and loads, the two models differ only by axial compression (which is small in most cases). However, for out of plane loads, the results differ significantly, and including distributed wrenches enhances model accuracy.

backbone. Our approach couples the classical Cosserat string and rod models to express tendon loads in terms of the rod's kinematic variables. We illustrate the difference between the predictions of this new coupled model and the point moment model for an example case with out of plane loads in Figure 1.3, and provide an experimental comparison of the two approaches in the experimental section of Chapter 4.

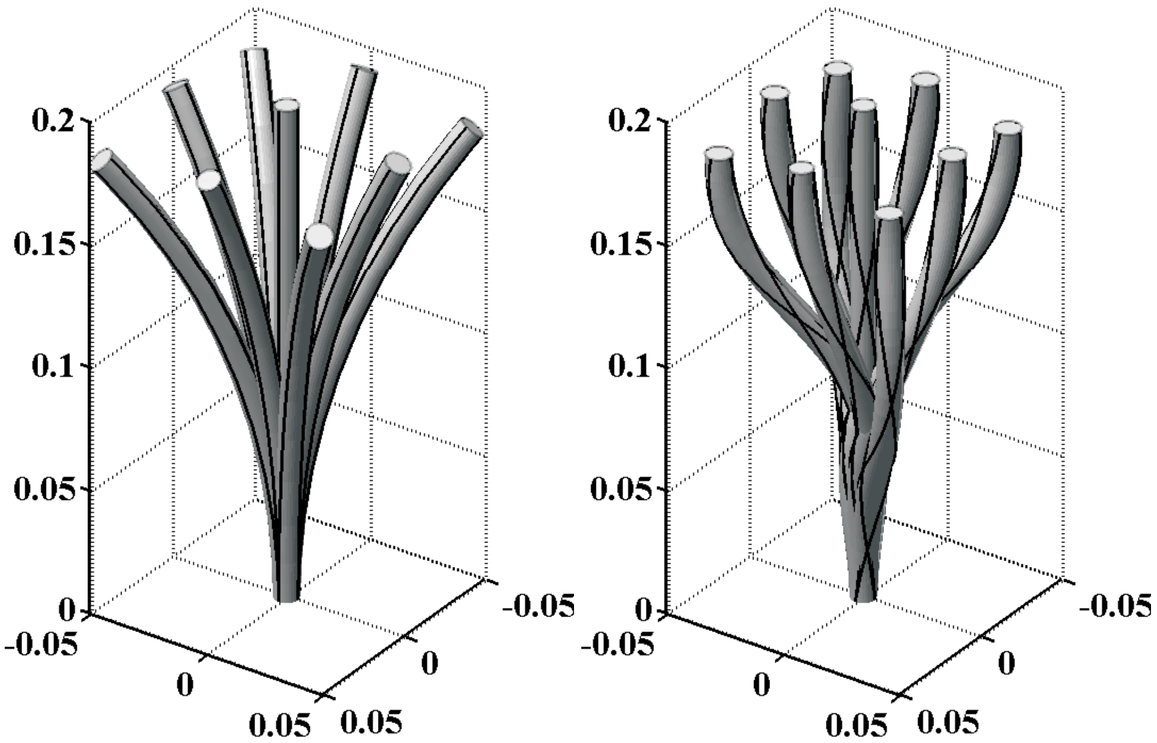

Figure 1.4: An example of robot shape/workspace modification using curved tendons. (Left) A robot with four straight tendons spaced at equal angles around its periphery. (Right) A similar robot with four helical tendons that each make one full revolution around the shaft. The two designs differ significantly in tip orientation capability, and the helical design may be better suited to e.g. a planar industrial pick and place task.

A further advantage of the coupled model is that it enables use of tendon routing paths that are general curves in space (prior designs have routed tendons in straight paths along the robot, parallel to the backbone axis). This expands the design space and the set of shapes achievable for tendon-actuated robots. Figure 1.4 illustrates how this can be useful for reshaping the workspace of a single-section robot, reorienting the tip. This illustrative example could conceivably be valuable in industrial pick and place tasks where objects to be manipulated lie in a plane. Another example of the usefulness of general tendon routing is the cochlear implant of Simaan et al. [77], which uses a single curved tendon to control the shape of the implant during insertion, with the aim of reducing insertion forces and thereby trauma to the cochlea.

The ability to have a single section of the robot bend into variable curvature shapes is an important extension in the capabilities of continuum robots and is enabled by generally routed tendons. The model we derive in Chapter 4 provides the theoretical framework for design and control of robots actuated in this way.

1.1.3 Kinematic Control of Continuum Robots

In the absence of external loading, many continuum robot architectures will assume an approximately piecewise-constant curvature shape [90], as indicated by modeling results in [16, 49]. In these cases, the robot's forward kinematic model and Jacobian can often be written in closed form (see for example [8, 38, 45, 94, 102]).

However, when external loading is considered, and/or the robot design is such that the piecewise-constant curvature result does not hold, the forward kinematics problem requires the numerical solution of a set of nonlinear differential equations subject to multi-point boundary conditions. When this is the case (e.g. for the robot models presented in Chapters 3 and 4 of this dissertation), computing the robot's Jacobian becomes significantly more challenging.

The model equations themselves are often solved using a shooting method [28, 44, 62, 70, 84], and it is possible to approximate the Jacobian via finite differences by solving the boundary value problem multiple times. However, the computational intensiveness of this approach is often too high for real-time control.

Another approach that has previously been applied to concentric-tube robot control is to pre-computing a large number of forward kinematic solutions spanning the configuration space of a particular robot. Then, it is possible to construct a function which approximates the forward kinematic mapping dataset and which can be rapidly solved to obtain inverse kinematics. This approach has been successfully demonstrated in [28], but is limited to the specific robot for which the workspace was sampled, requires *a priori* specification of any points of interest along the robot one may wish to consider, and does not account for external loading, or multiple forward kinematics solutions.

The limitations of the two approaches outlined above highlight the need for the work that we undertake in Chapter 5. We present a method for obtaining the Jacobian and compliance matrix directly from the model equations of a general continuum robot with minimal computational burden. Our approach yields an arc length parametrized Jacobian useful for controlling any point (or many of them simultaneously) along the robot, and also explicitly takes into account external loading. As further demonstrated in Chapter 5, this approach enables teleoperation in a real-time setting without pre-computation.

Previous work related to the method we present in Chapter 5 includes Gravagne and Walker's formulation for the Jacobian and compliance matrix of a planar continuum robot where the actuators provide a set of discrete or continuous torques along the length [37]. Jones et al. [44] also suggested a method for obtaining the manipulator Jacobian for a tendon-actuated robot under external loading, by using a Cosserat-rod-based model and applying finite differences to an associated initial value problem, to approximate the Jacobian.

In Chapter 5, we extend both of these approaches to include non-planar continuum robots of various architectures and actuation strategies, and provide exact equations to calculate the Jacobian, requiring no finite difference approximations. We then demonstrate use of this Jacobian to implement real-time inverse kinematics solutions for concentric-tube robots via a damped-least-squares algorithm.

The latter half of Chapter 5 addresses force sensing using the robot's compliance matrix. This work supports the findings of recent research that has shown that flexible continuum robots can also be used as force senors. In [100, 102], Xu and Simaan introduced the concept of intrinsic force sensing for continuum robots, demonstrating that by sensing the axial actuation loads on their multi-backbone continuum robot, certain components of an end-effector wrench could be determined. Additionally, work by Bajo and Simaan used the relative position of points on the robot shape to determine the contact location [9].

Here we extend the current body of research on intrinsic force sensing by considering the problem of shape-based load estimation from a probabilistic perspective. That is, given noisy measurements of the robot's shape and/or end effector pose, we aim to estimate the most likely set of loads on the robot and quantify the uncertainty in that estimation. Our approach is based on applying the popular Extended Kalman Filter (EKF) algorithm to the problem of estimating the applied forces and the pose of the end-effector simultaneously. Simulation results indicate that this approach is feasible if both the sensor accuracy and model accuracy are high, even though the compliance matrix of a typical continuum robot is ill-conditioned.

1.2 Dissertation Contributions

Free-Space Kinematic Modeling Concentric-Tube Robots:

In the first half of Chapter 3, we obtain a new model for the forward kinematics of concentric-tube robots, by deriving a general coordinate-free energy formulation, leading to a set of differential equations that describes the shape of an an active cannula. The model accounts for bending and torsional strain throughout the robot, and non-constant precurvature and stiffness of the component tubes. We derive an analytical solution for the 2-tube, constant-precurvature case, and demonstrate that the resulting cannula shape is non-circular. The experimental contribution of this chapter is a demonstration that the new modeling framework can reduce model prediction error by 82% over the prior bending-only model, and 17% over the prior transmissional torsion model in a simple set of experiments with a prototype active cannula.

The first half of Chapter 3 contains results which were published at the IEEE RAS/EMBS International Conference on Biomedical Robotics and Biomechatronics (BioRob) in 2008 [64], and at the IEEE International Conference on Robotics and Automation (ICRA) in 2009 [71], as well as in IEEE Transactions on Biomedical Engineering [65] and the International Journal of Robotics Research [70]. Some of the results in this chapter were independently and concurrently developed by Dupont et al. [27,28].

Static Modeling of Concentric-Tube Robots under External Loads:

The contributions of the latter half of Chapter 3 are (1) an extension of the classical, geometrically exact Kirchoff rod theory from one rod to many precurved concentric tubes under arbitrary external point and distributed wrench loading, and (2) experimental validation of the accuracy of the model for a specific prototype robot under point and distributed loading. This work generalizes the free-space kinematic model by additionally accounting for the effect of external loading on a general robot.

The latter half of Chapter 3 contains results which were published at the IEEE International Conference on Robotics and Automation in 2010 [63], and in IEEE Transactions on Robotics [62].

Static and Dynamic Modeling of Tendon-Actuated Continuum Robots:

In Chapter 4 we provide a new Cosserat-rod-based model for the deformation of tendon-actuated continuum robots under general external point and distributed wrench loads. This model describes both point and distributed tendon loads in a geometrically exact manner for large 3D deflections. Other specific contributions include the ability to accommodate general tendon routing, and an additional model describing the distributed dynamics of tendon actuated robots. Our experimental contribution in this chapter is a validation of accuracy of the static model on a physical prototype with straight, helical, and polynomial tendon paths, subject to both distributed and point loads.

Chapter 4 contains results presented at the International Symposium on Experimental Robotics in 2010 [66], and in IEEE Transactions on Robotics [69].

Kinematic Control and Force Sensing with Continuum Robots:

Chapter 5 demonstrates two of the many practical uses of the models developed in Chapters 3 and 4. Specific contributions of this work include (1) an efficient method for obtaining an arc length parametrized Jacobian and compliance matrix for general continuum robots under applied loads, (2) demonstration of Jacobian-based kinematic control of a concentric-tube robot in simulation, and (3) demonstration of probabilistic, shape-based force sensing for a continuum robot in simulation. Chapter 5 contains results published at the IEEE International Conference on Robotics and Automation in 2011 [67], and at the IEEE Conference on Intelligent Robots and Systems in 2011 [68].

Chapter 2

Mathematical Framework and Notation

Chapters 3, 4, and 5 all rely on a common geometric framework to describe the shape of the elastic structures that comprise continuum robots. These chapters also draw heavily on classical solid mechanics principles and Cosserat-rod theory, using many methods and nomenclature from chapters 4 and 8 of Antman's work on nonlinear elasticity [3], while making use of some concise kinematic notation familiar to roboticists (see [53]). In this chapter, we give a concise overview of the frameworks used throughout this dissertation. The symbols used are summarized in a nomenclature section at the end of the chapter.

2.1 The Kinematics of Rods

2.1.1 Geometric Representation of Rods

We define the shape of a rod or tube as a parametric Cartesian curve in space $\boldsymbol{p}(s) \in \mathbb{R}^3$ paired with an orthonormal rotation matrix expressing the material orientation, $R(s) \in \mathrm{SO}(3)$ ($\mathrm{SO}(3)$ is the special orthogonal group in three dimensions, $\mathrm{SO}(3) = \left\{R \in \mathbb{R}_{3x3} \mid R^T R = I, \text{ and } \det(A) = 1\right\}$). Both position and orientation are functions of a scalar reference length parameter s over some finite interval, say $s \in [0 \ \ell]$. Thus, a mapping from s to a homogeneous rigid-body transformation,

$g(s) \in \mathrm{SE}(3)$, describes the entire rod:

$$g(s) = \begin{bmatrix} R(s) & \boldsymbol{p}(s) \\ \mathbf{0}^T & 1 \end{bmatrix}, \tag{2.1}$$

where SE(3) is the special Euclidean group in three dimensions. We will often refer to $g(s)$ as a "frame" hereafter.

In the following chapters, we are primarily concerned with how the shape of a rod $g(s)$ changes from some initial reference state to a final deformed shape as the result of external forces or constraints as shown in Figure 2.1. Thus, we begin by defining the initial reference shape,

$$g^*(s) = \begin{bmatrix} R^*(s) & \boldsymbol{p}^*(s) \\ \mathbf{0}^T & 1 \end{bmatrix}.$$

Note that we will use the * symbol to denote variables associated with the reference state. It will often be convenient for the parameter s to represent the arc length along the reference curve $\boldsymbol{p}^*(s)$, but this is not required.

While the curve of the rod in its undeformed reference state defines $\boldsymbol{p}^*(s)$, the reference orientation $R^*(s)$ can be assigned somewhat arbitrarily. However, one can establish conventions governing the assignment of reference orientations such that the mapping from $R^*(s)$ to $R(s)$ has an easily interpretable meaning in terms of material strains. In this work we choose to adopt such a convention for this purpose. We assign reference orientations such that

$$R^*(s)\boldsymbol{e}_3 = \frac{\dot{\boldsymbol{p}}^*(s)}{\|\dot{\boldsymbol{p}}^*(s)\|}, \tag{2.2}$$

where $\dot{\boldsymbol{p}}^*(s) = \frac{d\boldsymbol{p}^*(s)}{ds}$. (Note that we use the $\dot{}$ symbol to denote differentiation with respect to s throughout this dissertation, with the exception of Chapter 5, where we

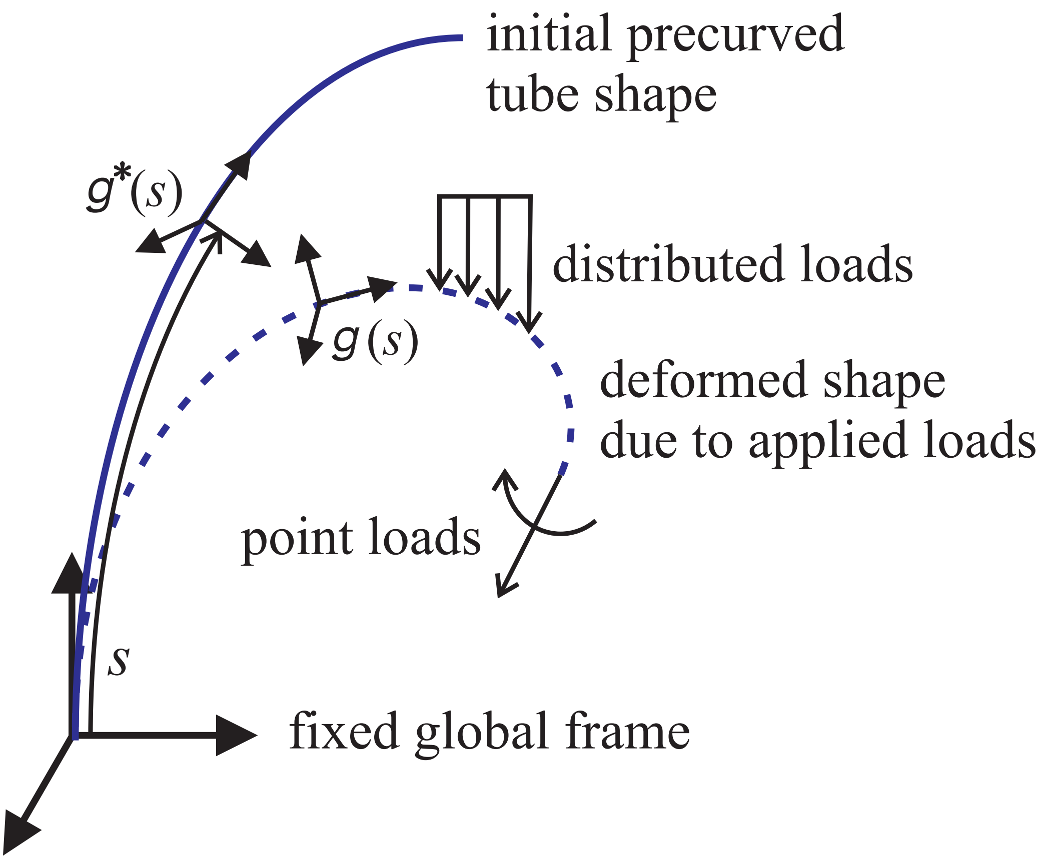

Figure 2.1: The shape of a rod structure in its reference state is defined by a parameterized frame along the rod's length. The rod then deforms to a new shape defined by a new set of frames as the result of external forces.

use $'$). Also $\boldsymbol{e}_1$, $\boldsymbol{e}_2$, and $\boldsymbol{e}_3$ are used for the standard basis vectors $[1\ 0\ 0]^T$, $[0\ 1\ 0]^T$, and $[1\ 0\ 0]^T$, respectively) The physical interpretation of this constraint is that the local z axis of the reference frame points along the tangent of the reference curve.

The convention above, defines the only the z axis of the reference orientation. If the rod or tube has a cross section which is not radially symmetric, it is sometimes convenient to make the x and y axes of each reference frame align with the principal axes of the cross section (note that principal axes are orthogonal by definition). Otherwise, one could use the Frenet-Serret convention which provides closed form equations that can be used to generate frames as long as $\boldsymbol{p}^*(s)$ is twice differentiable and nonzero. In this convention, one axis is aligned with the plane of geometric curvature at s. Perhaps more intuitive, but less analytically simple are Rotation Minimizing, or Bishop frames [11], which propagate along s without undergoing any instantaneous rotation about the tangent axis, as reviewed in [21].

2.1.2 Differential Geometry

Following the notation in [53], we recognize that, in general, $R(s)^T \dot{R}(s) \in \mathfrak{so}(3)$ is a 3×3 skew symmetric matrix ($\mathfrak{so}(3)$ is the Lie algebra of Lie group SO(3)). Since the set of skew-symmetric matrices is isomorphic to $\mathbb{R}^3$, we define a bijective mapping from $\mathbb{R}^3$ to $\mathfrak{so}(3)$ using the $\widehat{\ }$ symbol as follows. For $\boldsymbol{u} = [u_x\ u_y\ u_z]^T \in \mathbb{R}^3$,

$$\widehat{\boldsymbol{u}} = \begin{bmatrix} 0 & -u_z & u_y \\ u_z & 0 & -u_x \\ -u_y & u_x & 0 \end{bmatrix} \tag{2.3}$$

The inverse operation, denoted by $^\vee$, maps $\mathfrak{so}(3)$ to $\mathbb{R}^3$, so that $\widehat{\boldsymbol{u}}^\vee = \boldsymbol{u}$.

Similarly, $g(s)^{-1}\dot{g}(s) \in \mathfrak{se}(3)$ (the Lie algebra of Lie group SE(3)) can be parameterized by an element of $\mathbb{R}^6$. Following the convention of [53], we overload the $\widehat{\ }$ and $^\vee$ notation to also represent the isomorphic mapping from $\mathbb{R}^6$ to $\mathfrak{se}(3)$ and its inverse, respectively. Thus, for $\boldsymbol{\xi} = [v_x\ v_y\ v_z\ u_x\ u_y\ u_z]^T \in \mathbb{R}^6$,

$$\widehat{\boldsymbol{\xi}} = \begin{bmatrix} 0 & -u_z & u_y & v_x \\ u_z & 0 & -u_x & v_y \\ -u_y & u_x & 0 & v_z \\ 0 & 0 & 0 & 0 \end{bmatrix}, \tag{2.4}$$

and the inverse operation, denoted by $^{\vee}$, maps $\mathfrak{se}(3)$ to $\mathbb{R}^6$, so that $\widehat{\boldsymbol{\xi}}^{\vee} = \boldsymbol{\xi}$.

Thus, if one has a parameterized frame, $g(s)$, a twist vector can be obtained representing the rates of change of $g(s)$ with respect to s expressed in coordinates of $g(s)$ (body frame coordinates),

$$\boldsymbol{\xi}(s) = [v_x\ v_y\ v_z\ u_x\ u_y\ u_z]^T = \left(g^{-1}(s)\dot{g}(s)\right)^{\vee},$$

The first three components of $\boldsymbol{\xi}$, form a vector of linear rates of change, $\boldsymbol{v} = [v_x\ v_y\ v_z]^T$. The last three components of $\boldsymbol{\xi}$, form a vector of the angular rates of change $\boldsymbol{u} = [u_x\ u_y\ u_z]^T = \left(R^T\dot{R}\right)^{\vee}$.

Similarly, if one knows the "body frame" twist vector $\boldsymbol{\xi}(s)$, and an initial frame $g(0)$ then the remaining frames can be obtained by integrating the differential equation

$$\dot{g}(s) = g(s)\widehat{\boldsymbol{\xi}}(s), \tag{2.5}$$

or equivalently, by integrating the pair of equations

$$\boldsymbol{p}(s) = R(s)\boldsymbol{v}, \quad \dot{R}(s) = R(s)\widehat{\boldsymbol{u}}(s). \tag{2.6}$$

Obtaining $g(s)$ from $\boldsymbol{\xi}(s)$ via (2.5) or (2.6) is not trivial. If $\boldsymbol{\xi}(s)$ happens to be constant with respect to s, then a closed form solution exists via the matrix exponential,

$$g(s) = g(0)e^{\widehat{\boldsymbol{\xi}}s},$$

which can be computed using Rodrigues' formula. However, in the general case one usually has to resort to numerical integration to obtain $g(s)$ from $\xi(s)$. We discuss this issue and others in Section 2.2.5

2.1.3 Reference Frames and Reference Twists

As a consequence of our framing convention which assigns the reference frame z axis tangent to the reference curve, the associated reference twist $\boldsymbol{\xi}^*(s)$ will always have a certain form. Combining (2.2) and (2.6), we see that $\boldsymbol{v}^* = [0\ 0\ \ \|\dot{\boldsymbol{p}}^*(s)\|]^T$. Thus, if we choose to use the arc length of the reference curve as our parameter s, then $\boldsymbol{v}^* = [0\ 0\ 1]^T$.

As an example, in the simple case where the reference curve of a cylindrical rod is a straight line given by $\boldsymbol{p}^*(s) = [0\ \ 0\ \ s]^T$, we could set the reference orientation to identity, $R^*(s) = I$. Then the reference twist would have $\boldsymbol{v}^*(s) = [0\ \ 0\ \ 1]^T$, and $\boldsymbol{u}^*(s) = [0\ 0\ 0]^T$.

If the reference curve is a circular arc of radius r, given by $\boldsymbol{p}^*(s) = [0\ \ \ r(\cos(s) - 1)\ \ \ r\sin(s)]^T$, then we could assign the reference orientations as

$$R^*(s) = \begin{bmatrix} 1 & 0 & 0 \\ 0 & \cos(s) & -\sin(s) \\ 0 & \sin(s) & \cos(s) \end{bmatrix}.$$

Then, we find that the reference twist is composed of $\boldsymbol{v}^*(s) = [0\ 0\ r]^T$, and $\boldsymbol{u}^*(s) = [1\ 0\ 0]^T$.

Alternatively, we could re-parameterize $\boldsymbol{p}^*(s)$ such that s represents the arc length,

$\boldsymbol{p}^*(s) = [0 \;\; r(\cos(s/r) - 1) \;\; r\sin(s/r)]^T$. Then the orientation could be

$$R^*(s) = \begin{bmatrix} 1 & 0 & 0 \\ 0 & \cos(s/r) & -\sin(s/r) \\ 0 & \sin(s/r) & \cos(s/r) \end{bmatrix},$$

and the resulting reference twist would have $\boldsymbol{v}^*(s) = [0\ 0\ 1]^T$, and $\boldsymbol{u}^*(s) = [\frac{1}{r}\ 0\ 0]^T$.

2.1.4 The Kinetic Analogy

We note that in the kinematic formulation above, one can make the following analogy to rigid body motion: as a "body frame" angular velocity $\boldsymbol{\omega}$ describes how a rotation matrix $R(t)$ changes with respect time [53], so a local curvature vector $\boldsymbol{u}$ describes how a rotation $R(s)$ changes with respect to the arc length of the rod. Thus, the expressions for the elastic energy stored in a deformed rod are of the same form as those for the kinetic energy of a tumbling rigid body. This is termed Kirchoff's kinetic analogue, as discussed in [47]. This analogy may be helpful for those with experience in robot dynamics to gain intuition about the models developed in this dissertation.

2.2 The Mechanics of Rods

2.2.1 Equilibrium Laws

Following [3], we give the derivation of the classic equilibrium equations for a Cosserat rod as follows. Consider an arbitrary section from c to s as shown in Figure 2.2. The internal forces and moments that the material of $(s, \ell]$ exerts on $[c, s]$ are denoted by the vectors $\boldsymbol{n}(s)$ and $\boldsymbol{m}(s)$ respectively. Similarly, the material of $[c, s]$ exerts $\boldsymbol{n}(c)$ and $\boldsymbol{m}(c)$ on the material of $[0, c)$. Summing the forces on $[c, s]$ and the moments on $[c, s]$ about the origin of the global frame, we obtain the conditions of static equilibrium.

$$\boldsymbol{n}(s) - \boldsymbol{n}(c) + \int_c^s \boldsymbol{f}(\sigma) d\sigma = \boldsymbol{0}, \tag{2.7}$$

$$\begin{aligned} \boldsymbol{m}(s) + \boldsymbol{p}(s) \times \boldsymbol{n}(s) - \boldsymbol{m}(c) - \boldsymbol{p}(c) \times \boldsymbol{n}(c) \\ + \int_c^s \left(\boldsymbol{p}(\sigma) \times \boldsymbol{f}(\sigma) + \boldsymbol{l}(\sigma)\right) d\sigma = \boldsymbol{0}, \end{aligned} \tag{2.8}$$

where $\boldsymbol{f}$ is the applied force distribution per unit of s, and $\boldsymbol{l}$ is the applied moment distribution per unit of s. For clarity, we will take all vectors in (2.7) and (2.8) to be expressed coordinates of a fixed global frame throughout this dissertation. Taking the derivative of the static equilibrium conditions with respect to s, one arrives at the classic forms of the equilibrium differential equations for a special Cosserat rod,

$$\dot{\boldsymbol{n}}(s) + \boldsymbol{f}(s) = \boldsymbol{0}, \tag{2.9}$$

$$\dot{\boldsymbol{m}}(s) + \dot{\boldsymbol{p}}(s) \times \boldsymbol{n}(s) + \boldsymbol{l}(s) = \boldsymbol{0}. \tag{2.10}$$

These equations describe the evolution of $\boldsymbol{m}$ and $\boldsymbol{n}$ along s.

2.2.2 Strains

The deformation of a rod structure from its reference state $g^*(s)$ to a new state $g(s)$ implies a corresponding change from $\boldsymbol{\xi}^*(s)$ to $\boldsymbol{\xi}(s)$, which we denote $\Delta\boldsymbol{\xi}(s) = \boldsymbol{\xi}(s) - \boldsymbol{\xi}^*(s) = \left[\Delta\boldsymbol{v}(s)^T \;\; \Delta\boldsymbol{u}(s)^T\right]^T$. A consequence of the reference frame assignment convention is that each of the components of $\Delta\boldsymbol{\xi}(s)$ has a direct physical meaning in terms of the mechanical strains of the rod in its deformed state.

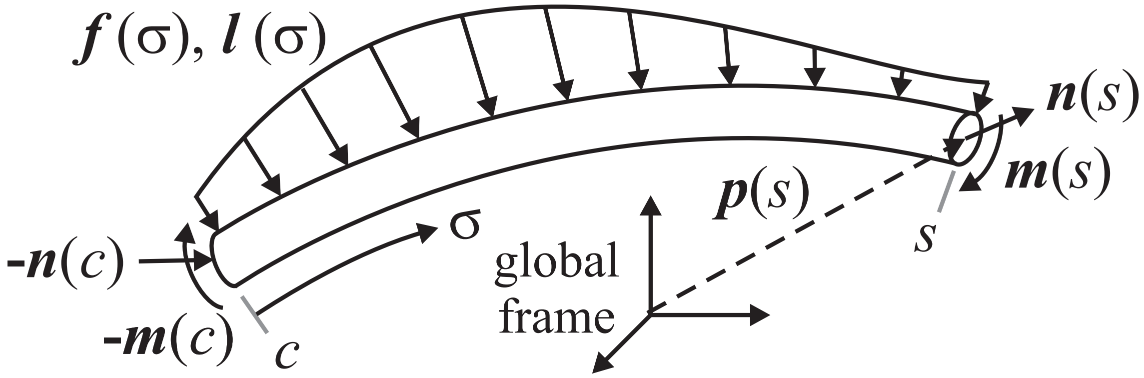

Figure 2.2: Arbitrary section of rod from c to s subject to distributed forces and moments. The internal forces $\boldsymbol{n}$ and moments $\boldsymbol{m}$ are also shown.

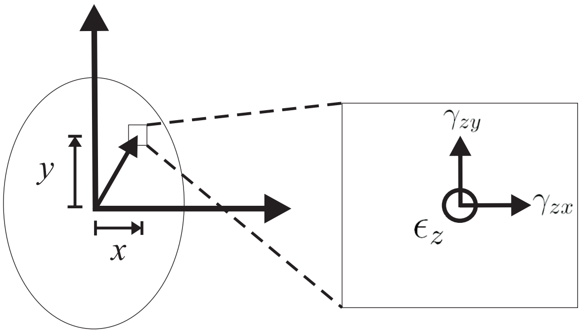

Figure 2.3: Cross section of the rod taken at the $x - y$ plane of the deformed frame $g(s)$. Strain quantities on this face of a small volume element are shown. These quantities are directly related to the vectors $\Delta\boldsymbol{v}(s)$ and $\Delta\boldsymbol{u}(s)$ in Equation 2.11.

First, the transverse shear strains experienced by the rod in the x and y directions of the deformed frame correspond to $\Delta\boldsymbol{v}_x$ and $\Delta\boldsymbol{v}_y$. Similarly, the elongation strain in the z direction corresponds directly to $\Delta\boldsymbol{v}_z$. Thus, $\Delta\boldsymbol{v}(s)$ is dimensionless.

The components of $\Delta\boldsymbol{u}_x$ and $\Delta\boldsymbol{u}_y$ similarly correspond to bending about the x and y axes of the deformed frame, and $\Delta\boldsymbol{u}_z$ corresponds to torsion about the z axis. Since $\boldsymbol{u}(s)$ represents the angular rate of change of $g(s)$ with respect to s, the units of $\Delta\boldsymbol{u}(s)$ are $length^{-1}$ (if s represents arc length).

With respect to the conventional strain quantities commonly used in beam mechanics, ϵ_z, γ_{zx}, and γ_{zy} (the normal and shear strains on the x-y face of a small volume as shown in Figure 2.3) can be recovered using $\Delta\boldsymbol{v}(s)$ and $\Delta\boldsymbol{u}(s)$.

$$[\gamma_{zx} \quad \gamma_{zy} \quad \epsilon_z]^T = \Delta\boldsymbol{v} - \boldsymbol{r} \times \Delta\boldsymbol{u}, \tag{2.11}$$

where $\boldsymbol{r} = [x \quad y \quad 0]^T$ is the position of the element within the cross section. This formulation assumes a linear strain profile across the section. The remaining two normal strains, ϵ_x, ϵ_y, and the remaining shear strain γ_{xy} are related to the deformation of the cross section itself, and the classical rod-mechanics theory that we employ in this dissertation assumes that cross sections always remain rigid. This is implicit in our original definition of a "rod" as a space curve paired with with an orthonormal rotation matrix for material orientation, which provides no mechanism for describing cross section deformation. This simplification provides a significant computational advantage over a full 3D continuum mechanics model, and is a widely accepted approximation for long slender rods whose cross sections are small compared to their length.

2.2.3 Constitutive Laws and Elastic Energy

Constitutive stress-strain laws provide the link between the kinematic variables $\boldsymbol{u}$ and $\boldsymbol{v}$ and the internal loads $\boldsymbol{m}$ and $\boldsymbol{n}$. As discussed above, the difference between the kinematic variables in the rod's reference state and those in the deformed state can be directly related to the mechanical strains in the rod. The internal loads in a rod are then related to the strains by a stress-strain constitutive law that takes the elastic material properties into account. Throughout this work, we employ the following linear constitutive relationships. Assuming that the x and y axes of g^* are aligned with the principal axes of the cross section, we have

$$\begin{aligned}\boldsymbol{n}(s) =& R(s)K_{SE}(s)\left(\boldsymbol{v}(s)-\boldsymbol{v}^*(s)\right),\\ \boldsymbol{m}(s) =& R(s)K_{BT}(s)\left(\boldsymbol{u}(s)-\boldsymbol{u}^*(s)\right),\end{aligned} \tag{2.12}$$

where

$$K_{SE}(s) = \begin{bmatrix} GA(s) & 0 & 0 \\ 0 & GA(s) & 0 \\ 0 & 0 & EA(s) \end{bmatrix},$$

$$K_{BT}(s) = \begin{bmatrix} EI_{xx}(s) & 0 & 0 \\ 0 & EI_{yy}(s) & 0 \\ 0 & 0 & G\left(I_{xx}(s)+I_{yy}(s)\right) \end{bmatrix},$$

where $A(s)$ is the area of the cross section, $E(s)$ is Young's modulus, $G(s)$ is the shear modulus, and $I_{xx}(s)$ and $I_{yy}(s)$ are the second moments of area of the tube cross section about the principal axes. (Note that $I_{xx}(s) + I_{yy}(s)$ is the polar moment of inertia about the centroid.) While it is possible to employ other nonlinear constitutive laws in the models throughout this dissertation, we use these linear relationships because they are notationally convenient and accurate for many continuum robots, including both designs that we consider here.

Given the above constitutive laws, the elastic energy that is stored in a rod in a deformed state is given by

$$E = \int_0^{\ell} \left(\boldsymbol{u}-\boldsymbol{u}^*\right)^T K_{BT}\left(\boldsymbol{u}-\boldsymbol{u}^*\right) + \left(\boldsymbol{v}-\boldsymbol{v}^*\right)^T K_{SE}\left(\boldsymbol{v}-\boldsymbol{v}^*\right)\, ds \tag{2.13}$$

2.2.4 Model Equations

In order to arrive at a full set of equations that can be used to calculate the shape of a deformed rod, we must combine the geometric descriptions with the equilibrium and constitutive laws. We can write (2.9) and (2.10) in terms of the kinematic variables using (2.12), their derivatives with respect to s, and the differential geometric relationship (2.5). After manipulation, this yields the full set of differential equations shown below.

$$\begin{aligned}
&\dot{\boldsymbol{p}} = R\boldsymbol{v} \\
&\dot{R} = R\widehat{\boldsymbol{u}} \\
&\dot{\boldsymbol{v}} = \dot{\boldsymbol{v}}^* - K_{SE}^{-1}\Big(\big(\widehat{\boldsymbol{u}}K_{SE} + \dot{K}_{SE}\big)(\boldsymbol{v} - \boldsymbol{v}^*) + R^T\boldsymbol{f}\Big) \\
&\dot{\boldsymbol{u}} = \dot{\boldsymbol{u}}^* - K_{BT}^{-1}\Big(\big(\widehat{\boldsymbol{u}}K_{BT} + \dot{K}_{BT}\big)(\boldsymbol{u} - \boldsymbol{u}^*) + \widehat{\boldsymbol{v}}K_{SE}(\boldsymbol{v} - \boldsymbol{v}^*) + R^T\boldsymbol{l}\Big)
\end{aligned} \tag{2.14}$$

Alternatively, an equivalent and often simpler system can be obtained using $\boldsymbol{m}$ and $\boldsymbol{n}$ as state variables rather than $\boldsymbol{v}$ and $\boldsymbol{u}$.

$$\begin{aligned}
&\dot{\boldsymbol{p}} = R\boldsymbol{v}, \quad \text{where } \boldsymbol{v} = K_{SE}^{-1}R^T\boldsymbol{n} + \boldsymbol{v}^* \\
&\dot{R} = R\widehat{\boldsymbol{u}}, \quad \text{where } \boldsymbol{u} = K_{BT}^{-1}R^T\boldsymbol{m} + \boldsymbol{u}^* \\
&\dot{\boldsymbol{n}} = -\boldsymbol{f} \\
&\dot{\boldsymbol{m}} = -\dot{\boldsymbol{p}} \times \boldsymbol{n} - \boldsymbol{l}
\end{aligned} \tag{2.15}$$

If the effects of shear and extension cause relatively small changes in the shape in comparison to the effects of bending and torsion (which is often the case for long slender rods, and we assume this in our models for concentric-tube robots), then a simplified model can be obtained by setting $\boldsymbol{v} = \boldsymbol{v}^*$. In the case of (2.14) with

$\boldsymbol{v} = \boldsymbol{v}^* = \boldsymbol{e}_3$, this results in

$$\begin{aligned}
\dot{\boldsymbol{p}} &= R\boldsymbol{e}_3 \\
\dot{R} &= R\widehat{\boldsymbol{u}} \\
\dot{\boldsymbol{n}} &= -\boldsymbol{f} \\
\dot{\boldsymbol{u}} &= \dot{\boldsymbol{u}}^* - K^{-1}\Big(\left(\hat{\boldsymbol{u}}K + \dot{K}\right)\left(\boldsymbol{u} - \boldsymbol{u}^*\right) + \widehat{\boldsymbol{e}}_3 R^T \boldsymbol{n} + R^T \boldsymbol{l}\Big).
\end{aligned} \tag{2.16}$$

Boundary conditions for a rod which is clamped at $s = 0$ and subject to an applied force $\boldsymbol{F}_\ell$ and moment $\boldsymbol{L}_\ell$ at $s = \ell$ would be $R(0) = R_0$, $\boldsymbol{p}(0) = \boldsymbol{p}_0$, $\boldsymbol{m}(\ell) = \boldsymbol{L}_\ell$, and $\boldsymbol{n}(\ell) = \boldsymbol{F}_\ell$.

2.2.5 Numerical Solution Methods

In implementing the robot models developed in this dissertation, we have used numerical shooting methods with great success to quickly and accurately solve boundary value problems like the ones outlined in Section 2.2.4. Research in the field of nonlinear rod mechanics, most notably that of Simo and Vu-Quoc [78], Rubin [13], and Antman [3], usually focuses any numerical treatments on solution of dynamic equations. Treatment of the static case is typically not focused on computational speed, and is done with a nonlinear finite-element approach, many times employing third-party nonlinear root-finding packages such as Matlab's `fsolve` function to solve the resulting large nonlinear system [13]. For the particular problems we address in this dissertation, we have found this type of method to perform slower than an easily implemented shooting method which uses standard algorithms for initial value problems (IVPs), especially when the methods outlined in Chapter 5 are used to efficiently obtain the gradients necessary to update the initial condition guesses. A more thorough investigation in the future may find advantages to the finite-element approach, but since the shooting methods provide sufficient speed ($>$ 1000 Hz on a standard PC) and accuracy for robot control, we have used them throughout this work.

Turning to the details of the IVP algorithms used in the shooting methods, we note that because of the special structure that elements of SE(3), and SO(3) have, numerical integration of equations like (2.5) above may sometimes require special care. In general, Runge-Kutta, and other standard methods are not guaranteed to preserve the orthonormality of a rotation matrix when the integration is performed element-wise using (2.5) or (2.6) directly. To remedy this, one could parameterize R using Euler angles or unit quaternions, or use a number of numerical methods specifically designed to preserve the structure of SO(3), a review of which can be found in [58]. Although not guaranteed to preserve orthonormality, integrating (2.1) or (2.6) directly is very easily programmed, and we have observed that the deviation from orthonormality tends to zero as step-size decreases using standard Runge-Kutta algorithms. If orthonormality is still a concern, a re-orthonormalization procedure could be implemented as is often done in registration problems. Furthermore, in several test cases, we observed that the positional accuracy of integrating (2.1) directly via an element-wise Runge-Kutta method noticeably exceeded the positional accuracy of several geometrically exact algorithms of the same order and step-size.

2.2.6 Geometric Exactness

A theory of rod deformation is sometimes referred to as “geometrically exact” if it makes no approximations with respect to kinematic variables [4]. The non-exact methods typically used to predict the deformation of structural beams often employ two “small deflection” approximations (either of which removes geometric exactness) to enable closed-form solutions: (1) the deformed shape is assumed “close” to the initial shape when computing the internal forces and moments, and (2) some approximate formula is used for the beam’s curvature in calculating the elastic curve. In this dissertation, our modeling approaches are based on the geometrically exact Cosserat rod theory outlined above, in which neither assumption is made.

2.3 Summary of Nomenclature

$*$: Denotes a variable defined for the reference state of a rod.

$\dot{}$: Denotes a derivative with respect to s, except where indicated in Chapter 5.

$\widehat{\ }$: Converts $\mathbb{R}^3$ to $\mathfrak{so}(3)$ and $\mathbb{R}^6$ to $\mathfrak{se}(3)$:

$$\widehat{\boldsymbol{u}} = \begin{bmatrix} 0 & -u_z & u_y \\ u_z & 0 & -u_x \\ -u_y & u_x & 0 \end{bmatrix}, \quad \begin{bmatrix} \boldsymbol{v} \\ \boldsymbol{u} \end{bmatrix}^{\wedge} = \begin{bmatrix} 0 & -u_z & u_y & v_x \\ u_z & 0 & -u_x & v_y \\ -u_y & u_x & 0 & v_z \\ 0 & 0 & 0 & 0 \end{bmatrix}$$

$\vee$: Inverse of the $\widehat{\ }$ operation. For example, $(\widehat{\boldsymbol{u}})^{\vee} = \boldsymbol{u}$.

s : $\in \mathbb{R}$ - Reference length parameter. It is often convenient for this to be the arc length along the reference backbone.

$\boldsymbol{p}(s)$: $\in \mathbb{R}^3$ - Position of rod centroid in global frame coordinates.

$R(s)$: $\in \mathrm{SO}(3)$ - Orientation of the rod material with respect to the global frame.

$g(s)$: $\in \mathrm{SE}(3)$ - Homogeneous transformation containing $R(s)$ and $\boldsymbol{p}(s)$. (The "body frame".)

$\boldsymbol{u}(s)$: $\in \mathbb{R}^3$ - Angular rate of change of g with respect to s in body-frame coordinates. $\boldsymbol{u} = \left(R^T \dot{R}\right)^\vee$

$\boldsymbol{v}(s)$: $\in \mathbb{R}^3$ - Linear rate of change of g with respect to s expressed in body-frame coordinates. $\boldsymbol{v} = R^T \dot{\boldsymbol{p}}$

$\boldsymbol{n}(s)$: $\in \mathbb{R}^3$ - Internal force in the rod expressed in global frame coordinates.

$\boldsymbol{m}(s)$: $\in \mathbb{R}^3$ - Internal moment in the rod expressed in global frame coordinates.

$\boldsymbol{f}(s)$: $\in \mathbb{R}^3$ - External force per unit s on the rod expressed in global frame coordinates.

$\boldsymbol{l}(s)$: $\in \mathbb{R}^3$ - External moment per unit s on the rod expressed in global frame coordinates.

E : Young's modulus of the rod material.

G : Shear Modulus of the rod material.

A : Area of the rod cross section.

I_{xx} : Second moment of area of the rod cross section about the body frame x axis.

I_{yy} : Second moment of area of the rod cross section about the body frame y axis.

I_{zz} : Polar moment of area of the backbone cross section about the body frame z axis. $I_{zz} = I_{xx} + I_{yy}$

Chapter 3

Concentric-Tube Continuum Robots

3.1 Introduction

As discussed in Chapter 1, robots consisting of several concentric, preshaped, elastic tubes can work dexterously in narrow, constrained, and/or winding spaces, as are commonly found in minimally invasive surgery. Previous models of these concentric-tube robots (also called ‘active cannulas’) use assumptions that imply piecewise constant precurvature of component tubes and neglect torsion in curved sections of the device. In this chapter we first develop a new model which overcomes these prior limitations, thus providing greater accuracy and generality. Using a coordinate-free energy formulation, we derive differential equations describing the interplay between bending and torsional effects in a collection of n concentric tubes with general precurved shapes. We detail how to solve the model equations to obtain the shape of the device as a function of base actuation and explore in detail the implications of torsional flexibility for the special case of two tubes. Experiments demonstrate that this framework is more descriptive of physical prototype behavior than previous models; it reduces model prediction error by 82% over the calibrated bending-only model, and 17% over the calibrated transmissional torsion model in a set of experiments.

In the latter part of this chapter we consider the fact that many practical applications where the active cannula must interact with its environment require a model that accounts for deformation under external loading. We apply geometrically exact rod theory to produce a forward kinematic model that accurately describes large deflections due to a general collection of externally applied point and/or distributed wrench loads. This model is a generalization of the kinematic model presented in the first half of the chapter. Experimental results are provided for both point and distributed loads. Average tip error under load was 2.91 mm (1.5 – 3% of total robot length), which is similar to the accuracy of prior kinematic models.

3.2 Kinematic Model

In this section we derive a model which describes the shape of multiple precurved tubes arranged concentrically in free space. We do this by formulating and minimizing an energy functional which describes the total elastic energy due to bending and torsion stored in all tubes of a general n-tube collection.

3.2.1 Assumptions

The energy formulation in this section is performed under the standard assumptions of Kirchhoff rod theory, a special case of Cosserat rod theory (see [3] for an in-depth treatment of both). Kirchhoff theory assumes inextensibility and neglects transverse shear strain, which are generally regarded as good assumptions for long thin rods like the tubes that make up an active cannula. We also neglect gravitational effects in this analysis, because they have little effect at the scales and stiffnesses involved in our work. This can be seen from standard cantilever beam theory, which predicts a tip deflection caused by gravity of only 60 microns for a single straight, horizontally cantilevered tube 100mm long, with an OD of 1.6mm, an ID of 1.3mm, and a Young's modulus of 50GPa. Note that this is a highly conservative calculation because (1) the actual cannula will consist of several concentric tubes and thus have a higher bending stiffness (2) it will not generally be straight (3) it will not generally be horizontally cantilevered, and (4) the elastic modulus may actually be up to 75GPa (the manufacturer, NDC, Inc., quotes a range of 41-75GPa). Thus, it does not appear to be necessary to consider gravitational loading this kinematic models (although we note that gravity may be incorporated using the static model developed in the second half of this chapter). We also neglect friction as has been done in all active cannula models to date. Qualitatively the authors have observed some frictional hysteresis in prototypes with tightly packed tubes, but do not observe any discernible hysteresis in the prototypes described in the experimental sections of this chapter. It is likely that frictional effects will be complex functions of a number of parameters including curvature functions, arc lengths, tolerances between tubes, surface smoothness, lubrication, etc., and a detailed study of all such effects is left to future work. Quantitatively, the suitableness of all the assumptions listed above can be tested by comparing model predictions to experimental tip positions. We provide such comparisons in the experimental sections of this chapter.

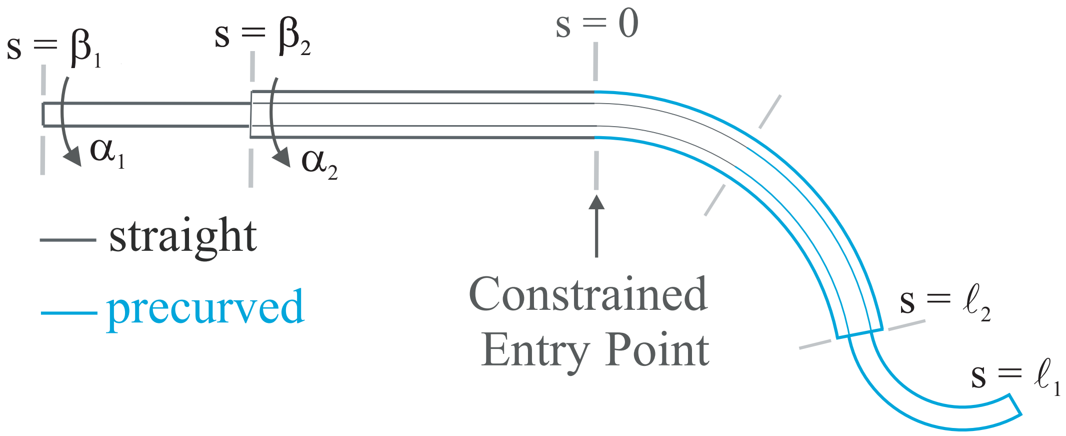

Figure 3.1: Diagram of tube overlap configuration with actuation inputs shown.

3.2.2 Precurved Tube Shapes

A diagram of a typical two-tube robot is shown in Figure 3.1, where blue sections denote regions where a tube has a non-straight precurved shape. A general n-tube robot could be more complex, but this example is sufficient for illustrating the variables associated with each tube. We denote s as the arc length along the robot from the point where it extends out of a constrained entry point (e.g. a hole in the front of an actuation unit, or a surgical trocar port), where a fixed global base frame $g_{base} = I$ may be located, in whose coordinates we will describe the shape of the robot. The base of the i^{th} tube is located at an arc length of $\beta_i < 0$, and is axially rotated by an angle α_i with respect to some fixed base frame. Thus, the robot's actuator variables consist of the set $\{\alpha_1 ... \alpha_n, \beta_1 ... \beta_n\}$, and the forward kinematics problem consists of determining the resulting shape of the robot for a given set of tubes and actuation variables

Following the conventions in Chapter 2, we assume that each tube is described by an arc-length-parameterized curve in its reference state $\boldsymbol{p}_i^*(s)$ for $s \in [\beta_i, \beta_i + \ell_i]$ where ℓ_i is the length of tube i.We attach reference frames to each preshaped tube continuously along the arc length, s, with the local z axis always pointing along the tangent to the curve, $\dot{\boldsymbol{p}}_i$, and with the origin of the reference frame at $\boldsymbol{p}_i(s)$. Thus, a set of reference frames $g_i^*(s) \in \mathrm{SE}(3)$ is defined, one for each tube as

$$g_i^*(s) = \begin{bmatrix} R_i^*(s) & \boldsymbol{p}_i^*(s) \\ \mathbf{0}^T & 1 \end{bmatrix},$$

where $R_i^*(s) \in \mathrm{SO}(3)$ is the rotation of the frame at the point s along the curve relative to the base frame, and the z-axis tangency convention implies that

$$\dot{\boldsymbol{p}}^* = R^* \boldsymbol{e}_3. \tag{3.1}$$

The creation of these frames establishes a pre-curvature vector as

$$\boldsymbol{u}^*(s) = \left(R^{*T}(s)\dot{R}^*(s)\right)^\vee.$$

Our goal is to find the new deformed shape $g_i(s)$ of each tube when the tubes are constrained to be concentric and actuated by base rotation and translation as shown in Figure 3.1.

3.2.3 Constraints for Concentric Tubes

We define concentric tubes as being constrained to follow a common trajectory in space, that is, $\boldsymbol{p}_1(s) = \boldsymbol{p}_2(s) = ... = \boldsymbol{p}_n(s)$ for $s \in [0\ \ell]$. We designate this common deformed curve as $\boldsymbol{p}(s)$. Note that this does not imply that each $g_i(s)$ must be equal.

The equality of the deformed curves implies that $\boldsymbol{p}_1(0) = \boldsymbol{p}_2(0) = ... = \boldsymbol{p}_n(0)$ and $\dot{\boldsymbol{p}}_1(s) = \dot{\boldsymbol{p}}_2(s) = ... = \dot{\boldsymbol{p}}_n(s)$.

Under the assumption of zero shear or extension in the tube deformation, the z-axis tangency constraint (3.1) also holds for the deformed tube shapes, $\dot{\boldsymbol{p}}_i = R_i\boldsymbol{e}_3$. This implies that the third columns of each $R_i(s)$ are equal, so that each $R_i(s)$ differs from the others by a rotation about the local tangent z axis. We introduce an angle $\theta_i(s)$ to parameterize the angular difference between the frame of tube i and that of tube one as follows:

$$R_i(s) = R_1(s)R_{\theta_i}, \tag{3.2}$$

where $R_{\theta_i} = e^{\widehat{\boldsymbol{e}}_3\theta_i(s)} = \begin{bmatrix} \cos(\theta_i) & -\sin(\theta_i) & 0 \\ \sin(\theta_i) & \cos(\theta_i) & 0 \\ 0 & 0 & 1 \end{bmatrix}$. denotes a rotation about the z axis by $\theta_i(s)$, and $\theta_1 \equiv 0$ by definition. (Similarly, we use a Greek subscripted R to denote a rotation about z by the subscript angle throughout the dissertation). Figure 3.2 below illustrates how $\theta_i(s)$ relates $g_1(s)$ to $g_i(s)$.

This further implies a relationship between the tube curvature vectors. Applying the definition of $\boldsymbol{u}_i$, we obtain,

$$\boldsymbol{u}_i = \left(R_i^{\mathrm{T}}\dot{R}_i\right)^{\vee} = R_{\theta_i}^{\mathrm{T}}\boldsymbol{u}_1 + \dot{\theta}_i\boldsymbol{e}_3. \tag{3.3}$$

Interpreted geometrically, this equation says that the local x and y curvatures of each deformed tube are equal when expressed in the same reference frame. The torsional z components are free to vary independently for each tube. We note that the third component of (3.3) gives us

$$\dot{\theta}_i = u_{i,z} - u_{1,z} \tag{3.4}$$

It will be convenient to define an additional angle $\psi_i(s)$ for each tube which describes that tube's absolute material orientation away from a common reference frame along the length of the robot. We define

$$\psi_i(s) = \alpha_i + \int_{\beta_i}^{s} u_{iz} d\sigma. \tag{3.5}$$

where α_i is the z-axis rotation of the tube base with respect to the fixed global frame. This implies that $\theta_i = \psi_i - \psi_1$, and

$$R_i(s) = R_B(s) R_{\psi_i}(s).$$

where R_B is the Bishop frame rotation matrix which coincides with the fixed global frame at $s = 0$ and then evolves along the common deformed curve with no instantaneous rotation about the z axis, which is to say that its curvature vector has the form

$$\boldsymbol{u}_B(s) = \left(R_B^T \dot{R}_B\right)^{\vee} = [u_{Bx} \;\; u_{By} \;\; 0]^T .$$

Then, the tube curvature vectors are related to the bishop curvature by

$$\boldsymbol{u}_i = R_{\psi_i}^T \boldsymbol{u}_B + \dot{\psi}_i \boldsymbol{e}_3, \tag{3.6}$$

which implies that

$$\dot{\psi}_i = u_{iz}. \tag{3.7}$$

3.2.4 Stored Elastic Energy

As stated above, we assume that the only degrees of freedom required to describe the conformations of each tube are bending and twisting. Therefore, the deformation energy stored in a section of tube i from $s = \sigma_1$ to $s = \sigma_2$ is given by

$$E = \frac{1}{2} \int_{\sigma_1}^{\sigma_2} [\boldsymbol{u}(s) - \boldsymbol{u}^*(s)]^T K(s) [\boldsymbol{u}(s) - \boldsymbol{u}^*(s)] ds, \tag{3.8}$$

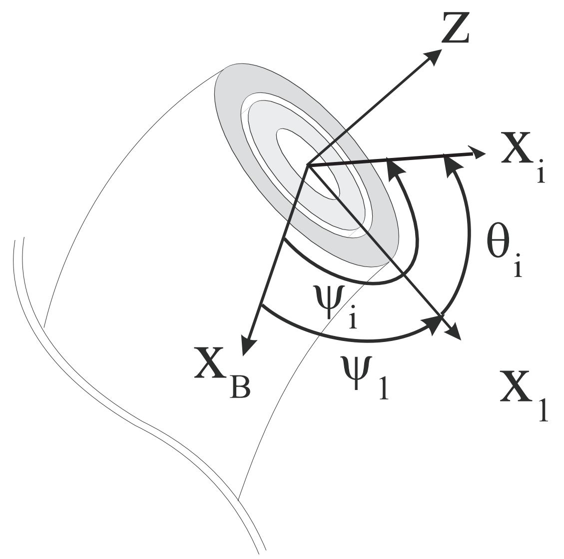

Figure 3.2: Shown here are coordinate frames for the first and the i^{th} tubes, and the Bishop backbone frame at an arbitrary cross section of the active cannula. The z axes coincide and are tangent to the backbone curve. The x axis of each frame is located an angle ψ_i away from the Bishop frame, and the x axis of frame i is located an angle θ_i away from frame 1.

where $K = K_{BT}$ from Chapter 2, $\boldsymbol{u}^*(s) = (R^*(s)^T\dot{R}^*(s))^\vee$ is the local curvature vector of the pre-shaped, unloaded tube frame $g(s)$, and $\boldsymbol{u}(s) = (R(s)^T\dot{R}(s))^\vee$ is the local curvature vector after deformation. A very similar formulation of elastic energy in a Kirchhoff rod can be found in [10], and a more general formulation similar to 2.13 (for a tendon-driven continuum robot) which includes extensibility and shear is given in [32]. In general, the stiffness matrix in (3.8) depends on the material properties of the tube, its geometry, and the way in which the reference frame is attached. For example, if the local x and y axes of the reference frame are attached according to the Frenet-Serret convention, then in another reference system, such as a Bishop's frame, $\tilde{K}(s) = Q^T(s)K(s)Q(s)$ where $Q(s) = \exp\left\{\widehat{\boldsymbol{e}}_3\theta(s)\right\} \in \mathrm{SO}(3)$ is the relative rotation between these two systems of backbone reference frames around the z axis.

However, in the special case that

$$K = \begin{bmatrix} k_1 & 0 & 0 \\ 0 & k_1 & 0 \\ 0 & 0 & k_3 \end{bmatrix} \tag{3.9}$$

is constant in one such coordinate system (and this occurs whenever when the tube has an annular cross section), then $\tilde{K}(s) = K$. Thus for annular tubes, the stiffness matrix will be independent of the frame assignment as long as the z-axis tangent convention is followed.

For a cylindrical tube of constant cross-sectional inertia, $I = I_{xx} = I_{yy}$, and polar moment, $J = I_{zz}$, then $k_1 = EI$ and $k_3 = GJ$, where E denotes the Young's Modulus and G denotes the sheer modulus. Note that K can never be a scaled identity for cylindrical tubes, since

$$EI = GJ \Rightarrow \frac{E}{G} = \frac{J}{I} = 2 \Rightarrow 2(1+\nu) = 2 \Rightarrow \nu = 0,$$

and, for physical materials, $\nu \neq 0$.

For a general collection of n concentric tubes overlapping continuously for $s \in [\sigma_1, \sigma_2]$, the stored elastic energy will be the sum of the energies stored in the individual tubes:

$$E = \frac{1}{2}\sum_{i=1}^{n}\int_{\sigma_1}^{\sigma_2}[\boldsymbol{u}_i\,(s) - \boldsymbol{u}_i^*(s)]^T K_i(s)[\boldsymbol{u}_i\,(s) - \boldsymbol{u}_i^*(s)]ds. \tag{3.10}$$

where $\boldsymbol{u}_i^*(s)$ is the pre-shaped curvature and $\boldsymbol{u}_i(s)$ is the equilibrium curvature for tubes $i = 1 \ldots n$.

Our objective in the next section is to minimize the total elastic energy (3.10) stored in the tubes, subject to the concentric constraints (3.3).

3.2.5 Minimizing the Energy Functional

Substituting the concentric constraints (3.3) into the energy functional (3.10), we have

$$
\begin{aligned}
E &= \frac{1}{2}\int_{\sigma_1}^{\sigma_2}\sum_{i=1}^{n}[R_{\theta_i}^T\boldsymbol{u} + \dot{\theta}_i\boldsymbol{e}_3 - \boldsymbol{u}_i^*]^T K_i[R_{\theta_i}^T\boldsymbol{u} + \dot{\theta}_i\boldsymbol{e}_3 - \boldsymbol{u}_i^*]ds \\
&= \frac{1}{2}\int_{\sigma_1}^{\sigma_2}\sum_{i=1}^{n}\Big(\boldsymbol{u}^T K_i\boldsymbol{u} + G_iJ_i\dot{\theta}_i^2 + \boldsymbol{u}_i^{*T}K_i\boldsymbol{u}_i^* \\
&\qquad + 2G_iJ_i\dot{\theta}_i\,(u_z - u_{iz}^*) - 2\boldsymbol{u}^T R_{\theta_i}K_i\boldsymbol{u}_i^*\Big)ds.
\end{aligned}
\tag{3.11}
$$

where we have defined $\boldsymbol{u}(s) = \boldsymbol{u}_1(s)$, and we have assumed that K_i is diagonal with its first two diagonal elements equal (since we are primarily concerned with the case of tubes with annular cross sections), so that

$$
\boldsymbol{u}^T R_{\theta_i}K_iR_{\theta_i}^T\boldsymbol{u} = \boldsymbol{u}^T K_i\boldsymbol{u}, \text{ and } \boldsymbol{u}^T R_{\theta_i}K_i\dot{\theta}_i\boldsymbol{e}_3 = G_iJ_iu_z\dot{\theta}_i. \tag{3.12}
$$

Thus, by incorporating the constraints (3.3), the variables over which we are minimizing reduce to $(\boldsymbol{u}(s), \theta_2(s), \dot{\theta}_2(s), \ldots, \theta_n(s), \dot{\theta}_n(s))$. In order to find the minimizing $\boldsymbol{u}$, it is possible to complete the square and re-write the energy as

$$
E = \frac{1}{2}\int_{\sigma_1}^{\sigma_2}(\boldsymbol{u} - \boldsymbol{\alpha})^T K(\boldsymbol{u} - \boldsymbol{\alpha}) + C\,ds, \tag{3.13}
$$

where

$$
\begin{aligned}
\overline{\boldsymbol{u}}_i^* &= R_{\theta_i}\boldsymbol{u}_i^* - \dot{\theta}_i\boldsymbol{e}_3, & K &= \sum_{i=1}^{n}K_i, \\
\boldsymbol{\alpha} &= K^{-1}\sum_{i=1}^{n}K_i\overline{\boldsymbol{u}}_i^*, & C &= \sum_{i=1}^{n}\overline{\boldsymbol{u}}_i^{*T}K_i\overline{\boldsymbol{u}}_i^* - \boldsymbol{\alpha}^T K\boldsymbol{\alpha},
\end{aligned}
\tag{3.14}
$$

and we note since neither C nor $\boldsymbol{\alpha}$ depends on $\boldsymbol{u}$, it is easy to see that the $\boldsymbol{u}$ which minimizes this integral must be $\boldsymbol{u} = \boldsymbol{\alpha}$.

The same result can be obtained by the application of static equilibrium conditions. Realizing that in the absence of external loads, the sum of the internal moments carried by each tube must equal zero at every arc length location, we have

$$\begin{aligned} \sum_{i=1}^{n} R_{\theta_i} K_i (\boldsymbol{u}_i - \boldsymbol{u}_i^*) &= \sum_{i=1}^{n} R_{\theta_i} K_i (R_{\theta_i}^T \boldsymbol{u} + \dot{\theta}_i \boldsymbol{e}_3 - \boldsymbol{u}_i^*) = 0 \\ \implies \quad \boldsymbol{u} &= K^{-1} \sum_{i=1}^{n} K_i \left(R_{\theta_i} \boldsymbol{u}_i^* - \dot{\theta}_i \boldsymbol{e}_3 \right) = \boldsymbol{\alpha}. \end{aligned} \tag{3.15}$$

Having found the minimizing $\boldsymbol{u}$, we now only need to find the minimizing functions $\theta_i(s)$. To do this, we apply the Euler Lagrange equation,

$$\frac{\partial f}{\partial \theta_i} - \frac{d}{ds}\left(\frac{\partial f}{\partial \dot{\theta}_i}\right) = 0, \tag{3.16}$$

to the expanded integrand of (3.11) $n-1$ times, once with respect to each θ_i. Assuming that $G_i J_i$ is constant with respect to s, this results in

$$G_i J_i \left(\ddot{\theta}_i - \dot{u}_{iz}^* + \dot{u}_z \right) + \boldsymbol{u}_i^{*T} K_i \frac{\partial R_{\theta_i}^T}{\partial \theta_i} \boldsymbol{u} = 0.$$

for $i = 2...n$. Now substituting in the result $\boldsymbol{u} = \boldsymbol{\alpha}$, we get a system of differential equations which defines the variables $\theta_1...\theta_n$.

$$G_i J_i \ddot{\theta}_i - G_i J_i \dot{u}_{iz}^* + \frac{G_i J_i}{GJ} \sum_{j=1}^{n} G_j J_j (\ddot{\theta}_j - \dot{u}_{jz}^*) = \frac{E_i I_i}{EI} \sum_{j=1}^{n} E_j I_j \boldsymbol{u}_{ixy}^{*T} B_{\theta ij} \boldsymbol{u}_{jxy}. \tag{3.17}$$

where $EI = \sum_{k=1}^{n} E_k I_k$, $EI = \sum_{k=1}^{n} E_k I_k$, and

$$B_{\theta ij} = \begin{bmatrix} \sin(\theta_i - \theta_j) & -\cos(\theta_i - \theta_j) \\ \cos(\theta_i - \theta_j) & \sin(\theta_i - \theta_j) \end{bmatrix}$$

We note that the system of differential equations given by (3.17) for $i = 2...n$ is coupled in the variables $\theta_2...\theta_n$ and $\ddot{\theta}_2...\ddot{\theta}_n$. Since the coupling in $\ddot{\theta}_2...\ddot{\theta}_n$ is linear, it is possible to decouple the second derivative variables and write these equations as a second-order vector system $\ddot{\boldsymbol{\theta}} = \boldsymbol{f}(s, \boldsymbol{\theta})$. However, an even simpler system of differential equations can be derived by re-writing the energy minimization problem in terms of the absolute angular variables $\psi_1 ... \psi_n$. This comes at the price of introducing one more variable than is actually needed to solve the problem, but results in a simpler, more efficient expression of the governing equations. Re writing the energy using (3.6), we get

$$\begin{aligned} E &= \frac{1}{2}\int_{\sigma_1}^{\sigma_2} \sum_{i=1}^{n} [R_{\psi_i}^T \boldsymbol{u}_B + \dot{\psi}_i \boldsymbol{e}_3 - \boldsymbol{u}_i^*]^T K_i [R_{\psi_i}^T \boldsymbol{u}_B + \dot{\psi}_i \boldsymbol{e}_3 - \boldsymbol{u}_i^*] ds \\ &= \frac{1}{2}\int_{\sigma_1}^{\sigma_2} \sum_{i=1}^{n} \Big(\boldsymbol{u}_B^T K_i \boldsymbol{u}_B + G_i J_i \dot{\psi}_i^2 + \boldsymbol{u}_i^{*T} K_i \boldsymbol{u}_i^* \\ &\qquad + 2 G_i J_i \dot{\psi}_i \left(u_{Bz} - u_{iz}^* \right) - 2 \boldsymbol{u}_B^T R_{\psi_i} K_i \boldsymbol{u}_i^* \Big) ds. \end{aligned} \tag{3.18}$$

As before, the minimizing $\boldsymbol{u}_B$ can be found by completing the square, or by applying static equilibrium conditions. The result is

$$\boldsymbol{u}_B = K^{-1} \sum_{i=1}^{n} K_i \Big(R_{\psi_i} \boldsymbol{u}_i^* - \dot{\psi}_i \boldsymbol{e}_3 \Big). \tag{3.19}$$

After applying the Euler-Lagrange equation to the integrand of (3.18) for $\psi_1 ... \psi_n$, we get a result similar to (3.17),

$$G_i J_i \Big(\ddot{\psi}_i - \dot{u}_{iz}^* + \dot{u}_{Bz} \Big) + \boldsymbol{u}_i^{*T} K_i \frac{\partial R_{\theta_i}^T}{\partial \theta_i} \boldsymbol{u}_B = 0,$$

but a simplification results from the fact that $u_{Bz} = 0$. Hence, the equations are already decoupled in $\ddot{\psi}_1 ... \ddot{\psi}_n$, and can easily be expressed in state-vector form:

$$\ddot{\psi}_i = \dot{u}_{iz}^* + \frac{E_i I_i}{EI G_i J_i} \sum_{j=1}^{n} E_j I_j \boldsymbol{u}_{ixy}^{*T} B_{\psi ij} \boldsymbol{u}_{jxy}. \tag{3.20}$$

These fundamental differential equations describing the evolution of torsion along concentric precurved tubes can also be derived from the equilibrium equations of Cosserat rod theory outlined in Chapter 2. Starting with 2.10 written for tube i,

$$\dot{\boldsymbol{m}}_i + \dot{\boldsymbol{p}}_i \times \boldsymbol{n}_i + \boldsymbol{l}_i = \boldsymbol{0},$$

we multiply both sides by $\boldsymbol{e}_3^T R_i^T$ and expand using $\boldsymbol{m}_i = R_i(\boldsymbol{u}_i - \boldsymbol{u}_i^*)$, $\dot{R}_i = R_i\boldsymbol{u}_i$, and $\dot{\boldsymbol{p}}_i = R_i\boldsymbol{e}_3$ to obtain

$$\dot{\boldsymbol{u}}_{iz} = \dot{\boldsymbol{u}}_{iz}^* + \frac{E_iI_i}{G_iJ_i}\left(u_{ix}u_{iy}^* - u_{iy}u_{ix}^*\right)$$

where we have recognized that $\boldsymbol{e}_3^T R_i^T \boldsymbol{l}_i$ must be zero because the assumption of no friction implies that the tubes cannot apply any axial moment distributions to one another. Then, after applying (3.19), we obtain exactly the same equation as (3.20).

If the preshaped tubes have constant curvature vectors of the form $\boldsymbol{u}_i^* = [\kappa_i \ \ 0 \ \ 0]^T$, or $\boldsymbol{u}_i^* = [0 \ \ \kappa_i \ \ 0]^T$, then (3.20) reduces to

$$\ddot{\psi}_i = \frac{E_iI_i}{EIG_iJ_i}\sum_{j=1}^{n} E_jI_j\kappa_i\kappa_j \sin\left(\psi_i - \psi_j\right). \tag{3.21}$$

This is a very common case for concentric-tube robot prototypes, and thus the simplicity of (3.21) may be very useful for researchers implementing the results of this dissertation for future robots. In the next section, we discuss how the model equations can be solved and how the resulting shape of a concentric-tube robot can be computed.

3.2.6 Solving the Kinematic Model Equations

It is straightforward to apply the model equations developed in the previous section to compute the shape of a concentric-tube robot. As shown in Figure 3.1, a two tube robot can be considered to have four distinct sections, which begin and end where tubes begin and end, or where tubes transition from straight to curved. For example, beginning at the base of the cannula, the sections will often be as follows: (1) a section where both tubes are straight, (2) a section where one tube is curved and the other

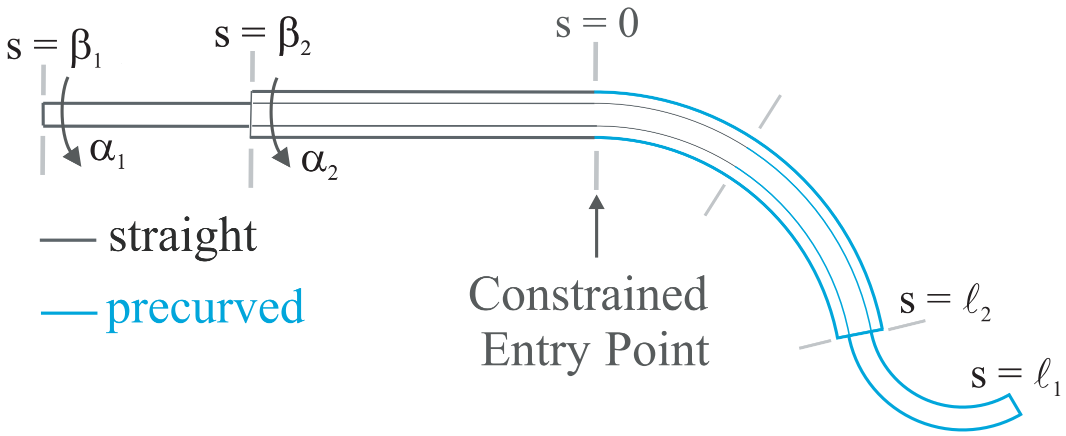

Figure 3.3: Diagram of tube overlap configuration with actuation inputs shown.

is straight, (3) a section where both tubes are curved, and (4) a section where only one tube is present and curved.

For a general n-tube robot, (3.20) can be used to describe the torsional behavior throughout the entire robot. In each section, the sums must simply be performed over all the tubes that are present. Equation 3.20 can be equivalently expressed by the two first order equations,

$$\begin{aligned} \dot{\psi}_i &= u_{iz} \\ \dot{u}_{iz} &= \dot{u}^*_{iz} + \frac{E_i I_i}{E I G_i J_i} \sum_{j=1}^{n} E_j I_j \boldsymbol{u}^{*T}_{ixy} B_{\psi ij} \boldsymbol{u}_{jxy}. \end{aligned} \tag{3.22}$$

We assume that the tubes are constrained to be straight until they emerge from the constrained entry point at the “base” of the robot. In this case, (3.22) implies that the torsion u_{iz} is constant, and thus the angle ψ_i varies linearly with s. Thus, we can write initial conditions for ψ_i at $s = 0$ which represent the combined effects of the actuation variables and the torsional deformation in the $s < 0$ region, namely

$$\psi_i(0) = \alpha_i - \beta_i u_{iz}(0). \tag{3.23}$$

Since the frictionless assumption implies that tubes cannot apply axial moments to one another, a torsion-free boundary condition exists at the end of each tube,

$$u_{iz}(\ell_i) = 0. \tag{3.24}$$

A simple shooting method is an efficient way to solve the boundary value problem represented by (3.22), (3.23), and (3.24). The basic procedure is to guess a value for each unknown initial torsion variable u_{iz}. Then compute the initial conditions for $\psi_i(0)$ using (3.23), and integrate all variables in (3.22) from $s = 0$ to $s = \max(\beta_1 + \ell_1, ..., \beta_n + \ell_n)$ using any standard numerical integration algorithm for initial value problems (IVP's), such as the Runge-Kutta family of methods. After the integration is performed, the boundary condition (3.24) is checked. If it is satisfied then the boundary value problem has been solved. If it is not satisfied, then a new guess for u_{iz} must be tried until it is. Thus, the shooting method can be thought of as an IVP integration algorithm couched inside a nonlinear root finding loop where the next guess for the unknown initial conditions may be calculated according to any of the well established root-finding methods such as Gauss-Newton, Steepest Descent, or Levenberg-Marquardt. The implementation of this approach can be done quite easily in Matlab by using the functions `ode45` and `fsolve`. For computational efficiency, it is desirable to implement the equations in a compiled language like C++, and to also take advantage of the methods in Chapter 5 for efficiently computing the Jacobian of the boundary conditions with respect to the initial conditions.

Once the boundary value problem given by (3.22), (3.23), and (3.24) has been solved, then the remaining components (u_{ix} and u_{iy}) of the deformed curvature vector can be obtained for each tube using the calculated solution, (3.19) and (3.6),

$$\boldsymbol{u}_{ixy} = \frac{1}{EI}\sum_{j=1}^{n} R_{\psi_j - \psi_i} E_j I_j \boldsymbol{u}^*_{ixy}. \tag{3.25}$$

This deformed curvature vector then provides the information needed to determine the deformed shape of any of the tubes by integrating the geometric differential equation

$$\begin{aligned} \dot{\boldsymbol{p}}_i &= R_i \boldsymbol{e}_3 \\ \dot{R}_i &= R_i \widehat{\boldsymbol{u}}_i, \end{aligned}$$

where numerical methods for doing this have been discussed in Chapter 2.

3.2.7 Analytical Solution for Two Circular Tubes

While the kinematic model equations can be solved numerically for any number of component tubes, some insight into the fundamental behavior of active cannulas can be gained buy considering the case of an active cannula composed of two circularly precurved tubes, for which an analytical solution can be found. This special case is interesting because an analytical solution exists, and because all prior experimental inquiries to date into active cannula behavior have addressed exclusively this particular case (see e.g. [27, 94]).

We consider the case where $n = 2$, $\boldsymbol{u}^*_1 = [\kappa_1 \quad 0 \quad 0]^T$, and $\boldsymbol{u}^*_2 = [\kappa_2 \quad 0 \quad 0]^T$. Expanding (3.17) in this case yields

$$\frac{G_1 J_1 G_2 J_2}{G_1 J_1 + G_2 J_2}\ddot{\theta} - \kappa_1 \kappa_2 \frac{E_1 I_1 E_2 I_2}{E_1 I_1 + E_2 I_2}\sin\theta = 0, \tag{3.26}$$

where θ_2 has been replaced with θ. Under the assumption that the two tubes have the same value of ν, Poisson's ratio, this equation reduces to

$$\ddot{\theta} - \kappa_1 \kappa_2 (1 + \nu)\sin\theta = 0, \tag{3.27}$$

however, we will not make this assumption here, for the sake of generality. Let

$$a = \kappa_1 \kappa_2 \frac{E_1 I_1 E_2 I_2 (G_1 J_1 + G_2 J_2)}{G_1 J_1 G_2 J_2 (E_1 I_1 + E_2 I_2)}, \tag{3.28}$$

so that

$$\ddot{\theta} - a \sin\theta = 0. \tag{3.29}$$

The appropriate boundary conditions here are the initial angle determined by the relative angular position of the tube bases, $\theta(0) = \theta_0$, and the natural boundary condition at the free end, $\dot{\theta}(L) = 0$. This natural boundary condition can be intuitively understood by considering that $\dot{\theta}(s) \propto$ axial torque applied at s. At L there is no torque being applied to the distal end of either tube. Thus, $\dot{\theta}(L) = 0$.

Notice that (3.29) has the same form as the differential equation which describes a simple pendulum. Fortunately, this equation arises often, and it has a known analytical solution in terms of Jacobi's elliptic functions. We solve it following the solution procedure similar to the method described in [1], which begins by multiplying both sides of (3.29) by $\dot{\theta}$, and integrating once. Applying the boundary condition $\dot{\theta}_L = 0$ then yields

$$\dot{\theta}^2 + 2a\cos\theta = 2a\cos\theta_L. \tag{3.30}$$

Rearranging (3.30), we obtain

$$s = \pm \frac{1}{\sqrt{2a}} \int_{\theta_0}^{\theta(s)} \frac{d\theta}{\sqrt{\cos\theta_L - \cos\theta}} \tag{3.31}$$

Now we use $\cos(\theta + \pi(1+2n)) = -\cos\theta \;\; \forall n \in Z$, and $\cos 2\theta = 1 - 2\sin^2\theta$, to write this in terms of incomplete elliptic integrals of the first kind as follows. First let

$$\gamma = \theta + \pi(1+2n), \quad k = \sin\frac{\gamma_L}{2} = \sqrt{\frac{1-\cos\gamma_L}{2}}, \tag{3.32}$$

and let Φ be defined by

$$\cos\gamma = 1 - 2k^2 \sin^2\Phi. \tag{3.33}$$

Then we have

$$\cos\gamma - \cos\gamma_L = 2k^2\cos^2\Phi, \quad \text{and} \quad \sin\gamma = 2k\sin\Phi\left(1 - k^2\sin^2\Phi\right)^{\frac{1}{2}} \tag{3.34}$$

So that (3.31) becomes

$$s = \pm\sqrt{\frac{1}{a}}\int_{\Phi(0)}^{\Phi(s)} \frac{d\theta}{\sqrt{1 - k^2\sin^2(\Phi)}} = \pm\sqrt{\frac{1}{a}}\Big(F\left(\Phi(s), k\right) - F\left(\Phi(0), k\right)\Big) \tag{3.35}$$

where $F(\Phi, k)$ is the elliptic integral of the first kind with amplitude Φ and modulus k. We can now use the Jacobi Amplitude functions, sn and cn which are the sine and cosine of the inverse function of F defined by the identities

$$\text{sn}(F(\Phi, k), k) = \sin\Phi \quad \text{and} \quad \text{cn}(F(\Phi, k), k) = \cos\Phi \tag{3.36}$$

to obtain the following solutions:

$$\begin{aligned} \theta(s) &= 2\,\sin^{-1}\left(k\ \text{sn}\left(F\left(\Phi(0), k\right) \pm \sqrt{a}s, k\right)\right) - \pi(1 + 2n) \\ \dot{\theta}(s) &= \pm 2k\sqrt{a}\ \text{cn}\left(F\left(\Phi(0), k\right) \pm \sqrt{a}s, k\right). \end{aligned} \tag{3.37}$$

The ± signs in (3.37) and take the same sign as $\theta_L - \theta_0$, and n is chosen such that γ_L takes on a value in the range $-\pi \leq \gamma_L \leq \pi$.

3.2.8 Implications of Torsion

In order to investigate the phenomena of multiple solutions and non-circular equilibrium shapes, we provide the following example. Consider a tube and a wire with properties given in Table 3.1. The long curved lengths of L_1=200 mm and L_2=140

Table 3.1: Physical Properties of Tube and Wire used in Simulation.

	Outer Tube	Inner Wire
Young's Modulus (GPa)	58	58
Shear Modulus (GPa)	21.5	21.5
Inner Diameter (mm)	2.01	0
Outer Diameter (mm)	2.39	1.60
Length (mm)	140	200
Curvature (1/mm)	0.0099	0.0138

mm for the inner wire and the outer tube, respectively, make the interaction of the curved portions pronounced and thus more easily visualizable. The boundary condition at the proximal end, where $s = 0$, is $\theta(0) = \theta_0 = \alpha_2 - \alpha_1$, where α_2 and α_1 are the base rotation angles applied by the actuators at the tube bases. The boundary condition at the free distal end where the outer tube ends ($s = L_2$) is $\dot{\theta}_{L_2} = 0$, which was already implicitly enforced on our solution in Equation (3.30). The analytical solution (3.37) contains the unknown constant, θ_{L_2} within k, so we find a solution for θ_{L_2} which satisfies the proximal boundary condition $\theta_0 = \alpha_2 - \alpha_1$, using a numerical root-finding procedure.

In [94] torsion was considered in straight transmission sections of a cannula. It was shown that in this case, multiple solutions (local minimum energy configurations) can emerge. We see the same phenomenon here. In general, there can be more than one value of θ_L which satisfies the boundary condition. The particular root to which the algorithm converges is dependent on the initial guess. As noted in [94]

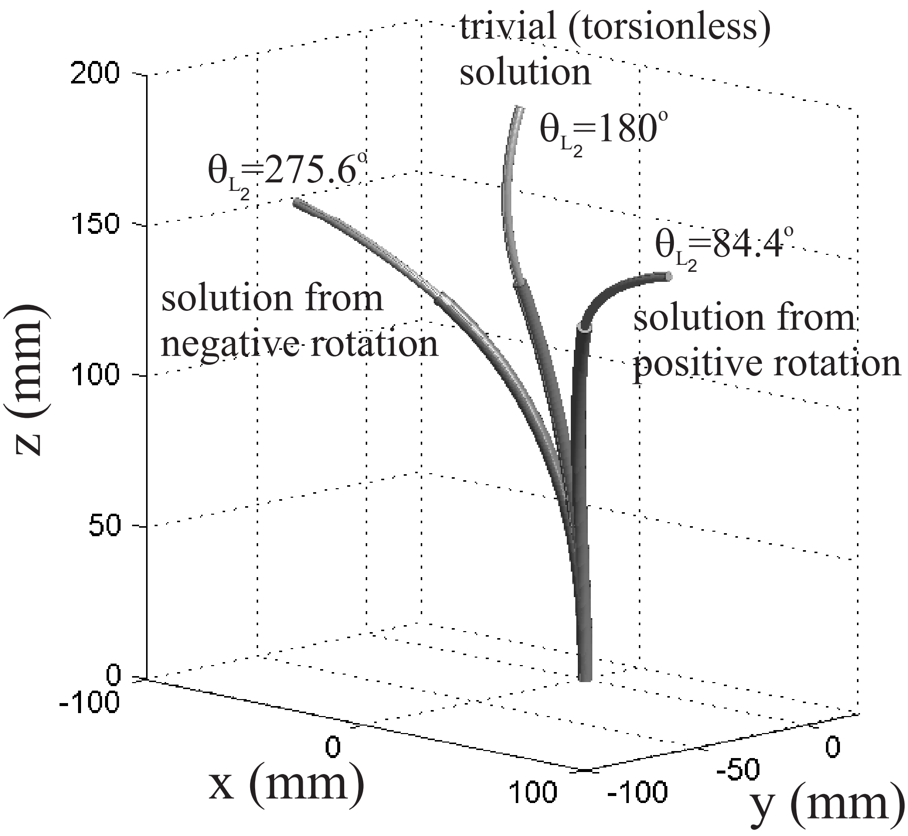

Figure 3.4: Simulation of the tubes given in Table 3.1 with the inner wire rotated to a base angle of $\alpha_1 = -180°$ so that $\theta_0 = 180°$. Three equilibrium conformations are shown corresponding to the three boundary condition solutions shown in Figure 3.5. The solution with $\theta_{L_2} = 84.4°$ is reached by rotating α_1 in the negative direction to $\alpha_1 = -180°$, and the solution $\theta_{L_2} = 275.6°$ is be reached by rotating α_1 in the positive direction to $\alpha_1 = 180°$. The solution with $\theta_L = 180°$ is the trivial (unstable) solution, with the tubes undergoing no torsion.

the particular configuration (solution) taken by the cannula will depend on actuator history. We illustrate this phenomenon in our example below. The inner wire is rotated to an angle of $\alpha_1 = -180°$, while the outer tube stays at $\alpha_2 = 0°$, making $\theta_0 = 180°$. The boundary condition residual is depicted in Figure 3.5 with respect to θ_{L_2}. Note that there are 3 places where the graph crosses the x-axis, representing three different solutions, corresponding to the three different configurations shown in Figure 3.4. The solution at $\theta_{L_2} = 180°$ is a trivial solution to the differential equation, representing the case where neither tube undergoes any torsion (a torsionally rigid model would produce this result). This is an unstable configuration in that the cannula will snap to one of the other solutions if perturbed slightly. The cannula will reach the $\theta_{L_2} = 84.4°$ solution if the actuator starts at $\alpha_1 = 0°$ and increases α_1 continuously until $\alpha_1 = 180°$. If the actuator decreases continuously from $\alpha_1 = 0°$ to $\alpha_1 = -180°$, the solution $\theta_{L_2} = -84.4°$ will be reached, which corresponds to the $\theta_{L_2} = 275.6°$ solution for $\alpha_1 = 180°$. In order to find the value of θ_{L_2} which corresponds to the actual configuration of the cannula, it is helpful to start simulating at a known configuration for which there is only one solution (e.g. $\theta_0 = 0$). Then, by undergoing incremental changes in θ_0, the solution for θ_L at the previous step can be used as the initial guess for the current configuration. This results in the simulation portraying the same solution as the physical cannula until a bifurcation in the cannula energy is reached (where the current solution vanishes – see [94]) and the cannula "snaps around" to a new solution.

For the a simple, two tube, circular precurvature case we are currently considering, it is possible to predict analytically when multiple solutions will exist (see [27] for an alternate derivation of the following result). For $\theta_0 = 180°$ (the angular input where multiple solutions will first exist) we can examine the integral in Equation 3.35 to determine whether multiple solutions are possible. If $\theta_L = 180°$, the integral is zero by definition, which means cannulas of any overlapped length have a solution $\theta_L = 180°$. For $\theta_L \neq 180°$, the integral has a lower bound of $\pi/2$, which can be seen in Figure 3.6 and is shown in (3.38). Thus, by rearranging (3.35) and applying this inequality, it can be seen that for cannulas with a value of $L\sqrt{a} < \pi/2$, only the trivial solution exists.

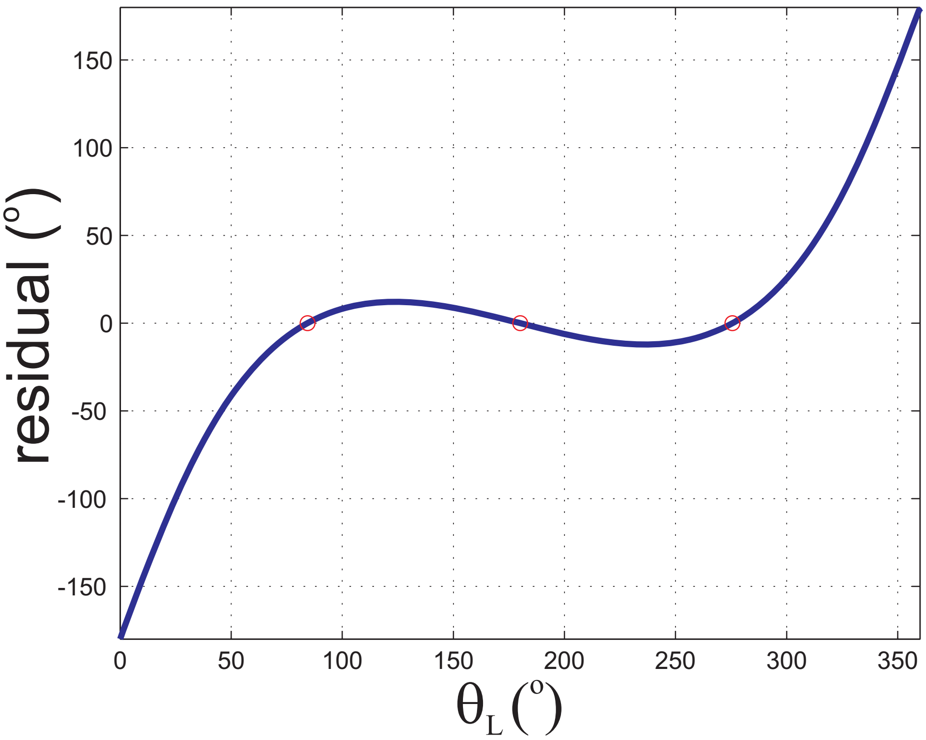

Figure 3.5: The boundary condition residual is plotted versus θ_L for the tubes in Table 3.1 and $\theta_0 = 180°$. Solutions for θ_L are shown at $\theta_L = 180°$, $\theta_L = 84.4°$, and $\theta_L = 275.6°$.

On the other hand, if $L\sqrt{a} \geq \pi/2$, two nontrivial solutions also exist, symmetric about $\theta_L = 180°$. Thus, as shown in (3.39), the dimensionless parameter $L\sqrt{a}$ - which is composed of the overlapped length, stiffness, and curvature of the tubes - can be used to predict whether a two tube cannula will exhibit multiple solutions and thus have the potential to "snap" from one stable solution to another.

To summarize our multiple solutions discussion above, we have the inequality

$$\pi/2 \leq \left| \int_0^{\Phi(L)} \frac{d\theta}{\sqrt{1 - k^2 \sin^2(\Phi)}} \right| \quad \forall \theta_L \neq 180°, \tag{3.38}$$

which when combined with (3.35) yields the conditions:

$$\begin{aligned} L\sqrt{a} < \pi/2 &\rightarrow \text{ only one solution} \\ L\sqrt{a} \geq \pi/2 &\rightarrow \text{ multiple solutions exist} \end{aligned} \tag{3.39}$$

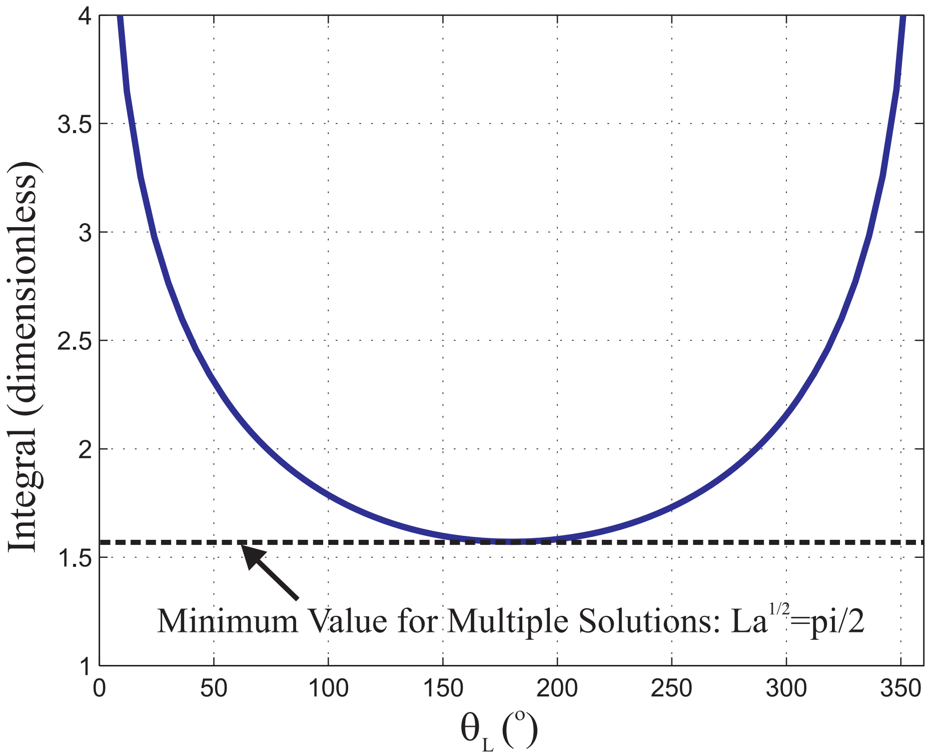

Figure 3.6: For $\theta_0 = 180°$ the value of the integral in (3.38) is shown in blue as a function of θ_L ranging from 0° to 360°. Because it is lower bounded by $\frac{\pi}{2}$, the dimensionless parameter $L\sqrt{a}$ can be used to predict when multiple solutions can occur.

As shown in Figure 3.4, the two solutions with torsion are significantly different than the no torsion solution. Thus torsion in the overlapping curved section can be very important for determining overall shape. Still, it would appear that each section is very close to circular, suggesting that some kind of adjustment to a piecewise circular model could be an effective way to compensate for torsion in the curved sections. Modeling the individual sections of an active cannula as circular arcs leads to very convenient kinematic formulations that have been widely exploited in prior work (e.g. [31, 72, 94], etc. – see also [90] for an overview of piecewise constant curvature kinematics for continuum robots). However, the presence of torsion can, in some cases, lead to curved shapes that are qualitatively different and which cannot

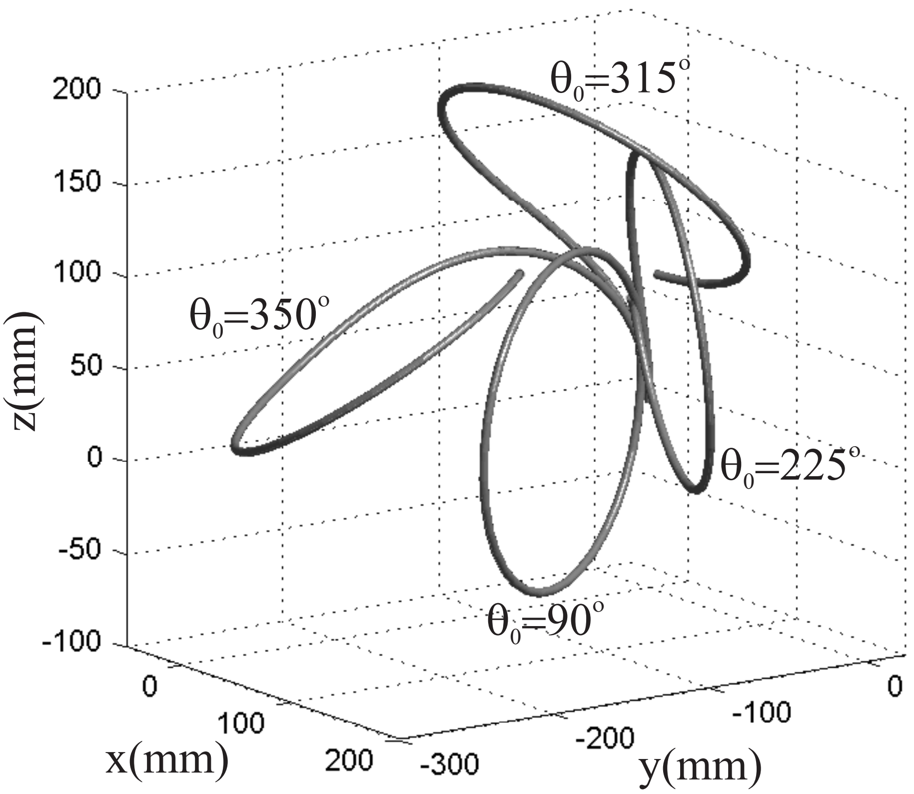

Figure 3.7: Shown above are four configurations of a simulation of two fully precurved, fully overlapping tubes, whose material properties are given in Table 3.1. Both tubes have a longer arc length of 636.5 mm (equal to one full circle of the outer tube). The inner wire is rotated in the positive direction to angles of 90°, 225°, 315°, and 350° at the base. It is evident that in extreme cases, circular tubes with precurvature can form highly non-circular shapes when combined due to the effects of torsion.

be approximated well by circular arcs. If the overlapped arc length is long or the curvatures are large, torsional relaxation makes it possible to obtain highly non-circular shapes from two circularly precurved tubes. To illustrate this, we extend the curved portions of both tubes used in our first example to 636.5 mm (corresponding to one full circle of the outer tube) and rotate the inner wire from $\alpha_1 = 0°$ to $\alpha_1 = 350$. The resulting shape is shown in Figure 3.7, where the inner wire has been rotated in the positive direction to angles of 90°, 225°, 315°, and 350° at the base. It is clear from Figure 3.7 that the resulting shape cannot be well approximated by a circle. How-

Table 3.2: Measured and Assumed Physical Quantities for Experimental Tube and Wire.

	Outer Tube	Inner Wire
Young's Modulus (GPa)	58	58
Shear Modulus (GPa)	21.5	21.5
Inner Diameter (mm)	2.01	0
Outer Diameter (mm)	2.39	1.60
Straight Length (mm)	93.5	218.5
Curved Length (mm)	92.3	85
Curvature (1/mm)	0.0099	0.0138

ever, for cannulas of sufficiently short curved overlap and sufficiently small curvature, piecewise circular models are reasonably accurate at predicting cannula shape. Such was the case for many prior prototypes (e.g. [72, 94]).

3.3 Experimental Validation of the Kinematic Model

In this section we will compare the predictions of three available models for active cannula shape with a set of experiments on a prototype cannula. The three models are the "bending only" model [72], the "transmissional torsion" model [92–94], and the model provided in Section 3.2.5. The experimental data set used here is the same as that provided in [94]. As described in [94], these experiments use an active cannula constructed of one tube and one wire, each of which has an initial straight transmission, followed by a circularly curved section near its tip.

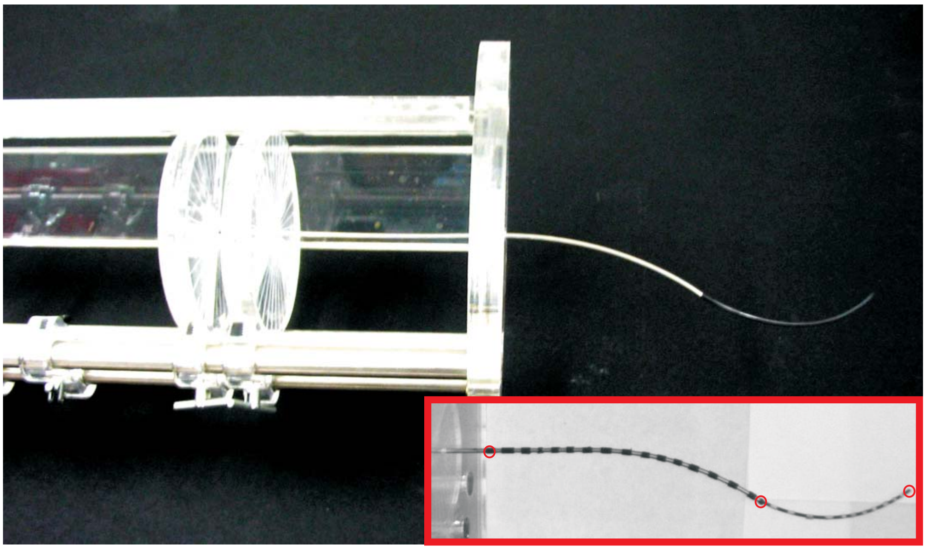

Figure 3.8: Manual actuation mechanism used in experiments. In this apparatus, both tube and wire are affixed to circular acrylic input handles at their bases, which are etched to encode rotation. The support structure is etched with a linear ruler to encode translation. Spring pin locking mechanisms lock the input discs at desired linear and angular input positions. The inset image of a striped cannula on a white background is an example of an image captured using one of our calibrated stereo cameras. The black bands seen are electrical tape and allow for point correspondences to be identified for stereo triangulation. The red circles indicate the locations at which euclidean errors were calculated. Calibration of model parameters was done to minimize the sum of these errors over all experiments.

3.3.1 Experimental Dataset

Here, we summarize the experimental data set (the dataset from [94]) which was used to compare the model given in Section 3.2 with transmissional torsion model. In these experiments, an outer tube and an inner wire were arranged in two different translational positions and a range of input angles were applied. The two translational positions were referred to as the "full overlap case" and the "partial overlap case". In the full overlap case, the tube and wire were arranged so that the link lengths were as follows: $10mm$ (tube curved, wire straight), $82.3mm$ (both curved), and $2.7mm$ (only wire present). For the full overlap case, data was recorded for 15 different input

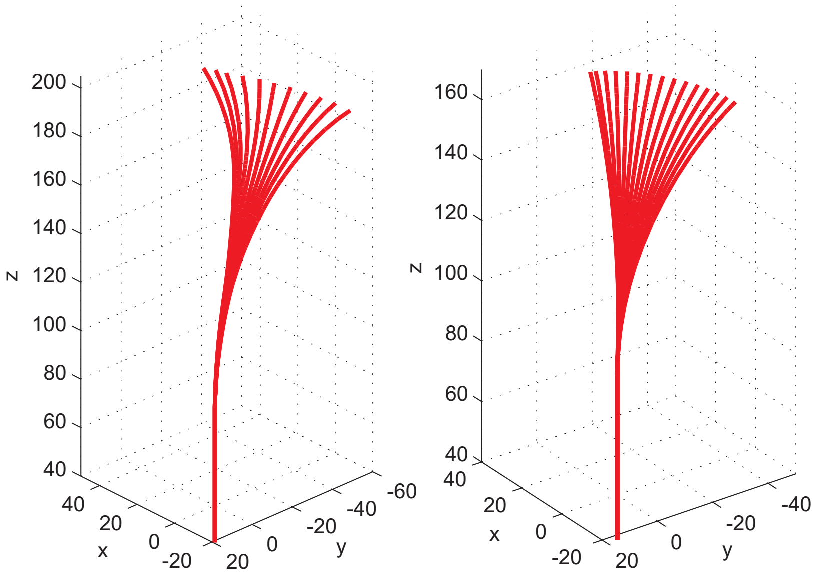

Figure 3.9: Configuration space covered in experiments. Left: partial overlap case, Right: full overlap case.

angles ranging from 0° to 280° in 20° increments. In the partial overlap case, the tube and wire were arranged so that the section lengths were as follows: $48mm$ (tube curved, wire straight), $44.3mm$ (both curved), and $40.7mm$ (only wire present). For this overlap configuration, data was recorded for 11 different input angles ranging from 0° to 200° in 20° increments. The workspace range covered by these actuation inputs is depicted in Figure 3.9.

3.3.2 Procedure and Model Calibration

Each of the above configurations were input to the base of the cannula tube and wire using the manual actuation unit shown in Figure 3.8. For each, the resultant overall shape of the cannula was recorded via a calibrated pair of stereo cameras (Sony XCD-X710 firewire cameras with a resolution of 1024 × 768 pixels). The fiducial markers shown in the inset image in Figure 3.8 enabled determination of

Table 3.3: Nominal and Calibrated Dimensionless Parameters

Parameter	Nominal Value	Calibrated Value
c_1	0.350	0.451
c_2	0.350	0.449
c_3	0.287	0.341

point correspondences for stereo triangulation, after they had been identified in image coordinates by manually clicking on the center of the black bands in video frames. One source of error in this data collection procedure is the accuracy of manual point selection in images, which is estimated to be approximately 2 pixels or 0.6 mm. Another is fiducial size (they are not infinitesimal points), causing small differences in intended selection locations. We estimate that fiducial dimensions introduce error of approximately the diameter of the wire itself (1.6 mm). Based on these, our overall vision system measurement error is approximately 2.2mm, in a worst-case sense.

The nominal physical properties of the tube and wire used in our experiments are given in Table 3.2. We compare the model of Section 3.2.5 with the prior transmissional torsion model using both the nominal values given in Table 3.2 and calibrated parameters (a calibration procedure for the transmissional torsion model is provided in [94]). Examining the equations in Section 3.2.5, we see that the stiffness coefficients in Equations 3.15 and 3.29 can be expressed in terms of the three dimensionless parameters

$$c_1 = \nu_1, \quad c_2 = \nu_2, \quad \text{and} \quad c_3 = \frac{E_1 I_1}{E_1 I_1 + E_2 I_2}. \tag{3.40}$$

Poisson's ratio is often taken to be approximately 0.35 for Nitinol. It has also been noted that plastic deformation can increase Poisson's ratio for Nitinol to 0.5 [95]. Since we pre-shaped our tubes via plastic deformation, we will assume a range of 0.30 to 0.50. An expected range for c_3 can be deduced from the uncertainty in each quantity upon which it depends. Nitinol dimensions are specified by the manufacturer (Nitinol Devices and Components, Inc.) to ±0.0010 in., while the elastic modulus E is reported as 41 to 75 GPa. Applying standard error propagation, the expected range for parameter c_3 is 0.143 to 0.431.

These ranges provide a basis for comparison with fitted parameter values produced by the parameter fitting procedure. To calibrate the parameters, we minimize the sum of the positional errors at the tip of the wire, the tip of the tube and the measured point most near the base, as shown in Figure 3.8. Matlab's `fmincon` function was used to optimize the values of the three dimensionless parameters given in (3.40) with upper and lower bounds set to the expected ranges of the parameters. As described in [94], the transformation between the stereo camera coordinate frame and a frame fixed at the base of the cannula was first estimated using point cloud registration [7]. Images of a 15-mm checkerboard pattern (with corners at known physical locations with respect to the cannula base frame) were captured. Sixteen corners on the checkerboard were triangulated with the stereo vision system. This registration was only expected to provide a rough estimate of the frame transformation. Thus, six "nuisance parameters" (a 3-vector for position and a 3-vector for orientation with magnitude of rotation encoded as length) describing the cannula base frame were included in the calibration procedure and initialized with the results from

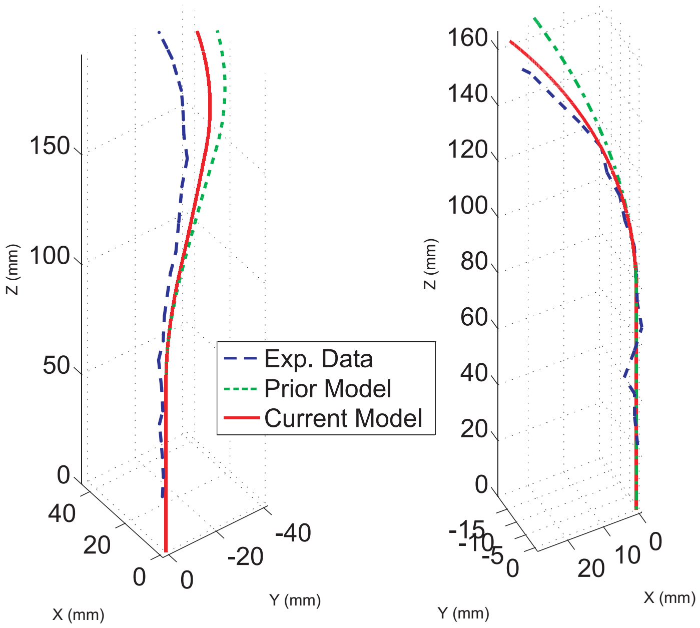

Figure 3.10: Comparison of shape for the transmissional torsion model (green – dotted line) with nominal parameters, the model given in Section 3.2.5 (red – solid line) with nominal parameters, and experimental data (blue – dashed line) for configurations near the edge of the active cannula workspace. Note that the model given in Section 3.2.5 produces predictions closer to experimentally observed cannula shape. Left: partial overlap case, Right: full overlap case.

the point cloud registration. Nuisance parameters showed only small changes during optimization, with cannula base frame moving only 0.5 mm, and rotating through X-Y-Z Euler Angles of $\alpha = 0.9°$, $\beta = 0.3°$, $\gamma = 4.0°$.

3.3.3 Results

The calibrated parameter values are given alongside their nominal values in Table 3.3, and we note that they fall well within their expected ranges and converge to near the same values for initial guesses in a range within ±5% of the optimal values. In [94] calibration led to one of the parameters falling outside its expected range, which illustrates that the model presented in this chapter more completely captures

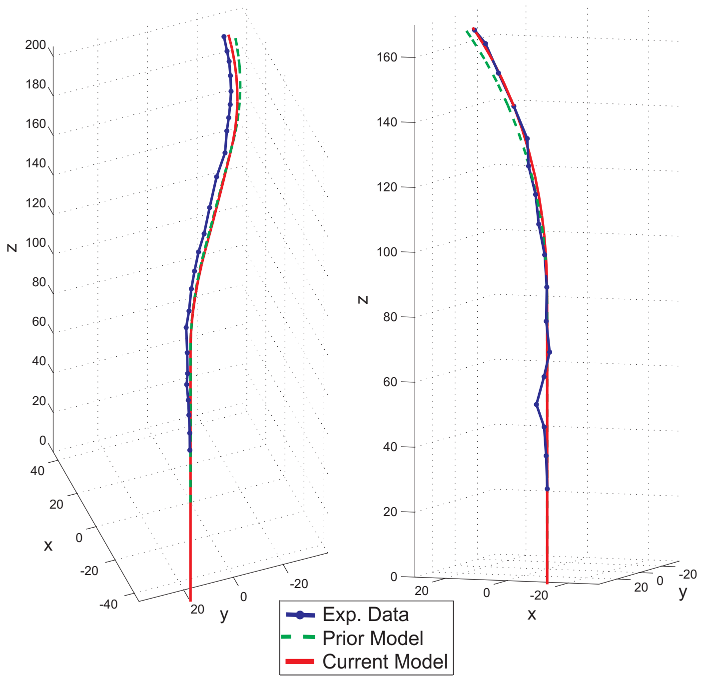

Figure 3.11: Comparison of shape for the transmissional torsion model (green – dotted line) with calibrated parameters, the model given in Section 3.2.5 (red – solid line) with calibrated parameters, and experimental data (blue – dashed line) for configurations near the edge of the active cannula workspace. Note that the model given in Section 3.2.5 produces predictions closer to experimentally observed cannula shape. Left: partial overlap case, Right: full overlap case.

the underlying mechanics. Note that the unmodeled presence of friction would have a similar effect on our data as lowering the torsional rigidity of the tubes, namely increasing torsional windup. Thus, the calibration process would tend to increase c_1 and c_2 to compensate for frictional effects. This may account for the slightly high values of c_1 and c_2, but they are nevertheless still within their expected ranges.

This is also supported by the data in Table 3.4. When using nominal parameters from data sheets, the model of Section 3.2.5 is significantly more accurate than the transmissional torsion model. Specifically, the model of Section 3.2.5 results in an average tip error of only 4.72 mm as opposed to 10.1 mm for the transmissional model. Figure 3.10 shows the experimental data and the predictions of both models using

Table 3.4: Tip Error Statistics (Uncalibrated/Calibrated) for Current Model Compared to Prior Models

	Mean Tip Error (mm)	Max Tip Error (mm)
Bending Only Model	24.8/13.6	54.3/31.5
Transmissional Torsion Model	10.1/3.0	22.1/8.8
Model of Section 3.2.5	4.7/2.5	12.7/7.1

nominal parameters for the two worst experimental cases, where angular input angle differences are at the edge of the workspace and torsion is most significant. These are 280° in the full overlap case, and 200° in the partial overlap case.

Quantitatively, the model of Section 3.2.5 with calibrated parameters exhibits a mean tip error of 2.5 mm across all experiments with a maximum tip error of 7.1 mm, as shown in Table 3.4). In comparison, the calibrated transmissional torsion model exhibits a mean of 3.0 mm and a maximum of 8.8 mm, and the bending only model a mean of 13.6 mm and a maximum of 31.5 mm. With calibrated parameters, the model of Section 3.2.5 improves the mean tip error 82% over the bending only model, and 17% over the transmissional torsion model.

Plots of the experimental data and the predictions of both models using calibrated parameters are shown in Figure 3.11, picturing the same two "worst-case" experiments shown in Figure 3.10. The behavior pictured is common to all experimental positions using either calibrated or uncalibrated parameters, namely that the prediction of the model of Section 3.2.5 lies nearer the experimental data than the transmissional torsion model prediction. Note also that the predictions of the bending only model are not shown in for clarity, since they are sufficiently far from the experimental data that they would obscure the differences between the other two models. As discussed in [94], the bending only model neglects the torsional windup that occurs in an active cannula, so its predictions become increasingly structurally incorrect as the angle input difference increases. These quantitative results also indicate that the general modeling framework is providing enhanced predictive ability by reducing tip error.

3.3.4 Conclusions

We have presented a general model formulation for computing the shape of concentric-tube continuum robots. This model can account for precurvatures and stiffnesses that vary along the length of component tubes, and it explicitly takes torsion into account throughout the entire device.

We also showed via simulation and experiments that the new model described in this chapter captures the underlying mechanics of the cannula more accurately than prior models. This was illustrated in simulation by the fact that tubes with circular precurvatures can combine to form a dramatically different shape if torsion is allowed in curved sections. In the experiments it was shown that the model parameter values fell within their expected ranges after calibration to the experimental data, which was not the case for the model with only transmissional (straight section) torsion.

As a tool to simulate possible designs and judge their merits in comparison to design goals, this new model may have significant implications for active cannula applications in both medicine and industry. Since accounting for torsion significantly increases model accuracy, this model enables active cannulas to be used in applications which demand increasing accuracy. Furthermore, active cannulas with variable precurvatures will be able to reach further and through more complex trajectories while using fewer tubes. This new model also facilitates future studies on patient-specific preshaping of active cannula component tubes, so that one may match the capabilities of the device to the particular location and entry trajectory required by a specific patient.

An important area of further development is the development of concentric-tube robot models that consider external loading. The next section addresses this problem by expanding upon the kinematic model using Cosserat-rod theory to describe large robot deformations due to external loading conditions.

3.4 Model with External Loading

The mechanics-based model developed in the first half of this chapter describes the shape of a concentric-tube continuum robot, or "active cannula", in free-space as a function the preset tube shapes and the linear and angular positions of the tube bases. In many practical applications where the active cannula must interact with its environment, a model that additionally accounts for the effects of external loading will be necessary in order to control the robot accurately and develop new capabilities like force-sensing and force control. In this chapter we apply geometrically exact rod theory to produce a forward kinematic model that accurately describes the large deflections of a concentric-tube robot due to a general collection of externally applied point and/or distributed wrench loads. Like the free-space model in the previous sections of this chapter, this model accommodates any number of generally pre-shaped tubes and describes the independent torsional deformations of the individual tubes. Experimental results confirm that the model with external loading is accurate for both point and distributed loads. Average tip error under load was 2.91 mm (1.5 – 3% of total robot length).

Our model for externally loaded concentric tube robots is based on combining classical Cosserat rod theory, which is detailed in Chapter 2, with the concentricity constraints which are detailed in Section 3.2.3 of this chapter. We first summarize our assumptions below and give the relevant Cosserat-rod equations from Chapter 2 and which we apply to each tube in the robot. Then, applying the concentricity constraints to these equations, we obtain a system of differential equations that describes the shape of the robot under external loading.

3.4.1 Assumptions

With respect to constitutive behavior, we use the standard assumptions of the classical elastic rod theory of Kirchoff, a special case of Cosserat rod theory [3]. The assumptions of Kirchoff are (1) inextensibility and no transverse shear strain, and (2) linear constitutive equations for bending and torsion. Inextensibility and shearlessness are generally regarded to be good assumptions for long thin rods such as the tubes in active cannulas (e.g. the prototype described in Section 3.5), To illustrate the validity of the inextensibility assumption, we provide the following calculation. The maximum insertion force for the inner tube of our prototype was measured to be 10.1 N using an ATI Nano17 force sensor, a number which also exceeds any of the applied loads in our experiments. If this load was applied at both ends of a straight tube with the same dimensions as the inner tube used in our experiments, the total elongation would be less than 50 micrometers. Thus, we can be confident that bending and torsion will dominate the deformation behavior of an active cannula. For simplicity we adopt the linear constitutive equations, but our overall approach does not require it. Active cannulas often remain below 3% strain in practical use, which is in the linear range of Nitinol [103].

We also neglect friction in this model, as do all active cannula models to date. While friction is a worthy topic of future modeling and compensation efforts, the fact that we can achieve less than 3 mm average tip error without modeling friction indicates that its effects do not dominate the behavior of our experimental prototype. Furthermore, we explored hysteresis with our experimental prototype and noted no discernible effects, i.e. we could not induce the cannula to reach a different final position under load when the load was allowed to oscillate. We will comment further upon how frictional effects might be added to our modeling framework in the future in the conclusion section of this chapter.

3.4.2 Single Tube Equations

As in the free-space model, we let the unloaded precurved shape of a tube be defined by an arc-length parameterized curve $\boldsymbol{p}^*(s)$, and we assign frames continuously along $\boldsymbol{p}^*(s)$, choosing the z axes of these frames to always be tangent to the curve. Thus, a continuous homogeneous transformation $g^*(s)$ is established, consisting of the position and orientation of an arc length parameterized reference frame along each tube,

$$g^*(s) = \begin{bmatrix} R^*(s) & \boldsymbol{p}_i^*(s) \\ 0 & 1 \end{bmatrix}. \tag{3.41}$$

We then obtain the local pre-curvature vector by using the kinematic relationship

$$\boldsymbol{u}^*(s) = \left(R^{*\mathrm{T}}(s)\dot{R}^*(s)\right)^{\vee}.$$

The deformed backbone shape of each tube, $g(s)$, is then defined differentially by

$$\dot{g}(s) = g(s)\widehat{\boldsymbol{\xi}}(s),$$

where $\boldsymbol{\xi}(s) = \begin{bmatrix} \boldsymbol{e}_3^{\mathrm{T}} & \boldsymbol{u}^{\mathrm{T}}(s) \end{bmatrix}^{\mathrm{T}}$, or equivalently

$$\boldsymbol{p}(s) = R(s)\boldsymbol{e}_3, \quad \dot{R}(s) = R(s)\widehat{\boldsymbol{u}}(s), \tag{3.42}$$

where $\boldsymbol{u}(s) = \boldsymbol{u}^*(s) + \Delta\boldsymbol{u}(s)$ is the curvature vector of the deformed backbone curve, and $\boldsymbol{v} = \boldsymbol{v}^* = \boldsymbol{e}_3$ because of the Kirchoff assumptions, arc-length parameterization, and the z-axis tangent convention.

We use a linear constitutive law to describe the relationship of the strains to the internal moment vector (expressed in global frame coordinates) at s:

$$\boldsymbol{m}(s) = R(s)K(s)\Delta\boldsymbol{u}(s), \tag{3.43}$$

where

$$K(s) = \begin{bmatrix} E(s)I(s) & 0 & 0 \\ 0 & E(s)I(s) & 0 \\ 0 & 0 & G(s)J(s) \end{bmatrix},$$

$E(s)$ is Young's modulus, $I(s)$ is the second moment of area of the tube cross section, $G(s)$ is the shear modulus, and $J(s)$ is the polar moment of inertia of the tube cross section. Note that since we assume zero shear and extension, we have replaced $K_{BT}(s)$ with $K(s)$ in this chapter.

As detailed in Chapter 2, the classic Cosserat-rod equilibrium equations are obtained by taking the arc-length derivative of the static equilibrium conditions on a section of rod, yielding

$$\dot{\boldsymbol{n}}(s) + \boldsymbol{f}(s) = \boldsymbol{0}. \tag{3.44}$$

$$\dot{\boldsymbol{m}}(s) + \dot{\boldsymbol{p}}(s) \times \boldsymbol{n}(s) + \boldsymbol{l}(s) = \boldsymbol{0}. \tag{3.45}$$

Combining the kinematics with the equilibrium and constitutive laws, we can write (3.44) and (3.45) in terms of the kinematic variables using (2.12), their derivatives with respect to s, and the differential geometric relationships $\dot{R} = R\widehat{\boldsymbol{u}}$ and $\dot{\boldsymbol{p}} = R\boldsymbol{e}_3$ from (2.5). After algebraic manipulation, this yields the full set of differential equations shown below is obtained, assuming that K is constant with respect to s:

$$\begin{aligned}
\dot{\boldsymbol{p}} &= R\boldsymbol{e}_3 \\
\dot{R} &= R\widehat{\boldsymbol{u}} \\
\dot{\boldsymbol{n}} &= -\boldsymbol{f} \\
\dot{\boldsymbol{u}} &= \dot{\boldsymbol{u}}^* - K^{-1}\left(\widehat{\boldsymbol{u}}K\left(\boldsymbol{u}-\boldsymbol{u}^*\right) + \widehat{\boldsymbol{e}}_3 R^T\boldsymbol{n} + R^T\boldsymbol{l}\right)
\end{aligned} \tag{3.46}$$

Alternatively, an equivalent system can be obtained using $\boldsymbol{m}$ as a state variable rather than $\boldsymbol{u}$:

$$\begin{aligned}
\dot{\boldsymbol{p}} &= R\boldsymbol{e}_3, \\
\dot{R} &= R\widehat{\boldsymbol{u}}, \qquad \text{where } \boldsymbol{u} = K_{BT}^{-1}R^T\boldsymbol{m} + \boldsymbol{u}^* \\
\dot{\boldsymbol{n}} &= -\boldsymbol{f} \\
\dot{\boldsymbol{m}} &= -\dot{\boldsymbol{p}} \times \boldsymbol{n} - \boldsymbol{l}
\end{aligned} \tag{3.47}$$

Typical boundary conditions for this a simple cantilevered case would be $g(0) = g_0$, $\boldsymbol{n}_i(\ell) = \boldsymbol{F}_{tip}$, and $\boldsymbol{m}_i(\ell) = \boldsymbol{L}_{tip}$ where $\boldsymbol{F}_{tip}$ and $\boldsymbol{L}_{tip}$ are applied point force and point moment vectors at $s = L$. We note that the equation for $\dot{\boldsymbol{n}}$ is linear and decoupled from the rest of the equations and may be directly integrated to obtain $\boldsymbol{n}$.

3.4.3 Concentric Constraints and Multi-Tube Equations

We now consider a robot composed of a collection of precurved concentric tubes subject to a set of external forces and moments along its length. We first review the concentric constraints derived in the first half of this chapter, and then derive a set of multi-tube model equations analogous to (3.46) and (3.47).

As in the free-space model, we assign each tube has its own arc length parameterized transformation $g_i^*(s)$ as in (3.41), and associated precurvature vectors $\boldsymbol{u}_i^*(s)$.

The reference frames of each tube are then related to that of the first tube by an angle $\theta_i(s)$ about the z-axis, and to the backbone bishop frame by an angle $\psi(s)$.

$$R_i(s) = R_1(s)R_{\theta_i} = R_B(s)R_{\psi_i}, \tag{3.48}$$

This implies the following constraint on the tube curvatures:

$$\boldsymbol{u}_i = R_{\theta_i}^T \boldsymbol{u}_1 + \dot{\theta}_i \boldsymbol{e}_3 = R_{\psi_i}^T \boldsymbol{u}_B + \dot{\psi}_i \boldsymbol{e}_3. \tag{3.49}$$

We note that the third component of (3.49) gives us

$$\dot{\theta}_i = u_{i,z} - u_{1,z}, \quad \text{and} \quad \dot{\psi}_i = u_{iz}. \tag{3.50}$$

We can sum (3.44) and (3.45) over all the tubes to obtain a set of equilibrium equations for the entire collection of tubes at a given location on the robot:

$$\sum_{i=1}^{n} (\dot{\boldsymbol{n}}_i + \boldsymbol{f}_i) = \boldsymbol{0}, \tag{3.51}$$

$$\sum_{i=1}^{n} (\dot{\boldsymbol{m}}_i + \dot{\boldsymbol{p}} \times \boldsymbol{n}_i + \boldsymbol{l}_i) = \boldsymbol{0}, \tag{3.52}$$

where we have recognized that $\boldsymbol{p}_1 = \boldsymbol{p}_2 = ... = \boldsymbol{p}_n = \boldsymbol{p}$.

As in the single tube case, we can now apply the expand (3.52) by using the constitutive law (3.43) and the kinematic relationship (3.42) for each tube to write

$$\sum_{i=1}^{n} \dot{\boldsymbol{m}}_i(s) = \sum_{i=1}^{n} R_i \Big(K_i \left(\dot{\boldsymbol{u}}_i - \dot{\boldsymbol{u}}_i^*\right) + \hat{\boldsymbol{u}}_i K_i \left(\boldsymbol{u}_i - \boldsymbol{u}_i^*\right) \Big),$$

assuming that K_i is constant with respect to s. We then use the derivative of the concentric constraint equation (3.49),

$$\dot{\boldsymbol{u}}_i(s) = \dot{\theta}_i \frac{dR^{\mathrm{T}}_{\theta_i}}{d\theta_i}\boldsymbol{u}_1 + R^{\mathrm{T}}_{\theta_i}\dot{\boldsymbol{u}}_1 + \ddot{\theta}_i\boldsymbol{e}_3, \tag{3.53}$$

to eliminate $\dot{\boldsymbol{u}}_2, ...\dot{\boldsymbol{u}}_n$ from (3.52). This substitution enables us to solve (3.52) for the first two components, $\dot{u}_{1,x}$ and $\dot{u}_{1,y}$.

$$\begin{aligned}\dot{\boldsymbol{u}}_{1xy} = -K^{-1}\sum_{i=1}^{n} R_{\theta_i}\Big(K_i(\dot{\theta}_i\frac{dR^{\mathrm{T}}_{\theta_i}}{d\theta_i}\boldsymbol{u}_1 - \dot{\boldsymbol{u}}^*_i) + \hat{\boldsymbol{u}}_i K_i(\boldsymbol{u}_i - \boldsymbol{u}^*_i)\Big)\Big|_{x,y} \\ -K^{-1}\Big(\widehat{\boldsymbol{e}}_3 R_1^T \boldsymbol{n} + R_1^T \boldsymbol{l}\Big)\Big|_{x,y}\end{aligned} \tag{3.54}$$

where $\boldsymbol{n}(s) = \sum_{i=1}^{n}\boldsymbol{n}_i(s)$, $\boldsymbol{l}(s) = \sum_{i=1}^{n}\boldsymbol{l}_i(s)$, $K = \sum_{i=1}^{n} K_i$ and $|_{x,y}$ denotes selection of only the first two components of a vector.

Now, since equation (3.45) applies to each individual tube, we multiply both sides by $\boldsymbol{e}_3^T R_i^T$ and expand using the constitutive law and the kinematic equations to obtain

$$\dot{\boldsymbol{u}}_{iz} = \dot{\boldsymbol{u}}^*_{iz} + \frac{E_iI_i}{G_iJ_i}\left(u_{ix}u^*_{iy} - u_{iy}u^*_{ix}\right) - \frac{1}{G_iJ_i}\boldsymbol{l}_i^T R_i \boldsymbol{e}_3. \tag{3.55}$$

This torsional behavior completes our multi-tube model, so that we now have first order state equations for the variable set $\{\boldsymbol{p}, R_1, \boldsymbol{n}, u_{1x}, u_{1y}, u_{2z}, ..., u_{nz}, \theta_2, ...\theta_n\}$. The equations that define their derivatives are (3.42), (3.44), (3.54), (3.55), and (3.50). The intermediate variables $\boldsymbol{u}_i$ can be calculated directly from $\boldsymbol{u}_1$ at every step using (3.49).

Alternate Formulation

We can write an alternate formulation of our externally loaded model by using the constitutive law to expand the internal moment carried by the entire collection of tubes.

$$\boldsymbol{m} = \sum_{i=1}^{n} \boldsymbol{m}_i = \sum_{i=1}^{n} R_i K_i \left(\boldsymbol{u} - \boldsymbol{u}^*\right)$$

We define $\boldsymbol{m}^b$ as the total moment $\boldsymbol{m}$ expressed in the frame of tube 1, $\boldsymbol{m}^b = R_1^T \boldsymbol{m}$, so that

$$\boldsymbol{m}^b = \sum_{i=1}^{n} R_{\theta_i} K_i \left(\boldsymbol{u} - \boldsymbol{u}^*\right).$$

By applying the concentric constraint (3.49), we can solve for the x and y components of the first tube's curvature vector in terms of the x and y components of $\boldsymbol{m}^b$, and the pre-curvatures:

$$\boldsymbol{u}_{1xy} = \frac{1}{\sum_{k=1}^{n} E_k I_k} \left(\boldsymbol{m}_{xy}^b + \sum_{j=1}^{n} R_{\theta_j} E_j I_j \boldsymbol{u}_{jxy}^* \right). \tag{3.56}$$

The x and y components of the i^{th} tube's curvature vector is then obtained by

$$\boldsymbol{u}_{ixy} = R_{\theta_i}^T \boldsymbol{u}_{1xy}. \tag{3.57}$$

Using the equations derived in the previous section, the above results allows us to write the model equations as

$$\begin{aligned}
\dot{\boldsymbol{p}} &= R_1 \boldsymbol{e}_3 \\
\dot{R}_1 &= R_1 \widehat{\boldsymbol{u}}_1 \\
\dot{\theta}_i &= u_{iz} - u_{1z} \\
\dot{u}_{iz} &= \dot{u}_{iz}^* + \frac{E_i I_i}{G_i J_i} \left(u_{ix} u_{iy}^* - u_{iy} u_{ix}^* \right) - \frac{1}{G_i J_i} \boldsymbol{l}_i^T R_1 \boldsymbol{e}_3. \\
\dot{\boldsymbol{n}} &= -\boldsymbol{f} \\
\dot{\boldsymbol{m}}_{xy}^b &= \left(-\widehat{\boldsymbol{u}} \boldsymbol{m}^b - \widehat{\boldsymbol{e}}_3 R_1^T \boldsymbol{n} - R_1^T \boldsymbol{l} \right) \Big|_{xy}
\end{aligned} \tag{3.58}$$

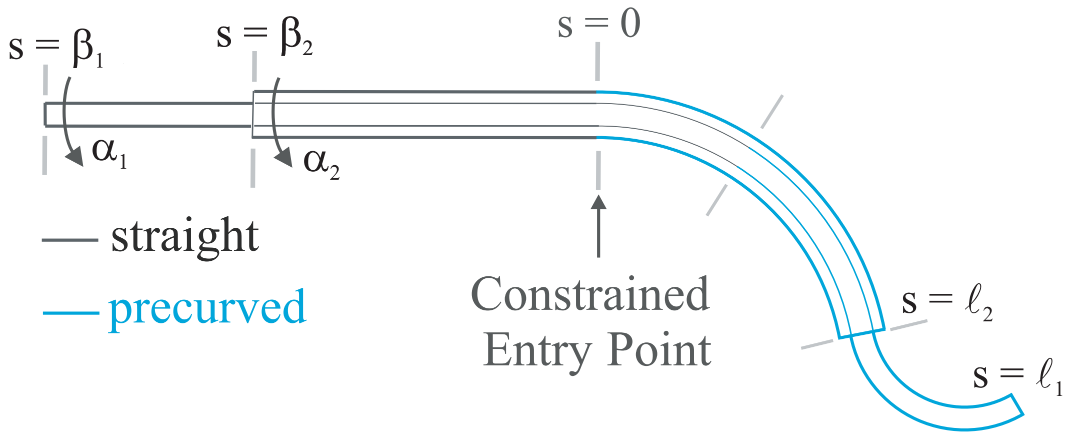

Figure 3.12: Diagram of a two tube cannula showing transition points where continuity of shape and internal moment must be enforced. The constrained point of entry into the workspace is designated as the arc length zero position.

where (3.56) and (3.57) are used to obtain the curvature vectors from the state variables. In this form, the state variable set is $\left\{\boldsymbol{p}, R_1, \boldsymbol{n}, \boldsymbol{m}_{xy}^b, u_{1z}, ..., u_{nz}, \theta_2, ...\theta_n\right\}$. A similar formulation was presented by Lock et al. in [50].

3.4.4 Solving the Loaded Model Equations

Nominally, the boundary conditions appropriate for our loaded model are the same as those for the free-space kinematic model, plus new boundary conditions for the new additional variables in the loaded model. Referring again to the diagram of a typical two-tube robot in Figure 3.12, the initial conditions for ψ_i are

$$\psi_i(0) = \alpha_i - \beta_i u_{iz}(0). \tag{3.59}$$

Thus, the initial conditions for $\boldsymbol{p}$ and R_1 are

$$\begin{aligned} \boldsymbol{p}(0) =& \mathbf{0}, \\ R_1(0) =& R_{\psi_1(0)}. \end{aligned} \tag{3.60}$$

In the absence of applied point loads, the torsion-free boundary condition still exists at the end of each tube,

$$u_{iz}(\ell_i) = 0, \tag{3.61}$$

and the moment and force boundary conditions at the very end of the device (the end of tube 1) are

$$\begin{aligned} \boldsymbol{m}(\ell_1) &= 0, \\ \boldsymbol{n}(\ell_1) &= 0. \end{aligned} \tag{3.62}$$

Challenges in practical implementation of our model include numerically dealing with point loads, the issue of tubes undergoing step changes in pre-curvature, and beginning and ending at different arc lengths. All such occurrences should ultimately result in a step change in the deformed curvature. To account for this, we propose solving a series of systems bounded by the discontinuous solution points while enforcing appropriate boundary conditions at the junctions.

Possible discontinuous solution points for a typical two-tube cannula are illustrated by gray lines perpendicular to the cannula in Figure 3.12, which break it into sections. The boundary conditions to be enforced across each transition point between sections (at arc length s) are as follows: (1) the position and orientation of each tube must be continuous across the boundary, so

$$g_i(s^-) = g_i(s^+),$$

and (2) static equilibrium requires that the sum of the internal moments carried by the tubes just before the end of the section equal the sum of the internal moments carried by the tubes just after the end of the section plus the sum of the applied point moments at the boundary (a point moment applied to tube i is denoted by $\boldsymbol{l}_{p,i}(s)$), that is

$$\sum_{i=1}^{n} \boldsymbol{m}_i(s^-) = \sum_{i=1}^{n} \boldsymbol{m}_i(s^+) + \sum_{i=1}^{n} \boldsymbol{l}_{p,i}(s).$$

This enforcement of static equilibrium across discontinuous boundaries is also required in application of Cosserat theory to other types of continuum robots, and forms of these same conditions are also given in [84].

3.5 Experimental Validation of Model with External Loading

In order to validate the model developed in Section 3.4, a set of experiments was performed for a collection of two Nitinol tubes with general precurvatures (see Figure 3.15) in various configurations and under various loading conditions.

3.5.1 Tube Properties and Measurement Procedures

The physical properties of the tubes used are given in Table 3.5. Each tube has an initial straight length followed by a curved section, the curvature of which is shown in Figure 3.15. In our experiments, the outer tube was held stationary in its fully extended position, while the base of the inner tube was translated to 5 different positions, given in Table 3.6. At each of these translational positions, the inner tube was rotated to 8 evenly spaced angular positions, given in Table 3.7[1]. Thus, the

---

[1] $\alpha_1 = 60°$ was substituted for $\alpha_1 = 45°$ when $\beta_1 = -131.7$ mm to keep the tip of the cannula in the field of view of both cameras.

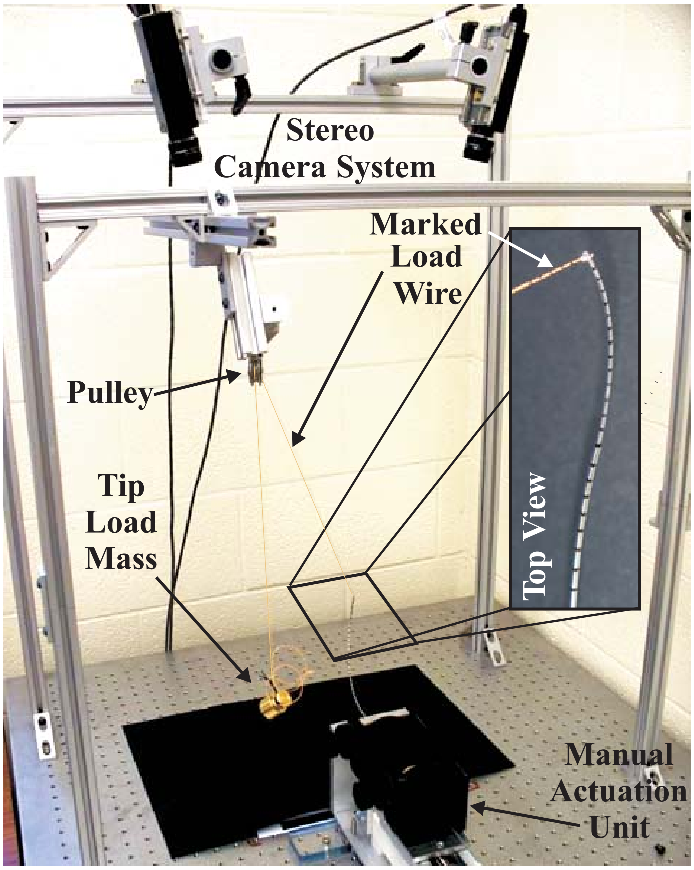

Figure 3.13: Photograph of the experimental setup. Tube bases were translated and rotated precisely by manual actuators. Three-dimensional backbone points were triangulated by identifying corresponding markers along the cannula in stereo images. The vector of the applied force was measured by triangulating positions along the wire which connects the cannula tip (via the pulley) to the applied weight.

tubes were actuated to 40 different workspace locations which evenly span the set of angular and linear differences of tube base positions (see Figure 3.16). The rest of the configuration space could be generated by a rigid rotation of the experimentally sampled space about the base frame z axis, so this set of tube positions evenly samples the unique – from the perspective of the model – configuration space locations.

As shown in Figure 3.13, at each of these configurations, a set of 3D points along the backbone was determined via images taken from a calibrated pair of stereo cameras (Sony XCD-X710 Firewire cameras with a resolution of 1024 × 768 pixels)

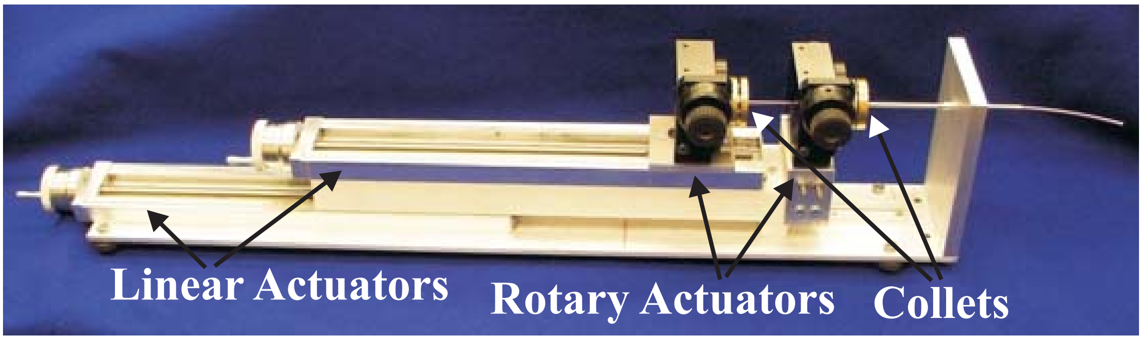

Figure 3.14: Manual actuation unit used to precisely position the bases of the tubes.

Table 3.5: Measured and Assumed Physical Quantities for Experimental Tubes

	Tube 1 (Inner)	Tube 2 (Outer)
Inner Diameter (mm)	1.25	2.00
Outer Diameter (mm)	1.75	2.37
Straight Length (mm)	122.7	30.7
Curved Length (mm)	206.9	102.5
Young's Modulus (E) (GPa)	60	60
Shear Modulus (J) (GPa)	23.1	23.1

mounted above the robot. The fiducial markers shown in the inset image in Figure 3.13 enabled determination of point correspondences for stereo triangulation, after they had been identified in image coordinates by manually clicking on the center of the black bands in each image with Matlab's `ginput` command. The cameras were calibrated using a camera calibration toolbox for Matlab [12], and the transformations between the stereo camera coordinate frames and the robot base frame were initially estimated by triangulating a grid of points with known locations in the base

Table 3.6: Translational Actuator Configurations

β_1 (mm)	-131.7	-154.7	-177.7	-200.7	-223.7
β_2 (mm)	-30.7	-30.7	-30.7	-30.7	-30.7
Tip Load (N)	0.981	0.981	0.981	1.962	4.905

Table 3.7: Rotational Actuator Positions Applied at Each Translational Configuration Shown in Table 3.6

α_1 (deg)	0	45	90	135	180	225	270	315
α_2 (deg)	0	0	0	0	0	0	0	0

frame and performing rigid point cloud registration [7]. The mean, max, min, and standard deviation of the euclidean registration errors were 0.57 mm, 1.30 mm, 0.11 mm, and 0.32 mm respectively. Directionally, the mean registration errors along the x, y, and z axes were 0.50 mm, 0.12 mm, and 0.15 mm respectively, where the x axis points toward the cameras and the z axis points along the robot axis at the base. These numbers encompass the error in the process of manually identifying the pixel coordinates of the points, as well as any error intrinsic to the stereo camera system. We take this to be a rough estimate of the effective accuracy of our vision-based triangulation system.

In each of the 40 actuator configurations, a point force was also applied to the tip of the cannula by a wire tied through a hole in the tip of the inner tube, and backbone data was taken in the robot's loaded state. The direction of the force vector applied by this wire was also determined by triangulating points marked along its length, as shown in Figure 3.13. As can also be seen in the figure, the wire was run over a pulley and attached to a mass ranging from 100 g to 500 g, as detailed in Table 3.6[2]. From the perspective of the cannula, the applied tip load vector was in a different direction in each experiment because the robot was in a different configuration in each.

The pulley was mounted to a 6 DOF manually adjustable frame made from standard 80-20 Inc. parts. In each of the 40 robot configurations, before taking data, the location and angle of the pulley was adjusted as needed to make sure that the cable was orthogonal to the pulley axis. At this time we also checked for hysteresis due to pulley friction by displacing the mass up and down (the flexible cannula acting as a spring) and noting that the pulley always returned to the same equilibrium angle when the weight was released. A subsequent experiment was done using this same procedure, in which the cable tension was measured using a six-axis load cell (Nano17, ATI, Inc.). The resolution of the cable tension was found to be ±0.009 N for the 0.981 N load, ±0.020 N for the 1.962 N load, and ±0.088 N for the 4.905 N load. Thus we conclude that any unmodeled pulley effects did not significantly affect the loads transmitted to the cannula.

The two tubes have general precurvatures $\boldsymbol{u}_1^*(s)$ and $\boldsymbol{u}_2^*(s)$. To obtain these, we began by capturing points along them (individually before inserting one into the other), using the stereo triangulation system in the manner described previously. We then fit a parametric polynomial curve to these points and gathered curvature data from these smooth fits. The components of precurvature for each tube are plotted in Figure 3.15 (the tube curves were framed using Bishop's frames, so there is only

---

[2] In the case where $\beta_1 = -223.7$, $\beta_2 = -30.7$, $\alpha_1 = 0°$, and $\alpha_2 = 0°$, the load was 1.962N

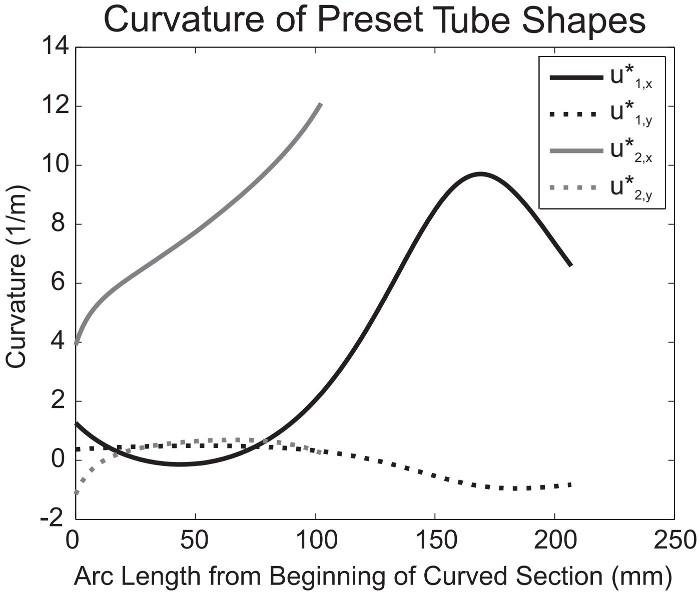

Figure 3.15: Measured curvatures of the preset tube shapes expressed in a Rotation Minimizing frame (Note that for Rotation Minimizing frames, $\boldsymbol{u}^*_{1,z}$ and $\boldsymbol{u}^*_{2,z}$ are zero by definition.)

x and y curvature). Note that the curvatures are not constant over s, and all prior prototypes reported in the literature have had constant curvature pre-set tube shapes.

3.5.2 Model Performance and Calibration

Since model error nearly always increases with the arc length along the robot toward the tip, we use tip location difference (called "tip error" henceforth) as a metric for comparing predictions to experiments, as has been done in many previous studies with active cannulas and other continuum robots. In our particular experiments, we also visually verified that tip error was the point of greatest deviation between model and experimental data, by plotting the two together for all experimental positions.

Using the nominal parameter values (those that were directly measured or appeared on data sheets – see [94] for further discussion of active cannula nominal

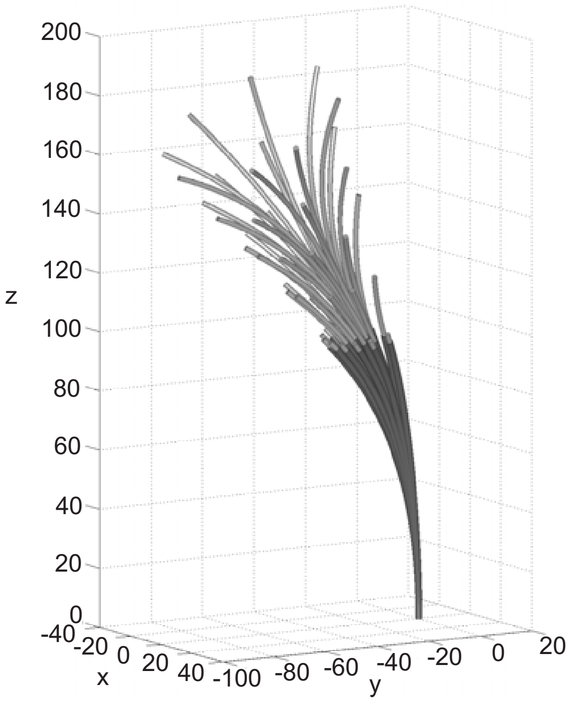

Figure 3.16: Illustration of the cannula in all 40 experimental configurations. One can span the entire workspace by rigidly rotating this collection about the z axis, which can be accomplished by rotating the base of each tube by the same amount, while keeping their angular differences the same. Thus, the above illustrates a sampling of all unique configuration space locations, from the model's point of view. For each configuration, backbone data was collected in the unloaded state and with a force applied to the tip of the cannula.

parameters, variances, and error propagation in model parameters) listed in Table 3.5, the mean tip error over all 80 experiments was 5.94 mm. Since actual values for the moduli of Nitinol tubes are highly uncertain (Young's modulus is listed as 41–75 GPa on data sheets from the manufacturer, NDC, Inc.), the values of each tube's bending and torsional stiffness were subsequently calibrated by finding the set of tube parameters which minimized the sum of the positional errors at three locations along the robot: the base ($s = 0$), the tip of the outer tube ($s = \ell_2$), and the tip of inner tube (the tip of the device, $s = \ell_1$). To reduce uncertainty in the registration of the robot base frame to the stereo camera frames, we included small changes to

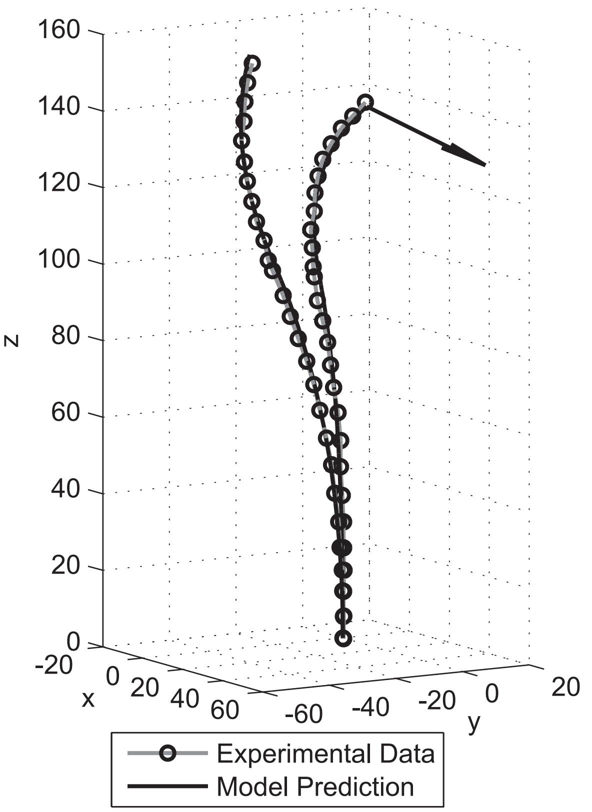

Figure 3.17: Comparison of model prediction and experimentally determined backbone points for the unloaded and loaded cases where actuators are set to $\beta_1 = -154.7$, $\beta_2 = -30.7$, $\alpha_1 = 135°$, and $\alpha_2 = 0°$. The direction of the 0.981 N applied force is shown by an arrow at the tip of the deformed model prediction. These examples are representative of our data set – their tip errors (approximately 3 mm) are near the 2.91 mm mean tip error over all 80 experiments.

the base frame position (translations δx, δy, δz) and to the orientation (XYZ Euler angle rotations $\delta\alpha$, $\delta\beta$, $\delta\gamma$) as additional parameters to be calibrated. Our calibration process is accomplished by solving an unconstrained nonlinear optimization problem for the parameter set

$P = \{E_1I_1, E_2I_2, J_1G_1, J_2G_2, \delta x, \delta y, \delta z, \delta\alpha, \delta\beta, \delta\gamma\}$:

$$P_{\text{calibrated}} = \underset{P}{\operatorname{argmin}}\left(\sum_{k=1}^{80} e_k(0) + e_k(\ell_2) + e_k(\ell_1)\right)$$

where $e_k(s) = \|\boldsymbol{p}_{model}(s) - \boldsymbol{p}_{data}(s)\|_k$ is the euclidean distance between the model backbone prediction and the data in experiment k. To implement this minimiza-

Table 3.8: Nominal and Calibrated Parameters

	Nominal Value	Calibrated Value
$E_1 I_1$ (Nm^2)	0.0204	0.0197
$J_1 G_1$ (Nm^2)	0.0157	0.0123
$E_2 I_2$ (Nm^2)	0.0458	0.0368
$J_2 G_2$ (Nm^2)	0.0352	0.0331
δx (mm)	0	-1.7
δy (mm)	0	-1.0
δz (mm)	0	0.3
$\delta\alpha$ (deg)	0	-0.06
$\delta\beta$ (deg)	0	0.67
$\delta\gamma$ (deg)	0	-0.58

tion, we used the Nelder-Meade simplex algorithm, as implemented by MATLAB's `fminsearch` function.

The parameters resulting from this model fitting procedure are shown in comparison to their nominal counterparts in Table 3.8. The base frame parameters showed only small changes during optimization, with XYZ Euler angles changing by $-0.06°$, $0.67°$, and $-0.58°$, while the frame origin translated 2.0 mm. Using these calibrated parameters, the mean error over all experiments was 2.91 mm as shown in Table 3.10.

Figure 3.17 shows the unloaded and loaded states of the cannula for actuator values of $\beta_1 = -154.7$, $\beta_2 = -30.7$, $\alpha_1 = 135°$, and $\alpha_2 = 0°$. Experimental data points are overlaid on the model prediction, and the model shown in the figure uses

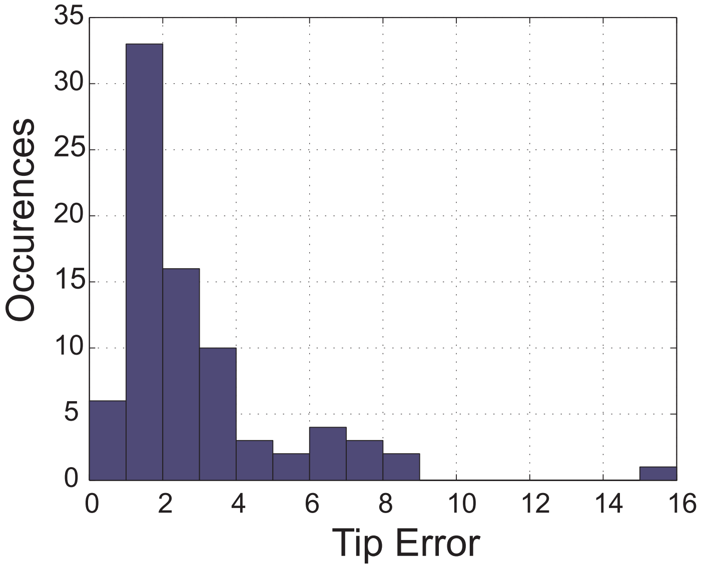

Figure 3.18: Histogram of tip error for all 80 experiments using fitted model parameters. 75% of the errors are below 3 mm, and 85% are below 4 mm

the calibrated parameters. The configuration shown is typical of all 80 experimental positions, in that the tip error in both cases is about 3 mm, while the mean for all experiments is 2.91 mm. The rest of the shape is also typical of the 80 experimental runs in that the experimental data lies very close to the model prediction along the entire backbone, and the applied forces were sufficient to cause large deflection in all cases.

3.5.3 Distributed Load Experiment

In order to demonstrate capability of the model of Section 3.4 to handle distributed loads, an experiment was conducted where a force distribution was applied along the length of the cannula. The actuator configuration was $\beta_1 = -122.7$ mm, $\beta_2 = -30.7$ mm, $\alpha_1 = \alpha_2 = 0°$. Note that the cannula's own weight is not sufficient to cause appreciable gravitational deflection, so we added additional weights along its

Table 3.9: Experimental Tip Error Statistics – Nominal Parameters

Tip Error Statistic (mm)	40 Unloaded Cases	40 Loaded Cases	All Cases
mean	3.76	7.82	5.79
min	0.60	2.42	0.60
max	10.59	25.53	25.53
std. dev.	2.85	4.13	4.08

Table 3.10: Experimental Tip Errors After Calibration

Tip Error Statistic (mm)	40 Unloaded Cases	40 Loaded Cases	All Cases
mean	2.89	2.92	2.91
min	0.62	0.91	0.62
max	8.49	15.20	15.20
std. dev.	2.19	2.52	2.34

length. As shown in Figure 3.19, we approximated a distributed load by placing a large number of nuts along the shaft of the cannula (on both the outer tube and the portion of the inner tube which extended out from the outer tube). The nuts were spaced evenly along the shaft and had a total mass of 56.96 grams. Stereo point correspondences were determined based on manually clicking backbone points between the nuts. The tip of the device was covered by the last nut, making it impossible to locate the tip in stereo images, so the tip was considered to be the last

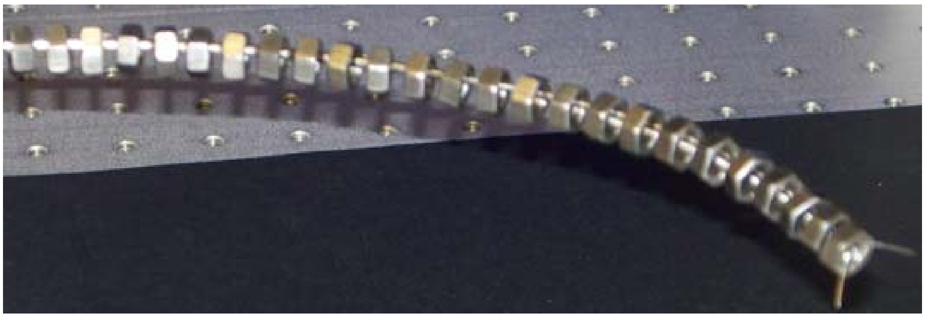

Figure 3.19: The active cannula under a distributed load represented by nuts equally spaced along its length.

visualizable section of the backbone, and the model arc length was reduced by one nut width. The model and experimental data for this loading condition are shown in Figure 3.20, along with the unloaded model for the same configuration. The tip error was 4.54 mm.

3.5.4 Statistical Analysis

Error statistics for both nominal and fitted parameter sets are given in Tables 3.9 and 3.10. The data set corresponds well to model predictions, with a mean tip error of 2.91 mm. An error histogram for all 80 cases shows that 75% of the errors were below 3 mm, and 85% were below 4 mm (Figure 3.18).

A statistical outlier with 15.20 mm of tip error occurred in the loaded state with $\beta_1 = -130.7$, $\beta_2 = -30.7$, $\alpha_1 = 270°$, $\alpha_2 = 0°$. The error in this case may have been increased by a procedural error (e.g. an incorrect α_1 value being recorded), or simply a worst-case compounding of unmodeled phenomena and measurement uncertainty. It is also worth noting that in this configuration the cannula was fully extended, and this error corresponds to only 7.68% of the arc length.

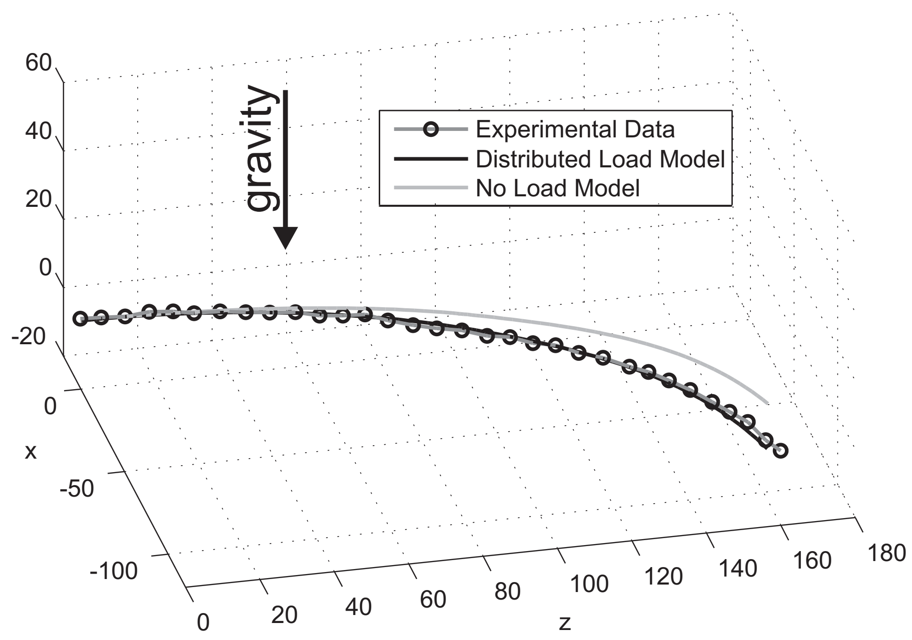

Figure 3.20: Comparison of loaded and unloaded model predictions with experimentally determined backbone points for a distributed load. The tip error is 4.54 mm.

We note that for long, slender continuum robots, tip error is highly dependent on the total arc length, since errors tend to increase from the base of the cannula to its tip, as mentioned previously. The total arc length of the active cannula in our experiments ranged from 105.9 mm to 197.9 mm over the experimental data set. Thus, an average tip error of 2.91 mm is approximately 1.5-3% of the arc length.

3.5.5 Error Sources

The unmodeled phenomena of transverse shear strain and elongation could potentially be accounted for by allowing $\Delta\xi(s)$ to include the first three components, $\Delta\boldsymbol{v}(s)$, but the kinematic constraints in this case become more complex, and shear effects are known to be negligible for long, thin beams. Additional torsion due to friction is likely a more significant effect, and could potentially be included in the model by additions or modifications of (3.55), which describes the axial torque along a tube. Depending on cannula design (intra-tube tolerances, precurvature functions, arc lengths, etc.), we believe that friction can become more pronounced than it was in our experimental prototype, and future model extensions accounting for it may be useful despite the minimal hysteresis observed in our experiments.

An unmodeled hardware detail that may be important is the fact that there is a small amount of clearance between the outside diameter of the inner tube and the inside diameter of the outer tube. This means that the tube tangents are not quite coincident where one exits the other, as the model assumes. In terms of design, this effect can be reduced by choosing tighter intra-tube tolerances, at the cost of increasing frictional effects. Alternatively, this effect could be modeled by modifying the continuity of position and orientation across transition points to include a small rotational and translational displacement where one tube exits another.

However, the fact that small tip errors were achieved without modeling any of the above effects indicates that they are largely negligible in our prototype. The model presented in this chapter effectively captures the main structural features of concentric tube continuum robots because it allows independent tube torsion during deformation. Whether it will be necessary to model any of these effects in the future will likely depend upon the design of the active cannula and the accuracy required by the application. Many clinical applications (e.g. needle biopsy or thermal ablation) can tolerate 3 mm tip errors. Other potential applications, such as retinal microsurgery, will require higher accuracy. In many cases, implementation of closed-loop control using this model is likely to significantly increase the operational accuracy and may render additional modeling detail unnecessary.

3.5.6 Conclusions

In this chapter we have presented an extension of the geometrically exact Cosserat rod theory to analyze a collection of concentric pre-curved tubes under a general set of distributed and point wrenches. We then tested this model in a set of experiments using an active cannula robot composed of two Nitinol tubes with general pre-set curved shapes, subject to both tip loads and distributed loads along the length of the device. With parameter fitting, the model achieved an average tip error of 2.91 mm across all 80 experimental positions, which span the model-unique configuration space.

Our modeling work in this chapter provides a theoretical foundation from which to understand active cannula shape under load, and from which to begin to explore many future applications. We expect that this model will be a valuable design tool in simulating proposed active cannula designs, enabling accurate compliance and kinematic analysis for cannulas intended to interact with tissue under environmental constraints. We also expect that it may facilitate use of the cannula's flexibility to sense and control contact forces. Intrinsic force sensing is desirable for thin continuum medical robots where inclusion of a force sensor could significantly affect device function (see [100]). Force information has the potential to enable tissue property estimation for locating lesions via palpation, or provide haptic feedback to the surgeon in a teleoperated system.

Chapter 4

Tendon-Actuated Continuum Robots

Tendons are a widely used actuation strategy for continuum robots, enabling forces and moments to be transmitted along the robot from base-mounted actuators. While most prior robots use tendons routed in straight paths along the robot, routing them through general curved paths within the robot offers potential advantages in reshaping the workspace and enabling a single section of the robot to achieve a wider variety of desired shapes. In this chapter, we provide a new model for the statics and dynamics of robots with general tendon routing paths, derived by coupling the classical Cosserat-rod and Cosserat-string models. This model also accounts for general external loading conditions, and encompasses traditional axially routed tendons as a special case. The advantage of using this coupled model for prior straight-tendon robots is that it accounts for the distributed wrenches that tendons apply along the robot. We show that these are necessary to consider when the robot is subjected to out-of-plane external loads. Experiments demonstrate the coupled model's ability to account for tendons routed through various curved paths. We show that the model matches experimental tip positions with an error of 1.7% of the robot length, in a set of experiments that include both straight and non-straight routing, with both point and distributed external loads.

4.1 Review of Classical Cosserat Rod Model

In this section we again provide a brief overview of the classical Cosserat rod model detailed in Chapter 2.

4.1.1 Rod Kinematics

In Cosserat-rod theory, a rod is characterized by its centerline curve in space $\boldsymbol{p}(s) \in \mathbb{R}^3$ and its material orientation, $R(s) \in \mathrm{SO}(3)$ which are functions of a reference parameter $s \in [0\ L]$. Thus a homogeneous transformation can be used to describe the entire rod:

$$g(s) = \begin{bmatrix} R(s) & \boldsymbol{p}(s) \\ 0 & 1 \end{bmatrix}.$$

Kinematic variables $\boldsymbol{v}(s)$ and $\boldsymbol{u}(s)$ represent the linear and angular rates of change of $g(s)$ with respect to s expressed in coordinates of the "body frame" $g(s)$. Thus, the evolution of $g(s)$ along s is defined by the following relationships;

$$\dot{R}(s) = R(s)\widehat{\boldsymbol{u}}(s), \quad \dot{\boldsymbol{p}}(s) = R(s)\boldsymbol{v}(s), \tag{4.1}$$

where, the dot denotes a derivative with respect to s, and the $^\wedge$ and $^\vee$ operators are as defined in Chapter 2, and [53].

We let the undeformed reference configuration of the rod be $g^*(s)$, where the z axis of $R^*(s)$ is chosen to be tangent to the curve $\boldsymbol{p}^*(s)$. One could use the Frenet-Serret or Bishop's convention to define the x and y axes of $R^*(s)$, or, if the rod has a cross section which is not radially symmetric, it is convenient to make the x and y

axes align with the principal axes. The reference kinematic variables $\boldsymbol{v}^*$ and $\boldsymbol{u}^*$ can then be obtained by

$$[\boldsymbol{v}^{*T} \;\; \boldsymbol{u}^{*T}]^T = \left(g^{*-1}(s)\dot{g}^*(s)\right)^\vee,$$

If the reference configuration happens to be a straight cylindrical rod with s as the arc length along it, then $\boldsymbol{v}^* = [0\ 0\ 1]^T$, and $\boldsymbol{u}^*(s) = [0\ 0\ 0]^T$.

4.1.2 Equilibrium Equations

Following [3], and our derivation in Chapter 2, one can write the equations of static equilibrium for an arbitrary section of rod as shown in Figure 4.1. The internal force and moment vectors (in global frame coordinates) are denoted by $\boldsymbol{n}$ and $\boldsymbol{m}$,the applied force distribution per unit of s is $\boldsymbol{f}$, and the applied moment distribution per unit of s is $\boldsymbol{l}$. Taking the derivative of the static equilibrium conditions with respect to s, one arrives at the classic forms of the equilibrium differential equations for a special Cosserat rod,

$$\dot{\boldsymbol{n}}(s) + \boldsymbol{f}(s) = \boldsymbol{0}, \tag{4.2}$$

$$\dot{\boldsymbol{m}}(s) + \dot{\boldsymbol{p}}(s) \times \boldsymbol{n}(s) + \boldsymbol{l}(s) = \boldsymbol{0}. \tag{4.3}$$

4.1.3 Constitutive Laws

One can use linear constitutive laws to map the kinematic strain variables to the internal forces and moments. Assuming that the x and y axes of g^* are aligned with

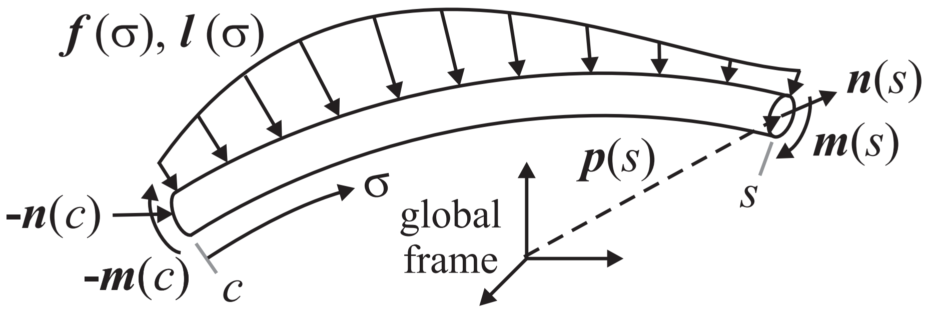

Figure 4.1: Arbitrary section of rod from c to s subject to distributed forces and moments. The internal forces $\boldsymbol{n}$ and moments $\boldsymbol{m}$ are also shown.

the principal axes of the cross section, we have

$$\begin{aligned}\boldsymbol{n}(s) =&R(s)K_{SE}(s)\left(\boldsymbol{v}(s)-\boldsymbol{v}^{*}(s)\right),\\ \boldsymbol{m}(s) =&R(s)K_{BT}(s)\left(\boldsymbol{u}(s)-\boldsymbol{u}^{*}(s)\right),\end{aligned}\tag{4.4}$$

where

$$\begin{aligned}&K_{SE}(s) =\mathrm{diag}\left(GA(s),GA(s),EA(s)\right), \quad \text{and}\\ &K_{BT}(s) =\mathrm{diag}\left(EI_{xx}(s),EI_{yy}(s),EI_{zz}(s)\right).\end{aligned}$$

K_{SE} is the stiffness matrix for shear and extension, and K_{BT} is the stiffness matrix for bending and torsion, where $A(s)$ is the area of the cross section, $E(s)$ is Young's modulus, $G(s)$ is the shear modulus, and $I_{xx}(s)$ and $I_{yy}(s)$ are the second moments of area of the tube cross section about the principal axes. (Note that $I_{zz}(s) = I_{xx}(s) + I_{yy}(s)$ is the polar moment of inertia of the cross section about the z axis pointing normal to the section and originating at its centroid.) We use these linear relationships here because they are notationally convenient and accurate for many continuum robots, but the Cosserat rod approach does not require it.

4.1.4 Explicit Model Equations

We can now write (4.2) and (4.3) in terms of the kinematic variables using (4.4), their derivatives, and (4.1). Assuming that the stiffness matrices are constant with respect to s, this leads to a the full set of differential equations shown below:

$$\begin{aligned}
\dot{\boldsymbol{p}} &= R\boldsymbol{v} \\
\dot{R} &= R\widehat{\boldsymbol{u}} \\
\dot{\boldsymbol{v}} &= \dot{\boldsymbol{v}}^* - K_{SE}^{-1}\Big(\widehat{\boldsymbol{u}}K_{SE}\left(\boldsymbol{v}-\boldsymbol{v}^*\right) + R^T\boldsymbol{f}\Big) \\
\dot{\boldsymbol{u}} &= \dot{\boldsymbol{u}}^* - K_{BT}^{-1}\Big(\widehat{\boldsymbol{u}}K_{BT}\left(\boldsymbol{u}-\boldsymbol{u}^*\right) + \widehat{\boldsymbol{v}}K_{SE}\left(\boldsymbol{v}-\boldsymbol{v}^*\right) + R^T\boldsymbol{l}\Big)
\end{aligned} \tag{4.5}$$

Alternatively, an equivalent system can be obtained using $\boldsymbol{m}$ and $\boldsymbol{n}$ as state variables rather than $\boldsymbol{v}$ and $\boldsymbol{u}$:

$$\begin{aligned}
\dot{\boldsymbol{p}} &= R\boldsymbol{v}, \qquad & \boldsymbol{v} &= K_{SE}^{-1}R^T\boldsymbol{n} + \boldsymbol{v}^* \\
\dot{R} &= R\widehat{\boldsymbol{u}}, \qquad & \boldsymbol{u} &= K_{BT}^{-1}R^T\boldsymbol{m} + \boldsymbol{u}^* \\
\dot{\boldsymbol{n}} &= -\boldsymbol{f} \\
\dot{\boldsymbol{m}} &= -\dot{\boldsymbol{p}} \times \boldsymbol{n} - \boldsymbol{l}
\end{aligned} \tag{4.6}$$

Boundary conditions for a rod which is clamped at $s = 0$ and subject to an applied force $\boldsymbol{F}_\ell$ and moment $\boldsymbol{L}_\ell$ at $s = \ell$ would be $R(0) = R_0$, $\boldsymbol{p}(0) = \boldsymbol{p}_0$, $\boldsymbol{m}(\ell) = \boldsymbol{L}_\ell$, and $\boldsymbol{n}(\ell) = \boldsymbol{F}_\ell$.

4.2 Coupled Cosserat Rod and Tendon Model

Having reviewed the classic Cosserat-rod model, we now derive a new model for tendon driven continuum manipulators. We use the Cosserat model of Section 4.1 to describe the elastic backbone, and we use the classic Cosserat model for extensible strings to describe the tendons. We will couple the string and rod models together by deriving the distributed loads that the tendons apply to the backbone in terms of the rod's kinematic variables, and then incorporating these loads into the rod model.

4.2.1 Assumptions

We employ two standard assumptions in our derivation. First, we assume frictionless interaction between the tendons and the channel through which they travel. This implies that the tension is constant along the length of the tendon. Frictional forces are expected to increase as the curvature of the robot increases due to larger normal forces, but the assumption of zero friction is valid if low friction materials are used, which is the case for our experimental prototype. Second, the locations of the tendons within the cross section of the robot are assumed not to change during the deformation. This assumption is valid for designs which use embedded sleeves or channels with tight tolerances, as well as designs which use closely spaced standoff disks.

4.2.2 Tendon Kinematics

We separate the terms $\boldsymbol{f}$ and $\boldsymbol{l}$ in (4.5) into truly external distributed loads, $\boldsymbol{f}_e$ and $\boldsymbol{l}_e$, and distributed loads due to tendon tension, $\boldsymbol{f}_t$ and $\boldsymbol{l}_t$.

$$\begin{aligned} \boldsymbol{f} &= \boldsymbol{f}_e + \boldsymbol{f}_t \\ \boldsymbol{l} &= \boldsymbol{l}_e + \boldsymbol{l}_t. \end{aligned} \tag{4.7}$$

In order to derive $\boldsymbol{f}_t$ and $\boldsymbol{l}_t$, we start by defining the path in which the tendon is routed along the robot length. Note that this path can be defined by channels or

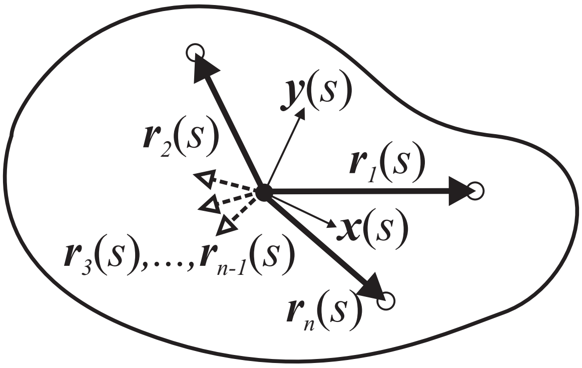

Figure 4.2: General cross section of the continuum robot material or support disk, showing tendon locations.

tubes within a homogeneous elastic structure, or support disks on an elastic backbone – both of which afford considerable flexibility in choosing tendon routing. In our experimental prototype, we drill many holes around the periphery of each support disk, allowing easy reconfiguration of tendon path as desired.

A convenient way to mathematically describe the tendon routing path is to define the tendon location within the robot cross section as a function of the reference parameter s. Thus, we define the routing path of the i^{th} tendon by two functions $x_i(s)$ and $y_i(s)$ that give the body-frame coordinates of the tendon as it crosses the $x-y$ plane of the attached backbone frame at s. As shown in Figure 4.2, a vector from the origin of the attached frame to the tendon location is then given in attached frame coordinates by

$$\boldsymbol{r}_i(s) = \begin{bmatrix} x_i(s) \; y_i(s) \; 0 \end{bmatrix}^T . \tag{4.8}$$

The parametric space curve defining the tendon path in the global frame when the robot is in its undeformed reference configuration is then given by

$$\boldsymbol{p}_i^*(s) = R^*(s)\boldsymbol{r}_i(s) + \boldsymbol{p}^*(s).$$

Similarly, when the robot is deformed due to tendon tension or external loads, the new tendon path in the global frame will be

$$\boldsymbol{p}_i(s) = R(s)\boldsymbol{r}_i(s) + \boldsymbol{p}(s). \tag{4.9}$$

4.2.3 Distributed Forces on Tendons

The governing differential equations for an extensible string can be derived by taking the derivative of the static equilibrium conditions for a finite section [3]. This results in the same equation for the internal force derivative as in (4.2).

$$\dot{\boldsymbol{n}}_i(s) + \boldsymbol{f}_i(s) = \boldsymbol{0}, \tag{4.10}$$

where $\boldsymbol{f}_i(s)$ is the distributed force applied to the i^{th} tendon per unit of s, and $\boldsymbol{n}_i(s)$ is the internal force in the tendon. In contrast to a Cosserat rod, an ideal string has the defining constitutive property of being perfectly flexible, meaning it cannot support internal moments or shear forces, but only tension [3] which we denote by τ_i. This requires that the internal force be always tangent to the curve $\boldsymbol{p}_i(s)$. Thus, we write

$$\boldsymbol{n}_i(s) = \tau_i \frac{\dot{\boldsymbol{p}}_i(s)}{\|\dot{\boldsymbol{p}}_i(s)\|}. \tag{4.11}$$

If friction were present, τ_i would vary with s, but under the frictionless assumption, it is constant along the length of the tendon. Using (4.10) and (4.11) one can derive an expression for the distributed force on the tendon as follows.

Beginning with (4.11),

$$\boldsymbol{n}_i = \tau_i \frac{\dot{\boldsymbol{p}}_i}{\|\dot{\boldsymbol{p}}_i\|},$$

we re-arrange and differentiate to obtain

$$\dot{\boldsymbol{p}}_i = \frac{1}{\tau_i}\left\|\dot{\boldsymbol{p}}_i\right\|\boldsymbol{n}_i, \qquad \ddot{\boldsymbol{p}}_i = \frac{1}{\tau_i}\left(\frac{d}{ds}\left(\left\|\dot{\boldsymbol{p}}_i\right\|\right)\boldsymbol{n}_i + \left\|\dot{\boldsymbol{p}}_i\right\|\dot{\boldsymbol{n}}_i\right).$$

Noting that $\boldsymbol{n}_i \times \boldsymbol{n}_i = 0$, one can take a cross product of the two results above to find,

$$\ddot{\boldsymbol{p}}_i \times \dot{\boldsymbol{p}}_i = \frac{\left\|\dot{\boldsymbol{p}}_i\right\|^2}{\tau_i^2}\left(\dot{\boldsymbol{n}}_i \times \boldsymbol{n}_i\right)$$

and so

$$\dot{\boldsymbol{p}}_i \times \left(\ddot{\boldsymbol{p}}_i \times \dot{\boldsymbol{p}}_i\right) = \frac{\left\|\dot{\boldsymbol{p}}_i\right\|^3}{\tau_i^3}\left(\boldsymbol{n}_i \times \left(\dot{\boldsymbol{n}}_i \times \boldsymbol{n}_i\right)\right).$$

Applying the vector triple product identity, $\boldsymbol{a} \times (\boldsymbol{b} \times \boldsymbol{c}) = \boldsymbol{b}\,(\boldsymbol{a} \cdot \boldsymbol{c}) - \boldsymbol{c}\,(\boldsymbol{a} \cdot \boldsymbol{b})$, we can expand the right-hand side of this equation. Since τ_i (the magnitude of $\boldsymbol{n}_i$) is constant with respect to s, then $\boldsymbol{n}_i \cdot \dot{\boldsymbol{n}}_i = \boldsymbol{0}$, and this results in

$$\boldsymbol{f}_i = -\dot{\boldsymbol{n}}_i = -\tau_i \frac{\dot{\boldsymbol{p}}_i \times \left(\ddot{\boldsymbol{p}}_i \times \dot{\boldsymbol{p}}_i\right)}{\left\|\dot{\boldsymbol{p}}_i\right\|^3}.$$

Using the fact that $\boldsymbol{a} \times \boldsymbol{b} = -\boldsymbol{b} \times \boldsymbol{a}$, and writing the cross products in skew-symmetric matrix notation ($\boldsymbol{a} \times \boldsymbol{b} = \widehat{\boldsymbol{a}}\boldsymbol{b}$), we arrive at

$$\boldsymbol{f}_i = \tau_i \frac{\dot{\boldsymbol{p}}_i \times \left(\dot{\boldsymbol{p}}_i \times \ddot{\boldsymbol{p}}_i\right)}{\left\|\dot{\boldsymbol{p}}_i\right\|^3} = \tau_i \frac{\widehat{\dot{\boldsymbol{p}}}_i^2}{\left\|\dot{\boldsymbol{p}}_i\right\|^3}\ddot{\boldsymbol{p}}_i. \tag{4.12}$$

4.2.4 Tendon Loads on Backbone

We can now write the collective distributed loads $\boldsymbol{f}_t$ and $\boldsymbol{l}_t$ that the tendons apply to the backbone, in terms of the individual forces on the tendons and their locations in the backbone cross-section.

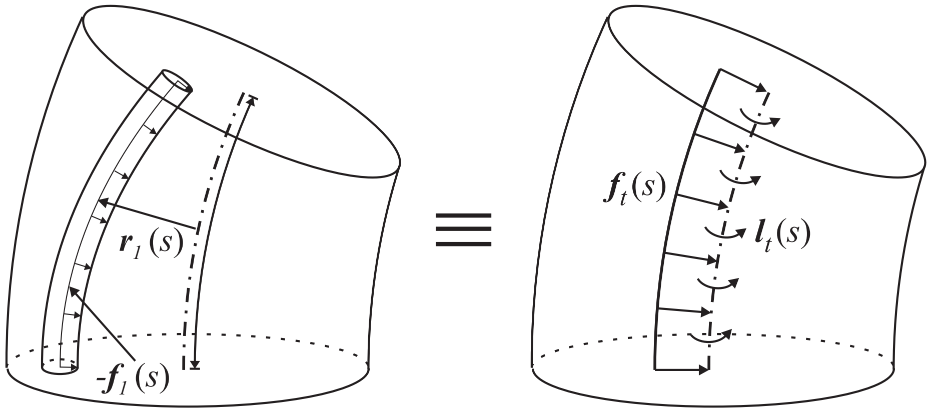

Figure 4.3: A small section of rod showing how the force distribution that the tendon applies to its surrounding medium is statically equivalent to a combination of force and moment distributions on the backbone itself.

The total distributed force is equal and opposite to the sum of the individual force distributions on the tendons (4.12), namely,

$$\boldsymbol{f}_t = -\sum_{i=1}^{n} \boldsymbol{f}_i.$$

The distributed moment at the backbone centroid is the sum of the cross products of each moment arm with each force. Thus,

$$\boldsymbol{l}_t = -\sum_{i=1}^{n} (\boldsymbol{p}_i - \boldsymbol{p}) \times \boldsymbol{f}_i = -\sum_{i=1}^{n} (Rr_i)^{\wedge} \boldsymbol{f}_i.$$

Substituting (4.12), yields

$$\begin{aligned} \boldsymbol{f}_t &= -\sum_{i=1}^{n} \tau_i \frac{\widehat{\dot{\boldsymbol{p}}_i}^2}{\|\dot{\boldsymbol{p}}_i\|^3} \ddot{\boldsymbol{p}}_i, \\ \boldsymbol{l}_t &= -\sum_{i=1}^{n} \tau_i \, (R\boldsymbol{r}_i)^{\wedge} \frac{\widehat{\dot{\boldsymbol{p}}_i}^2}{\|\dot{\boldsymbol{p}}_i\|^3} \ddot{\boldsymbol{p}}_i. \end{aligned} \tag{4.13}$$

We now express these total force and moment distributions in terms of the kinematic variables $\boldsymbol{u}$, $\boldsymbol{v}$, R and $\boldsymbol{p}$ so that we may substitute them into equations (4.7) and (4.5). To do this, we expand $\dot{\boldsymbol{p}}_i$ and $\ddot{\boldsymbol{p}}_i$. Differentiating (4.9) twice yields,

$$\begin{aligned}\dot{\boldsymbol{p}}_i =& R\left(\widehat{\boldsymbol{u}}\boldsymbol{r}_i + \dot{\boldsymbol{r}}_i + \boldsymbol{v}\right),\\ \ddot{\boldsymbol{p}}_i =& R\left(\widehat{\boldsymbol{u}}\left(\widehat{\boldsymbol{u}}\boldsymbol{r}_i + \dot{\boldsymbol{r}}_i + \boldsymbol{v}\right) + \widehat{\dot{\boldsymbol{u}}}\boldsymbol{r}_i + \widehat{\boldsymbol{u}}\dot{\boldsymbol{r}}_i + \ddot{\boldsymbol{r}}_i + \dot{\boldsymbol{v}}\right).\end{aligned} \tag{4.14}$$

We here note that $\ddot{\boldsymbol{p}}$ is a function of $\dot{\boldsymbol{u}}$ and $\dot{\boldsymbol{v}}$. Therefore, if we substitute these results into (4.13), and substitute (4.13) into the rod model (4.5) via (4.7), we obtain an implicitly defined set of differential equations. Fortunately, the resulting equations are linear in $\dot{\boldsymbol{u}}$ and $\dot{\boldsymbol{v}}$, and it is therefore possible to manipulate them into an explicit form. Rewriting them in this way (such that they are amenable to standard numerical methods) is the topic of the following subsection.

4.2.5 Explicit Decoupled Model Equations

Our coupled rod and tendon model is given in implicit form by (4.5), (4.7), (4.13), and (4.14). In this subsection, we algebraically manipulate these implicit equations into explicit, first-order, state-vector form. To express the result concisely, we have defined some intermediate matrix and vector quantities, starting with (4.14) expressed in body-frame coordinates, i.e.

$$\begin{aligned}\dot{\boldsymbol{p}}_i^b &= \widehat{\boldsymbol{u}}\boldsymbol{r}_i + \dot{\boldsymbol{r}}_i + \boldsymbol{v},\\ \ddot{\boldsymbol{p}}_i^b &= \widehat{\boldsymbol{u}}\dot{\boldsymbol{p}}_i^b + \widehat{\dot{\boldsymbol{u}}}\boldsymbol{r}_i + \widehat{\boldsymbol{u}}\dot{\boldsymbol{r}}_i + \ddot{\boldsymbol{r}}_i + \dot{\boldsymbol{v}}.\end{aligned}$$

We define vectors $\boldsymbol{a}_i$, $\boldsymbol{a}$, $\boldsymbol{b}_i$, and $\boldsymbol{b}$, as well as matrices A_i, A, B_i, B, G, and H as follows:

$$\begin{aligned} A_i =& -\tau_i \frac{\left(\widehat{\dot{\boldsymbol{p}}_i^b}\right)^2}{\left\|\dot{\boldsymbol{p}}_i^b\right\|^3}, & B_i &= \widehat{\boldsymbol{r}}_i A_i, \\ A =& \sum_{i=1}^{n} A_i, & B &= \sum_{i=1}^{n} B_i, \\ G =& -\sum_{i=1}^{n} A_i \widehat{\boldsymbol{r}}_i, & H &= -\sum_{i=1}^{n} B_i \widehat{\boldsymbol{r}}_i \\ \boldsymbol{a}_i =& A_i \left(\widehat{\boldsymbol{u}}\dot{\boldsymbol{p}}_i^b + \widehat{\boldsymbol{u}}\dot{\boldsymbol{r}}_i + \ddot{\boldsymbol{r}}_i\right), & \boldsymbol{b}_i &= \widehat{\boldsymbol{r}}_i \boldsymbol{a}_i, \\ \boldsymbol{a} =& \sum_{i=1}^{n} \boldsymbol{a}_i, & \boldsymbol{b} &= \sum_{i=1}^{n} \boldsymbol{b}_i. \end{aligned}$$

We then find that $\boldsymbol{f}_t$ and $\boldsymbol{l}_t$ can be expressed as

$$\begin{aligned} \boldsymbol{f}_t =& R\left(\boldsymbol{a} + A\dot{\boldsymbol{v}} + G\dot{\boldsymbol{u}}\right), \\ \boldsymbol{l}_t =& R\left(\boldsymbol{b} + B\dot{\boldsymbol{v}} + H\dot{\boldsymbol{u}}\right). \end{aligned} \tag{4.15}$$

Substituting tendon load expressions into the last two equations of (4.5) and rearranging them, we have

$$\begin{aligned} \left(K_{SE} + A\right)\dot{\boldsymbol{v}} + G\dot{\boldsymbol{u}} &= \boldsymbol{d} \\ B\dot{\boldsymbol{v}} + \left(K_{BT} + H\right)\dot{\boldsymbol{u}} &= \boldsymbol{c} \end{aligned}$$

where the vectors $\boldsymbol{c}$ and $\boldsymbol{d}$ are functions of the state variables as shown below.

$$\begin{aligned} \boldsymbol{c} =& K_{BT}\dot{\boldsymbol{u}}^* - \widehat{\boldsymbol{u}}K_{BT}\left(\boldsymbol{u} - \boldsymbol{u}^*\right) - \widehat{\boldsymbol{v}}K_{SE}\left(\boldsymbol{v} - \boldsymbol{v}^*\right) - R^T\boldsymbol{l}_e - \boldsymbol{b} \\ \boldsymbol{d} =& K_{SE}\dot{\boldsymbol{v}}^* - \widehat{\boldsymbol{u}}K_{SE}\left(\boldsymbol{v} - \boldsymbol{v}^*\right) - R^T\boldsymbol{f}_e - \boldsymbol{a}. \end{aligned}$$

We can now easily write the governing equations as

$$\begin{aligned}
&\dot{\boldsymbol{p}} = R\boldsymbol{v} \\
&\dot{R} = R\widehat{\boldsymbol{u}} \\
&\begin{bmatrix} \dot{\boldsymbol{v}} \\ \\ \dot{\boldsymbol{u}} \end{bmatrix} = \begin{bmatrix} K_{SE} + A & G \\ \\ B & K_{BT} + H \end{bmatrix}^{-1} \begin{bmatrix} \boldsymbol{d} \\ \\ \boldsymbol{c} \end{bmatrix}.
\end{aligned} \tag{4.16}$$

Noting that the quantities on the right hand side of (4.16) are merely functions of the state variables and system inputs ($\boldsymbol{u}$, $\boldsymbol{v}$, R, $\tau_1, ..., \tau_n$, $\boldsymbol{f}_e$ and $\boldsymbol{l}_e$), we have arrived at a system of differential equations in standard explicit form, describing the shape of a continuum robot with any number of generally routed tendons and with general external loads applied.

This system can be solved by any standard numerical integration routine for systems of the form $\dot{\boldsymbol{y}} = \boldsymbol{f}(s, \boldsymbol{y})$. The required matrix inverse may be calculated (either numerically or by obtaining a closed form inverse) at every integration step, or one could alternatively rewrite the equations as a system with a state dependent mass matrix on the left hand side and use any standard numerical method for solving $M(y, s)\dot{\boldsymbol{y}} = \boldsymbol{f}(s, \boldsymbol{y})$. For purposes of the simulations and experiments in this chapter, we simply numerically invert.

4.2.6 Simplified No-Shear Model

It is often the case that the effect of shear and extension is negligible when computing the deformed shape of a rod. Below we give decoupled model equations that result from assuming that there is zero shear and extension. Specifically we let $\boldsymbol{v} = \boldsymbol{v}^* =$

$[0 \;\; 0 \;\; 1]^T$. This results in the following decoupled model equations:

$$\begin{aligned}\dot{\boldsymbol{p}} &= R\boldsymbol{v} \\ \dot{R} &= R\widehat{\boldsymbol{u}} \\ \dot{\boldsymbol{u}} &= (H + K_{BT})^{-1}\Big(K_{BT}\dot{\boldsymbol{u}}^* - \widehat{\boldsymbol{u}}K_{BT}(\boldsymbol{u} - \boldsymbol{u}^*) - \widehat{\boldsymbol{v}}R^T\boldsymbol{n} - R^T\boldsymbol{l}_e - \boldsymbol{b}\Big) \\ \dot{\boldsymbol{n}} &= -R(\boldsymbol{a} + G\dot{\boldsymbol{u}}) - \boldsymbol{f}_e\end{aligned} \tag{4.17}$$

4.2.7 Boundary Conditions

When tendon i terminates at $s = \ell_i$ along the length of the robot, it applies a point force to its attachment point equal and opposite to the internal force in the tendon given by (4.11). Thus, the point force vector is given by

$$\boldsymbol{F}_i = -\boldsymbol{n}_i(\ell_i) = -\tau_i \frac{\dot{\boldsymbol{p}}_i(\ell_i)}{\|\dot{\boldsymbol{p}}_i(\ell_i)\|} \tag{4.18}$$

With a moment arm of $\boldsymbol{p}_i(\ell_i) - \boldsymbol{p}(\ell_i)$, this force creates a point moment $\boldsymbol{L}_i$ at the backbone centroid of,

$$\boldsymbol{L}_i = -\tau_i \left(R(\ell_i)\boldsymbol{r}_i(\ell_i)\right)^\wedge \frac{\dot{\boldsymbol{p}}_i(\ell_i)}{\|\dot{\boldsymbol{p}}_i(\ell_i)\|}. \tag{4.19}$$

If at some location $s = \sigma$, point loads $\boldsymbol{F}(\sigma)$ and $\boldsymbol{L}(\sigma)$ (resulting from tendon terminations or external loads) are applied to the backbone, the internal force and moment change across the boundary $s = \sigma$ by,

$$\begin{aligned}\boldsymbol{n}(\sigma^-) &= \boldsymbol{n}(\sigma^+) + \boldsymbol{F}(\sigma), \\ \boldsymbol{m}(\sigma^-) &= \boldsymbol{m}(\sigma^+) + \boldsymbol{L}(\sigma).\end{aligned} \tag{4.20}$$

where σ^- and σ^+ denote locations just before and just after $s = \sigma$. Any combination of external point loads and tendon termination loads can be accommodated in this way.

4.2.8 Point Moment Model

In prior tendon robot models, tendon actuation has often been modeled by simply applying the pure point moment in (4.19) to an elastic backbone model at the location where each tendon is attached, without considering the point force at the attachment point and the distributed tendon loads along the length (see Figure 4.4). This approach is convenient because it allows one to use the classical Cosserat rod equations (2.15) by simply applying boundary conditions that take into account the tendon termination moments.

In [32], Gravagne justified this approximation for planar robots by showing that the effects of the point force and the distributed loads effectively "cancel" each other, leaving only the point moment. Thus, as shown in Figure 1.3 this approach yields almost exactly the same final shape as the full coupled model when the robot deformation occurs in a plane.

However, as shown in Figure 1.3, the two approaches diverge as the robot shape becomes increasingly non-planar due to a transverse load at the tip. In Section 4.4, we investigate the accuracy of both approaches through a set of experiments on a prototype robot.

4.3 Dynamic Model

Based on the coupled rod and tendon model presented above for static continuum robot deformations, we now derive a model for the dynamics of a continuum robot

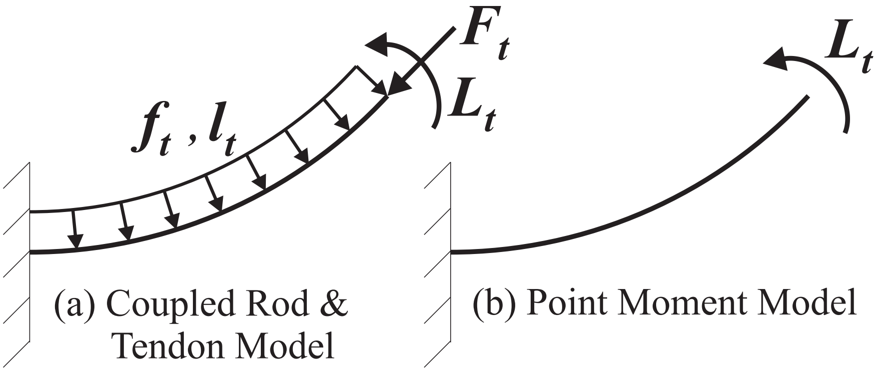

Figure 4.4: (a) The coupled Cosserat rod and tendon approach includes all of the tendon loads. These loads are themselves functions of the robot shape, so the robot is treated as a coupled system. (b) The point moment approach only includes the attachment moment. For planar deformations the two approaches predict a similar robot shapes, but our experimental results show that for out-of-plane loading, the coupled approach is more accurate.

with general tendon routing. Such a model will be useful for analyzing the characteristics of specific designs as well as the development of control algorithms similar to those derived for planar robots with straight tendons [33]. As we will show, adding the necessary dynamic terms and compatibility equations results in a hyperbolic system of partial differential equations, which can be expressed in the standard form

$$\boldsymbol{y}_t = f(s, t, \boldsymbol{y}, \boldsymbol{y}_s), \tag{4.21}$$

where a subscript s or t is used in this section to denote partial derivatives with respect to the reference parameter s and time t respectively.

We introduce two new vector variables, $\boldsymbol{q}$ and $\boldsymbol{\omega}$, which are the body frame linear and angular velocity of the rod at s. These are analogous to $\boldsymbol{u}$ and $\boldsymbol{v}$ respectively, but are defined with respect to time instead of arc length. Thus,

$$\boldsymbol{p}_t = R\boldsymbol{q} \qquad R_t = R\widehat{\boldsymbol{\omega}}. \tag{4.22}$$

Recalling from (4.5) that

$$\boldsymbol{p}_s = R\boldsymbol{v} \qquad R_s = R\widehat{\boldsymbol{u}}, \tag{4.23}$$

and using the fact that $\boldsymbol{p}_{st} = \boldsymbol{p}_{ts}$ and $R_{st} = R_{ts}$, we can derive the following compatibility equations,

$$\boldsymbol{u}_t = \boldsymbol{\omega}_s + \widehat{\boldsymbol{u}}\boldsymbol{\omega} \qquad \boldsymbol{v}_t = \boldsymbol{q}_s + \widehat{\boldsymbol{u}}\boldsymbol{q} - \widehat{\boldsymbol{\omega}}\boldsymbol{v}, \tag{4.24}$$

Equations (4.2) and (4.3) describe the static equilibrium of the rod. To describe dynamics, we can add the time derivatives of the linear and angular momentum per unit length in place of the zero on the right hand side, such that they become,

$$\dot{\boldsymbol{n}} + \boldsymbol{f} = \rho A \boldsymbol{p}_{tt}, \tag{4.25}$$

$$\dot{\boldsymbol{m}} + \dot{\boldsymbol{p}} \times \boldsymbol{n} + \boldsymbol{l} = \partial_t \left(R\rho J \boldsymbol{\omega} \right), \tag{4.26}$$

where ρ is the mass density of the rod, A is the cross sectional area of the backbone, and J is is the matrix of second area moments of the cross section. Expanding these and applying (4.24) one can obtain a complete system in the form of (4.21),

$$\begin{aligned}
\boldsymbol{p}_t =& R\boldsymbol{q} \\
R_t =& R\widehat{\boldsymbol{\omega}} \\
\boldsymbol{v}_t =& \boldsymbol{q}_s + \widehat{\boldsymbol{u}}\boldsymbol{q} - \widehat{\boldsymbol{\omega}}\boldsymbol{v} \\
\boldsymbol{u}_t =& \boldsymbol{\omega}_s + \widehat{\boldsymbol{u}}\boldsymbol{\omega} \\
\boldsymbol{q}_t =& \frac{1}{\rho A}\Big(K_{SE}\left(\boldsymbol{v}_s - \boldsymbol{v}_s^*\right) + \widehat{\boldsymbol{u}} K_{SE}\left(\boldsymbol{v} - \boldsymbol{v}^*\right) \\
& \qquad + R^T\left(\boldsymbol{f}_e + \boldsymbol{f}_t\right) - \rho A \widehat{\boldsymbol{\omega}}\boldsymbol{q} \Big) \\
\boldsymbol{\omega}_t =& (\rho J)^{-1}\Big(K_{BT}\left(\boldsymbol{u}_s - \boldsymbol{u}_s^*\right) + \widehat{\boldsymbol{u}} K_{BT}\left(\boldsymbol{u} - \boldsymbol{u}^*\right) \\
& \qquad + \widehat{\boldsymbol{v}} K_{SE}\left(\boldsymbol{v} - \boldsymbol{v}^*\right) + R^T\left(\boldsymbol{l}_e + \boldsymbol{l}_t\right) - \widehat{\boldsymbol{\omega}}\rho J \boldsymbol{\omega} \Big)
\end{aligned} \tag{4.27}$$

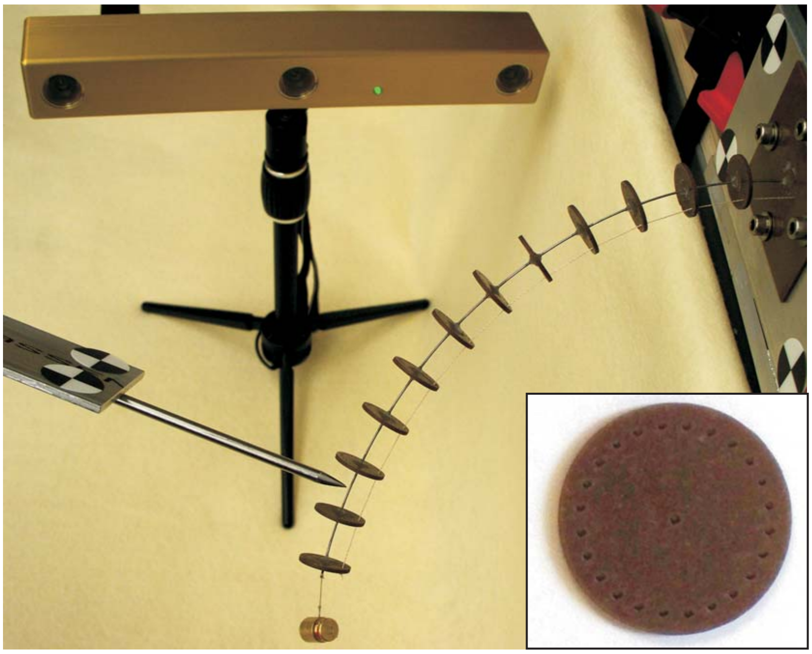

Figure 4.5: In each experiment, a set of 3D data points along the backbone was taken with an optically tracked stylus. (Inset) A standoff disk with a central hole for the backbone rod and outer holes through which tendons may be routed. Twelve copies of this disk were attached along the backbone as shown in the larger figure.

where $\boldsymbol{f}_t$ and $\boldsymbol{l}_t$ can be computed using (4.15). Typically, conditions at $t = 0$ are given for all variables along the length of the robot, and the boundary conditions of Subsection 4.2.7 apply for all time.

An active research field in mechanics and computer graphics simulation is to numerically evaluate models of dynamic rods that are physically accurate, and yet capable of being simulated in real-time (see e.g. [10]). Future research for our coupled rod and string model may address computational efficiency, internal damping, and real-time dynamic control.

4.4 Experimental Validation

We now describe several different experiments conducted using a continuum robot prototype with a variety of tendon paths and external loading conditions applied.

4.4.1 Prototype Construction

Our prototype robot is shown in Figure 4.5. The central backbone is a spring steel rod (ASTM A228) of length $\ell = 242$ mm and diameter $d = 0.8$ mm with 12 stand-off disks, 20 mm in diameter, spaced 20 mm apart along its length. The disks were laser cut from a 1.57 mm thick PTFE filled Delrin plastic to minimize friction with the tendons. As shown in the inset of Figure 4.5, 24 small pass-through holes were laser cut in a circular pattern at a radius of 8 mm from the center of each disk. The backbone rod was passed through the center holes of the disks and each was fixed to it using Loctite 401. For tendons, we used 0.36 mm PTFE coated fiberglass thread. Each tendon was run through various pass-through holes along the robot and knotted at the end, after passing through the final support disk. We note that in [49], the optimal ratio of tendon support spacing to offset distance from the backbone was found to be 0.4, and our prototype was designed to exactly match this ratio.

The tendon routing paths can be reconfigured on this robot by “re-threading” the tendons through a different set of holes in the various support disks. The robot’s self-weight distribution was measured to be 0.47 N/m, which is enough to cause significant deformation, producing 44 mm of downward deflection at the tip (18% of the total

Table 4.1: Tendon Routing Paths used in Experiments

Tendon (i)	1	2	3	4	5	6
$x_i(s)$ (mm)	8	0	-8	0	$8\cos(2\pi s/\ell)$	refer to (4.28)
$y_i(s)$ (mm)	0	8	0	-8	$8\sin(2\pi s/\ell)$	refer to (4.28)

arc length) for zero tendon tension. This weight was incorporated into all model calculations as a distributed force.

4.4.2 Experimental Procedure

In each of the following experiments, we applied known tensions to tendons behind the base of the robot by passing the tendons over approximately frictionless pulleys and attaching them to hanging calibration weights. In those cases with applied point loads, we also hung weights from the tip of the robot.

In each experiment, a set of 3D backbone points was collected by manually touching the backbone with the tip of an optically tracked stylus as shown in Figure 4.5. We used a MicronTracker 2 H3-60 (Claron Technology, Inc.) to track the stylus, which has a specified fiducial measurement accuracy of 0.20 mm.

4.4.3 Calibration

The base frame position of the robot can be determined accurately using the optically tracked stylus. The angular orientation of the robot backbone as it leaves the base support plate is more challenging to measure. (Note that the backbone cannot be

Table 4.2: Experimental Tensions and Tip Loads

Experiments with Tendons 1 - 4 (Straight)							
Tension (N)	0	0.98	1.96	2.94	2.94	2.94	4.91
Tip Load (N)	0	0	0	0	0.098	0.196	0

Experiments with Tendon 5 (Helical)							
Tension (N)	0.98	1.96	2.94	4.91	4.91	4.91	6.87
Tip Load (N)	0	0	0	0	0.098	0.196	0

Experiments with Tendon 6 (Polynomial)					
Tension (N)	1.50	2.46	3.66	4.91	4.91
Tip Load (N)	0	0	0	0	0.0196

assumed to exit exactly normal to the plate due to the tolerance between the backbone and the hole drilled in the plate, and a 2° angular error in base frame corresponds to an approximately 8 mm tip error when the robot is straight). Also, the effective stiffness of the backbone was increased due to the constraints of the standoff disks and Loctite adhesive at regular intervals. To account for these uncertainties we calibrated the effective Young's modulus and the set of XYZ Euler angles (α, β and γ) describing the orientation of the base frame.

Our calibration process was accomplished by solving an unconstrained nonlinear optimization problem to find the set of parameters which minimizes the sum of the positional errors at the tip of the device for the set of 25 experiments with straight tendon paths described in Sec. 4.4.4 and Table 4.2. In other words, for the parameter

Table 4.3: Nominal and Calibrated Parameters

Parameter	Nominal Value	Calibrated Value (Point Moment Model)	Calibrated Value (Coupled Model)
E (GPa)	210	227.9	229.6
α (deg)	180	177.7	177.9
β (deg)	0	2.2	2.2
γ (deg)	-90	-89.6	-89.7

set $P = \{E, \alpha, \beta, \gamma\}$:

$$P_{\text{cal}} = \underset{P}{\operatorname{argmin}}(\sum_{k=1}^{25} e_k)$$

where $e_k = \|\boldsymbol{p}_{model}(\ell) - \boldsymbol{p}_{data}(\ell)\|_k$ is the euclidean distance between the model tip prediction and the data in experiment k. To implement this minimization, we used the Nelder-Meade simplex algorithm, as implemented by MATLAB's `fminsearch` function.

To ensure fair comparison of the coupled model and the point moment model, the calibration procedure was performed separately for each model. Results are shown in Table 4.3. Note that the similarity in calibrated Euler angles and their low deviations from nominal values provide confidence that the correct base frame was obtained for both models. It is also important to note that the models contain the same number of parameters, so a fair comparison can be made. As expected, the calibrated values for Young's modulus are slightly higher than the nominal value of 210 GPa for spring steel, due to the increased stiffness provided by the disks and glue. Poisson's ratio was held constant at $\nu = 0.3125$ during calibration so that the shear modulus was

Table 4.4: Model Tip Errors for Straight Tendon Experiments

13 Cases with In-Plane Loads				
Tip Error Statistic (mm)	mean	std. dev.	min	max
Point Moment Model	3.5	1.4	1.2	5.6
Coupled Model	3.1	1.3	0.3	5.3

12 Cases with Out-of-Plane Loads				
Tip Error Statistic (mm)	mean	std. dev.	min	max
Point Moment Model	9.8	5.5	1.7	16.2
Coupled Model	4.1	2.1	0.6	7.9

Table 4.5: Coupled Model Tip Errors for Non-Straight Tendon Experiments

	mean	std. dev.	min	max
Tendon 5 (Helical)	5.5	2.7	1.9	10.0
Tendon 6 (Polynomial)	4.6	1.9	2.7	7.2

correctly scaled relative to Young's modulus.

4.4.4 Straight Tendon Results and Model Comparison

Table 4.1 details the location of the tendon routing paths used in our experiments in terms of $x_i(s)$ and $y_i(s)$ as defined in (4.8). We first performed 25 experiments (detailed in Table 4.2) with straight tendon paths in order to compare the accuracy of the new coupled model with that of the point moment model. We detail the tip error

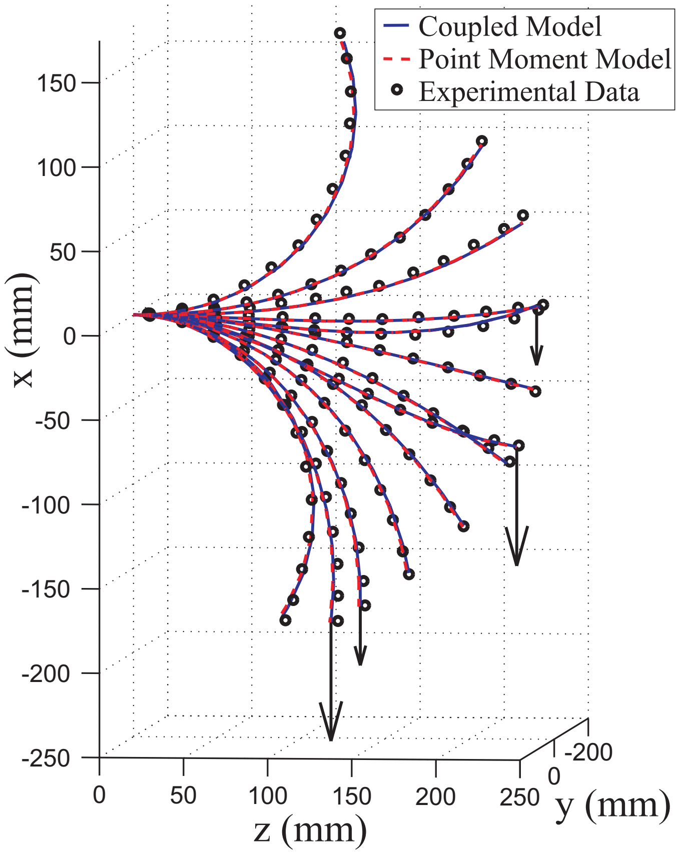

Figure 4.6: Pictured are the 13 experimental cases with in-plane external loads. The tendons on the top and bottom of the robot (tendons 1 and 3) were tensioned and vertical tip loads were applied in four of the cases. Distributed gravitational loading is present in every case. As detailed in Table 4.4, both the coupled model and the point moment model are accurate and nearly identical for in-plane loads.

statistics for both models with calibrated parameters in Table 4.4. The results for in-plane loading are accurate for both models, as shown in Figure 4.6. In contrast, for out-of-plane loads, the coupled model provides more accurate predictions (see Figure 4.7).

With calibrated parameters, the mean tip error over all 25 straight tendon experiments was 3.6 mm for the coupled model. This corresponds to 1.5% of the total arc length of the robot. Note that experimental data points lie close to the model prediction along the entire robot length, and the error increases gradually along the

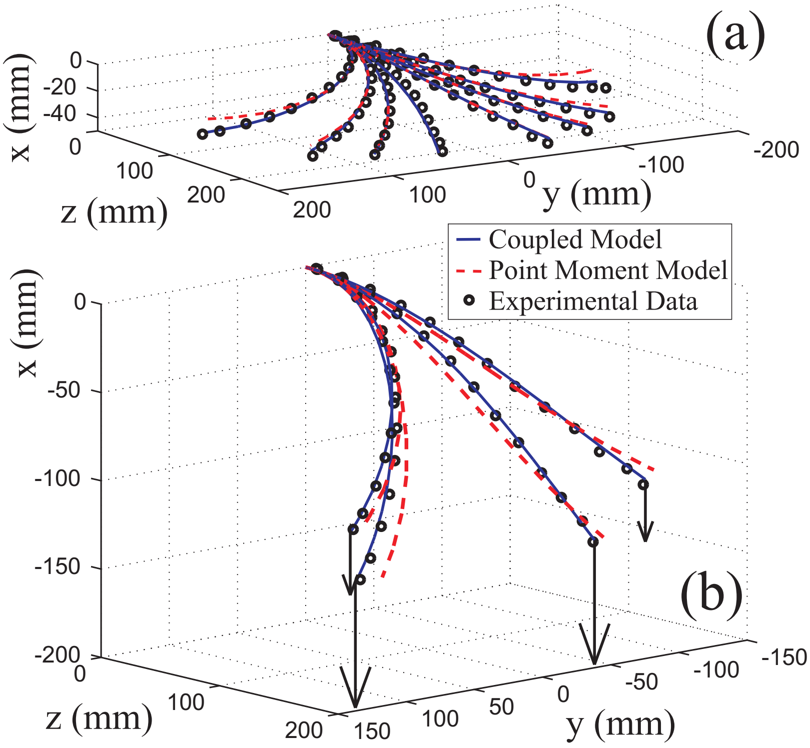

Figure 4.7: Pictured are the twelve experimental cases with out-of-plane external loads. The tendons on the left and right of the robot (tendons 2 and 4) were tensioned. (a) Distributed loading (robot self-weight) applied, (b) additional tip loads applied. As detailed in Table 4.4, the data agrees with the coupled model prediction, but the point moment model becomes inaccurate as the out-of-plane load increases, and as the curvature increases.

robot length, so that tip error normalized by the robot length is a reasonable metric for the accuracy of our model.

4.4.5 A High-Tension, Large-Load, Straight Tendon Experiment

We performed one additional straight tendon experiment to see how the two approaches compare for a case of large tension and large out-of-plane load, similar to the case which is simulated in Figure 1.3. Tendon 4 was tensioned to 6.38 N and a

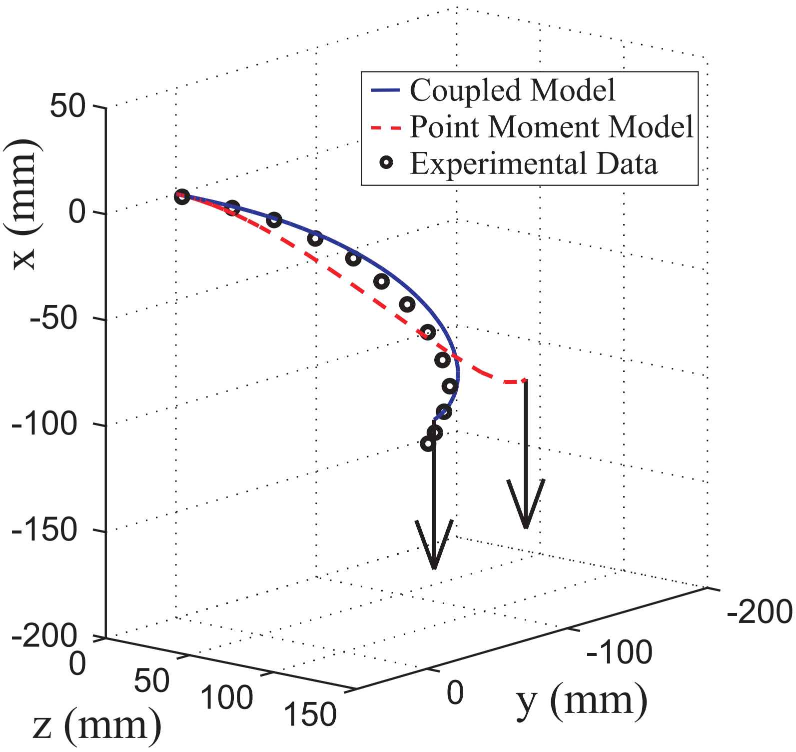

Figure 4.8: Pictured is a straight tendon case with high tension and high out-of-plane load, similar to the case depicted in Figure 1.3. The data clearly indicates that the coupled model is more accurate than the point moment model.

downward tip force of 0.196 N was applied. The resulting data and model predictions are shown in Figure 4.8. As illustrated in Figure 1.3, the two models produce very different results, and we can now see from Figure 4.8 that the coupled model prediction lies much closer to the data. Here, the tip error of the point moment model is 57 mm (23.5% of robot length), while the coupled model tip error is 12.8 mm (5.3% of robot length).

4.4.6 Experiments with Helical Tendon Routing

To explore more complex tendon routing we experimentally evaluated helical routing paths. As given in Table 4.1, our helical routing path winds through one complete

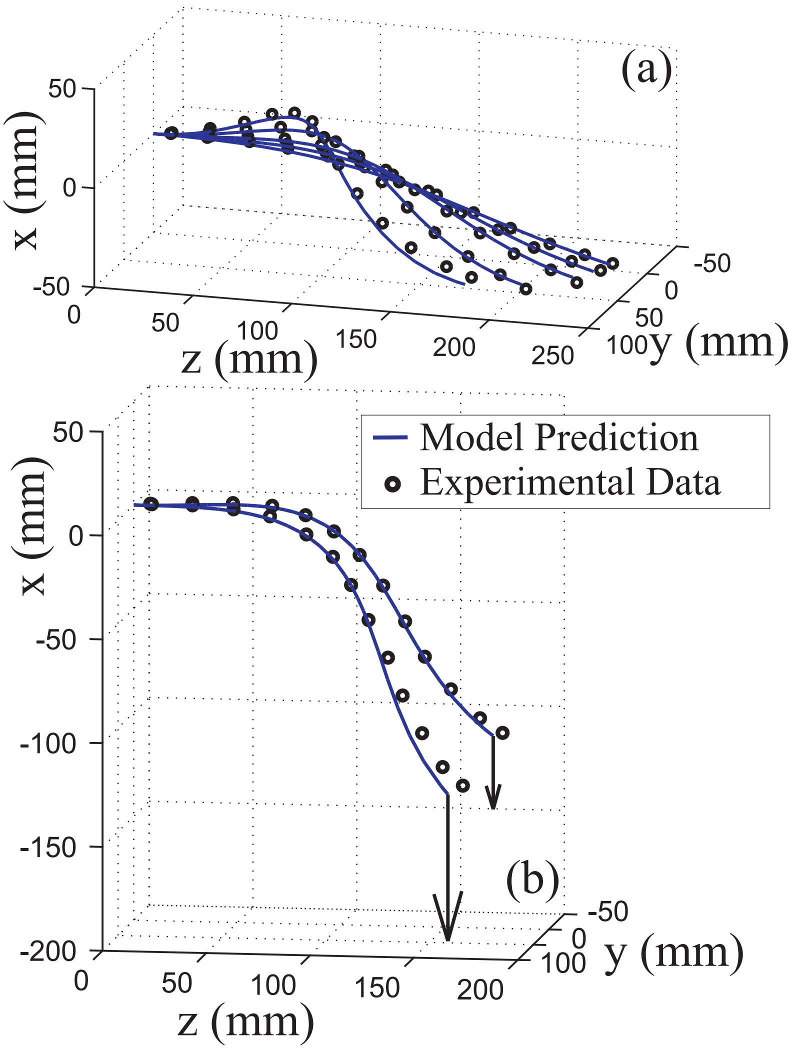

Figure 4.9: Pictured are the seven experiments performed with helical tendon routing (tendon number 5): (a) self-weight only, (b) cases with external tip loads. Numerical tip errors are given in Table 4.5 (mean 5.5 mm).

revolution as it traverses the robot from base to tip. The tensions and tip loads for these experiments are detailed in Table 4.2. Using the parameters calibrated from the previous straight tendon dataset, we plot the resulting data and model predictions in Figure 4.9 and 4.10. We see from Table 4.5 that the model agrees with the data with a mean tip error of 5.5 mm. The small increase in error over the straight tendon cases may be due to increased frictional forces, since the tension for the helical cases

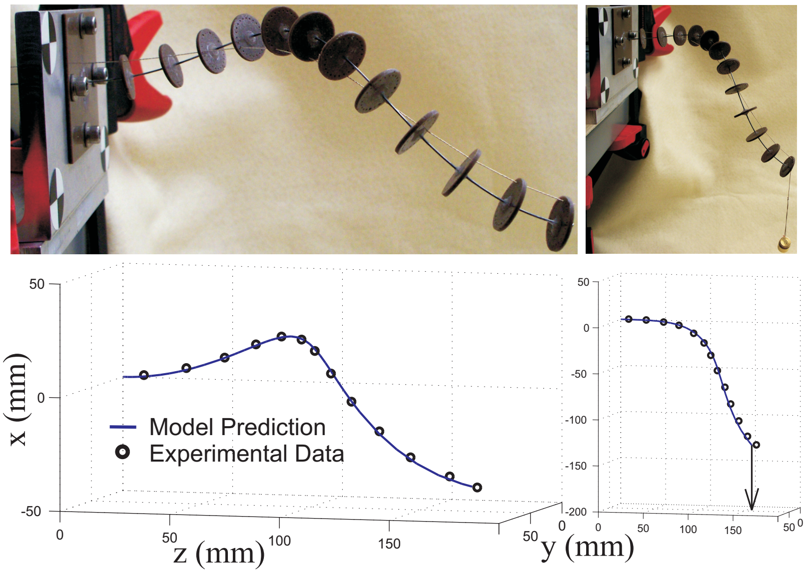

Figure 4.10: Two helical cases are shown with photographs from the same angle for better visualization. Left: The helical tendon is tensioned to 4.91 N, causing the backbone to assume an approximately helical shape which is deformed under its own weight. Right: An additional 20 g mass hung from the tip causes large overall deflection.

was higher.

4.4.7 Experiments with Polynomial Tendon Routing

In order to further illustrate our model's generality, we performed additional experiments with a general curved tendon routing choice. We parameterized the routing path variables by two trigonometric functions whose arguments are defined by a polynomial function of degree 4 as follows:

$$\begin{aligned} x_6(s) =& 8\cos(5887s^4 - 2849s^3 + 320s^2 + 6s) \\ y_6(s) =& 8\sin(5887s^4 - 2849s^3 + 320s^2 + 6s), \end{aligned} \tag{4.28}$$

where s is in meters and x_6 and y_6 are in millimeters. This routing path starts at the top of the robot, wraps around to the right side for most of the length, and

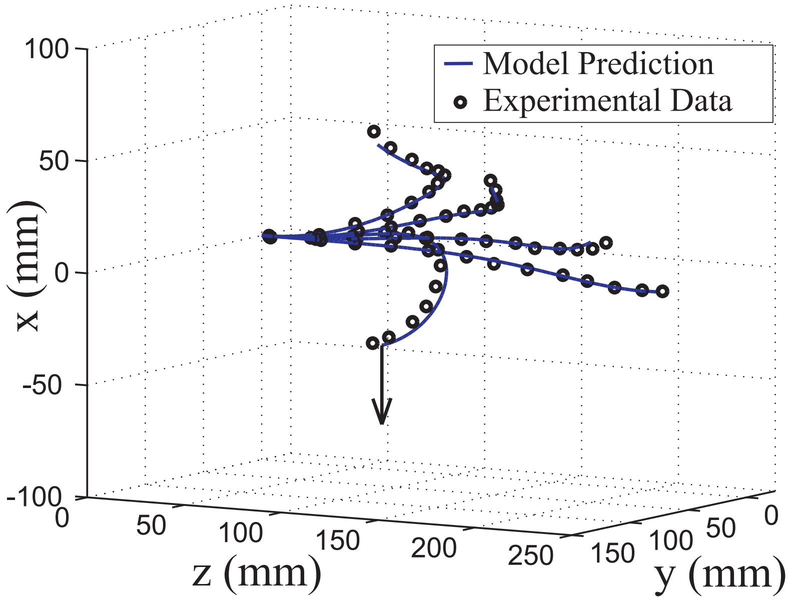

Figure 4.11: Pictured are five cases with polynomial tendon routing as specified Equation 4.28.

then returns to the top at the end of the robot. The tensions and loads are given in Table 4.2, and the results are detailed Table 4.5 and illustrated in Figure 4.11. The coupled model's predictions agree with the data, with a mean tip error of 4.6 mm. This set of experiments confirms the coupled model's ability to handle an arbitrary tendon routing choices.

4.4.8 Sources of Error

The largest source of measurement uncertainty is likely the procedure of manually placing the tip of the stylus on the robot during data capture. We estimate this uncertainty to be at most 2 mm. In general, the largest model errors occurred when the tendons were under the greatest tension. This agrees with the intuition that effects of static friction should become more significant as the tension and curvature increase. However, the low overall errors suggest that neglecting static friction is justifiable for this prototype.

4.5 Conclusions

In this chapter we have derived exact models for the forward kinematics, statics, and dynamics of continuum robots with general tendon routing experiencing external point and distributed loads. The models account for large deformations due to bending, torsion, shear, and elongation. The static model is formulated as a set of nonlinear ordinary differential equations in state vector form with boundary conditions, and the dynamic model consists of a system of hyperbolic partial differential equations.

Our experimental results demonstrated that using this approach, one can accurately predict the shape of a physical prototype with both straight and non-straight tendon routing paths and with external loading. With calibrated parameters, the mean tip error over all the experiments was 4.1 mm, or 1.7% of the total robot length. The straight tendon results also showed that the coupled model was on average twice as accurate as the point moment model for typical out-of-plane loading scenarios, and far more accurate for a case with high tension and loading.

The models developed in this chapter can be useful as design tools, and also provide the theoretical foundations for new control algorithms for tendon-actuated continuum robots. As illustrated in Figure 1.4, the design space of achievable robot shapes can be expanded by considering general tendon routing paths. We also believe that the models presented in this chapter will pave the way for new quasi-static and/or dynamic control techniques for tendon-actuated continuum robots in the future, although significant work remains to be done on efficient computational implementation (or suitable model approximations), before real-time dynamic control is possible. Furthermore the inclusion of general external loads in tendon-actuated continuum robot models is an important step forward for future practical applications, given their significant sag under self-weight and when carrying payloads.

In summary, continuum robots have the potential to increase the performance of robotic systems working in cluttered or unstructured environments, manipulating objects with the whole arm, or when compliant interaction with the environment is necessary. These capabilities appear useful in some traditional industrial robotics applications, and also in many new applications where traditional robots are not applicable due to lack of dexterity or danger of excessive force application. We believe that designs with general tendon routing, and use of static and dynamic models accounting for external loading, such as those derived in this chapter, will be key enablers of wider application of continuum robots in the future.

Chapter 5

Model-Based Control and Force Sensing

In Chapters 3 and 4, kinematic models that account for deformation due to applied loads were developed for two different continuum robots designs. For these two models and others reported in the literature, a set of nonlinear differential equations with boundary conditions must be solved to obtain the robot shape, thus making the task of computing manipulator Jacobians and compliance matrices computationally burdensome. In this chapter, we first propose a method for efficiently obtaining an arc length parametrized Jacobian and compliance matrix. Our approach involves propagating the necessary partial derivatives through the model equations, resulting in a new set of differential equations which can be solved as an initial value problem, via a single numerical integration to obtain Jacobians and compliance matrices along the robot length. We provide a specific case study using this method to obtain the Jacobian for a concentric-tube robot, and show that using this method, the kinematic model can be solved and the Jacobian obtained at rates sufficient for real-time control, using a standard desktop PC or laptop. We further describe a damped-least-squares approach to achieving inverse-kinematic control of continuum robots using the robot Jacobian. Using this method we demonstrate model-based 6 DOF teleoperation of a simulated concentric-tube robot in real time at approximately 200-300 Hz on a standard PC.

In the second half of this chapter, we explore the idea of using sensed robot deflections to estimate external forces applied to the robot via the compliance matrix. This way of achieving "intrinsic force sensing" may be particularly useful for thin continuum robots where application constraints preclude the use of traditional force sensors. We describe and simulate an Extended-Kalman-Filter-based approach to estimate forces applied at the tip of a flexible tendon-actuated robot using only uncertain measurements of the tip pose and an uncertain kinematic-static model for the robot.

5.1 Computing Jacobians and Compliance Matrices

5.1.1 Problem Statement

Models for the deformation of continuum robots with actuator values $\boldsymbol{q}$ and under a six degree-of-freedom point wrench $\boldsymbol{w}$ can be written in the following form [44,62,84]:

$$\begin{aligned} g' &= g\widehat{\boldsymbol{\xi}}(\boldsymbol{y}, g), \\ \boldsymbol{y}' &= \boldsymbol{f}(s, \boldsymbol{y}, g, \boldsymbol{q}, \boldsymbol{w}) \end{aligned} \tag{5.1}$$

where $g(s) \in \mathrm{SE}(3)$ is a homogeneous transformation defining the backbone location and orientation at arc length s, $\boldsymbol{\xi} \in \mathfrak{se}(3)$ (a body frame twist describing how g evolves in s, see Chapter 2 and [53]) is a function of a set of state variables $\boldsymbol{y}$ and possibly the matrix g, and the $'$ denotes a derivative with respect to s. (Note since we require derivatives with respect to both time and arc length, we will employ $\dot{}$ to denote a derivative with respect to time, and $'$ to denote a derivative with respect to arc length.)

At the base of the robot ($s = 0$), some subset of the elements of $\boldsymbol{y}$ are unknown, which we denote $\boldsymbol{y}_u$. These unknown variables typically include torsional and bending strains. The initial position and orientation g, and the remaining elements of $\boldsymbol{y}$, denoted by $\boldsymbol{y}_k$, may be specified in terms of $\boldsymbol{y}_u$ and the actuator positions $\boldsymbol{q}$. Thus, the boundary conditions at the proximal end of the robot are:

$$\begin{aligned} g(0) =& H(\boldsymbol{y}_u(0), \boldsymbol{q}, \boldsymbol{w}), \\ \boldsymbol{y}_k(0) =& \boldsymbol{h}(\boldsymbol{y}_u(0), \boldsymbol{q}, \boldsymbol{w}). \end{aligned} \tag{5.2}$$

At the distal end of the robot ($s = \ell$), there are general boundary conditions to be satisfied:

$$\boldsymbol{b}(\boldsymbol{y}(\ell), g(\ell), \boldsymbol{q}, \boldsymbol{w}) = \mathbf{0}. \tag{5.3}$$

Shooting methods can be used to solve such boundary value problems (BVP's). Since $\boldsymbol{b}$ is a function of the unknown initial conditions $\boldsymbol{y}_u$, a shooting method consists of using a nonlinear root-finding algorithm to iteratively converge on values for $\boldsymbol{y}_u$ which satisfy $\boldsymbol{b} = \mathbf{0}$. For a particular value of $\boldsymbol{y}_u(0)$, evaluation of $\boldsymbol{b}$ simply requires numerical integration of the initial value problem, which can be computed using standard methods such as the Runge-Kutta or Adams-Bashforth families of algorithms.

We are are interested in obtaining the spatial manipulator Jacobian, which is defined as follows [53]:

$$J^s = \left[\left(\frac{\partial g}{\partial q_1} g^{-1} \right)^{\vee} \cdots \left(\frac{\partial g}{\partial q_n} g^{-1} \right)^{\vee} \right].$$

Similarly, we define the spatial manipulator compliance matrix with respect to a tip wrench as,

$$C^s = \left[\left(\frac{\partial g}{\partial w_1} g^{-1} \right)^{\vee} \dots \left(\frac{\partial g}{\partial w_6} g^{-1} \right)^{\vee} \right].$$

These matrices can be generalized as continuous functions of arc length, and thus describe the motion of the entire robot with respect to changes in the actuator positions or the components of an applied wrench as,

$$\left(\dot{g}(s) g^{-1}(s) \right)^{\vee} = J^s(s, \boldsymbol{q}, \boldsymbol{w}) \dot{\boldsymbol{q}} + C^s(s, \boldsymbol{q}, \boldsymbol{w}) \dot{\boldsymbol{w}},$$

where the dot denotes a derivative with respect to time.

A straightforward approach to approximating J^s and C^s is to use a finite difference approximation on the BVP to compute each partial derivative. Thus, if $g(s)$ is the solution of the BVP given by (5.1), (5.2), and (5.3), the columns of the Jacobian and compliance matrix are given by

$$\begin{aligned} J^s_i &\approx \left(\frac{g_i(s) - g(s)}{\Delta q_i} g(s)^{-1} \right)^{\vee} \quad i = 1 \dots n, \\ C^s_i &\approx \left(\frac{g_i(s) - g(s)}{\Delta w_i} g(s)^{-1} \right)^{\vee} \quad i = 1 \dots 6, \end{aligned} \tag{5.4}$$

where $g_i(s)$ is the solution of the BVP with $q_i = q_i + \Delta q_i$ or $w_i = w_i + \Delta w_i$ respectively, and n is the number of actuators.

Using this method (which we henceforth call BVP finite differences, and which is depicted in Figure 5.1), the manipulator Jacobian and compliance matrix are obtained after $n + 6$ solutions of the boundary value problem. To increase computational efficiency, it is desirable to have a method which uses information from the related initial value problem (IVP) instead. In the next section, we describe such a method.

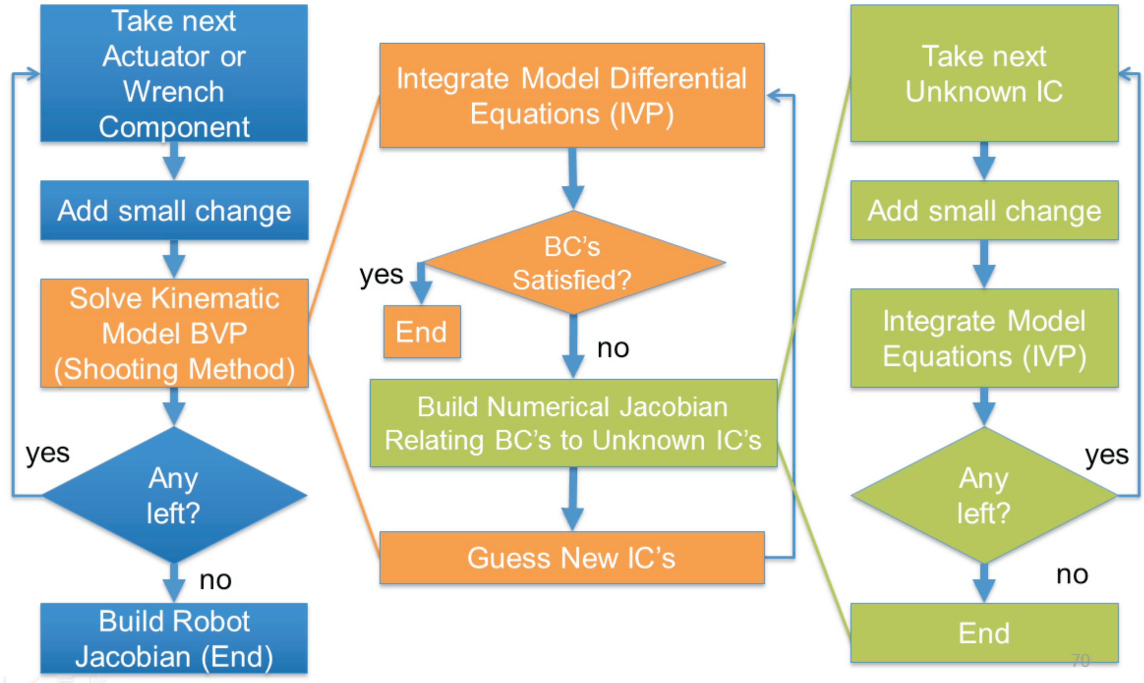

Figure 5.1: The above block diagram details the steps involved in computing the manipulator Jacobian and compliance matrices via the computationally inefficient method of performing finite difference calculations on the model BVP.

It is based on building a "Jacobian-like" matrices with respect to the IVP problem, and treating the actuator positions, the elements of the tip wrench, and the unknown initial conditions simultaneously as independent variables.

5.1.2 IVP Jacobians and Compliance Matrices

In this section, we consider the initial value problem below which is identical to our original boundary value problem given by (5.1), (5.2), and (5.3), except that the initial conditions are now specified for all variables, and the distal boundary conditions have been removed:

$$\begin{aligned}
\boldsymbol{y}_u(0) &= \boldsymbol{y}_{u,0} \\
g(0) &= H(\boldsymbol{y}_u(0), \boldsymbol{q}, \boldsymbol{w}) \\
\boldsymbol{y}_k(0) &= \boldsymbol{h}(\boldsymbol{y}_u(0), \boldsymbol{q}, \boldsymbol{w}) \\
g' &= g\widehat{\boldsymbol{\xi}}(\boldsymbol{y}, g) \\
\boldsymbol{y}' &= \boldsymbol{f}(s, \boldsymbol{y}, g, \boldsymbol{q}, \boldsymbol{w})
\end{aligned} \tag{5.5}$$

We define a Jacobian matrix E with respect to the solution of this IVP, consisting of sub-matrices E_q, E_w and E_u which describe changes in g in with respect to changes in $\boldsymbol{q}$, $\boldsymbol{w}$, and $\boldsymbol{y}_u(0)$ respectively as,

$$\begin{aligned}
E &= \left[E_q \quad E_w \quad E_u\right], \\
E_q &= \left[\left(\frac{\partial g}{\partial q_1} g^{-1}\right)^\vee \cdots \left(\frac{\partial g}{\partial q_n} g^{-1}\right)^\vee\right], \\
E_w &= \left[\left(\frac{\partial g}{\partial w_1} g^{-1}\right)^\vee \cdots \left(\frac{\partial g}{\partial w_6} g^{-1}\right)^\vee\right], \\
E_u &= \left[\left(\frac{\partial g}{\partial y_{u,1}(0)} g^{-1}\right)^\vee \cdots \left(\frac{\partial g}{\partial y_{u,m}(0)} g^{-1}\right)^\vee\right].
\end{aligned}$$

Similarly, we construct matrices B_q, B_w, and B_u which describe the change in the function $\boldsymbol{b}$ defined in (5.3) as,

$$\begin{aligned}
B &= \left[B_q \quad B_w \quad B_u\right], \\
B_q &= \frac{\partial \boldsymbol{b}}{\partial \boldsymbol{q}}, \quad B_w = \frac{\partial \boldsymbol{b}}{\partial \boldsymbol{w}}, \quad B_u = \frac{\partial \boldsymbol{b}}{\partial \boldsymbol{y}_u(0)}.
\end{aligned}$$

Using the above definitions, one can write down the time derivative of the robot pose, as well as the rate of change of the boundary condition function in terms of the time derivatives of $\boldsymbol{q}$, $\boldsymbol{w}$, and $\boldsymbol{y}_u(0)$ as,

$$\left(\dot{g}g^{-1}\right)^\vee = E_q\dot{\boldsymbol{q}} + E_w\dot{\boldsymbol{w}} + E_u\dot{\boldsymbol{y}}_u(0) \tag{5.6}$$

$$\dot{\boldsymbol{b}} = B_q\dot{\boldsymbol{q}} + B_w\dot{\boldsymbol{w}} + B_u\dot{\boldsymbol{y}}_u(0). \tag{5.7}$$

Now, if the original boundary value problem has been solved, we want $\boldsymbol{b}$ to remain at zero for any $\dot{\boldsymbol{q}}$ and $\dot{\boldsymbol{w}}$. Thus, if we set $\dot{\boldsymbol{b}} = 0$ in (5.7), we can solve for the $\dot{\boldsymbol{y}}_u(0)$ which will continue to satisfy the boundary conditions, namely,

$$\dot{\boldsymbol{y}}_u(0) = -B_u^\dagger \left(B_q\dot{\boldsymbol{q}} + B_w\dot{\boldsymbol{w}}\right)$$

Substituting the result into (5.6) yields

$$\left(\dot{g}g^{-1}\right)^\vee = \left(E_q - E_uB_u^\dagger B_q\right)\dot{\boldsymbol{q}} + \left(E_w - E_uB_u^\dagger B_w\right)\dot{\boldsymbol{w}},$$

from which we can see that the actual manipulator Jacobian and compliance matrix (as continuous functions of s) can be expressed in terms of the initial value Jacobians as follows,

$$J^s(s) = E_q(s) - E_u(s)B_u^\dagger B_q \tag{5.8}$$

$$C^s(s) = E_w(s) - E_u(s)B_u^\dagger B_w. \tag{5.9}$$

In the following sections we discuss two ways of computing E and B: approximation by finite differences, and derivation of differential equations that define E and B exactly.

5.1.3 IVP Matrices Via Finite Differences

If $g(s)$ is the solution of the BVP, it is straightforward to approximate the columns of E and B matrices from a finite difference method on the IVP. Defining the vector $\boldsymbol{x} = [q_1, ..., q_n, w_1, ..., w_6, y_{u,1}(0), ..., y_{u,m}]^T$ to contain all of the variables with respect to which we are interested in obtaining partial derivatives, we can approximate the i^{th} columns of E and B as

$$
\begin{aligned}
E_i &\approx \left(\frac{g_i(s) - g(s)}{\Delta x_i} g^{-1}(s)\right)^{\vee}, \\
B_i &\approx \frac{\boldsymbol{b}_i - \boldsymbol{b}}{\Delta x_i}
\end{aligned}
$$

where $g_i(s)$ and $\boldsymbol{b}_i(s)$ are obtained from the solution of the IVP with $x_i = x_i + \Delta x_i$. With this method (which we call IVP finite differences, and which is depicted in diagram in Figure 5.2), the actual Jacobian and compliance matrices are obtained via (5.8) and (5.9) after $n + m + 6$ numerical integrations of the IVP problem defined in (5.5), where m is the number of elements in $\boldsymbol{y}_u(0)$. This requires much less computation than the finite difference BVP algorithm in (5.4) because when using a shooting method, each BVP solution usually requires m IVP integrations to obtain the gradients and move one step. Thus, even if the shooting method converges in a single step (which is not guaranteed), the number of IVP integrations required by implementation of (5.4) is $(m)(n + 6)$.

Next, we propose a method which is not based on finite difference approximations, but on deriving a new set of differential equations which define E and B exactly. Using this method, E and B are obtained after one integration of an IVP (albeit a much larger one than the one required for forward kinematics). Our simulation results in Section 5.2.1 show that this method provides an significant improvement in computational efficiency over both BVP and IVP finite differencing.

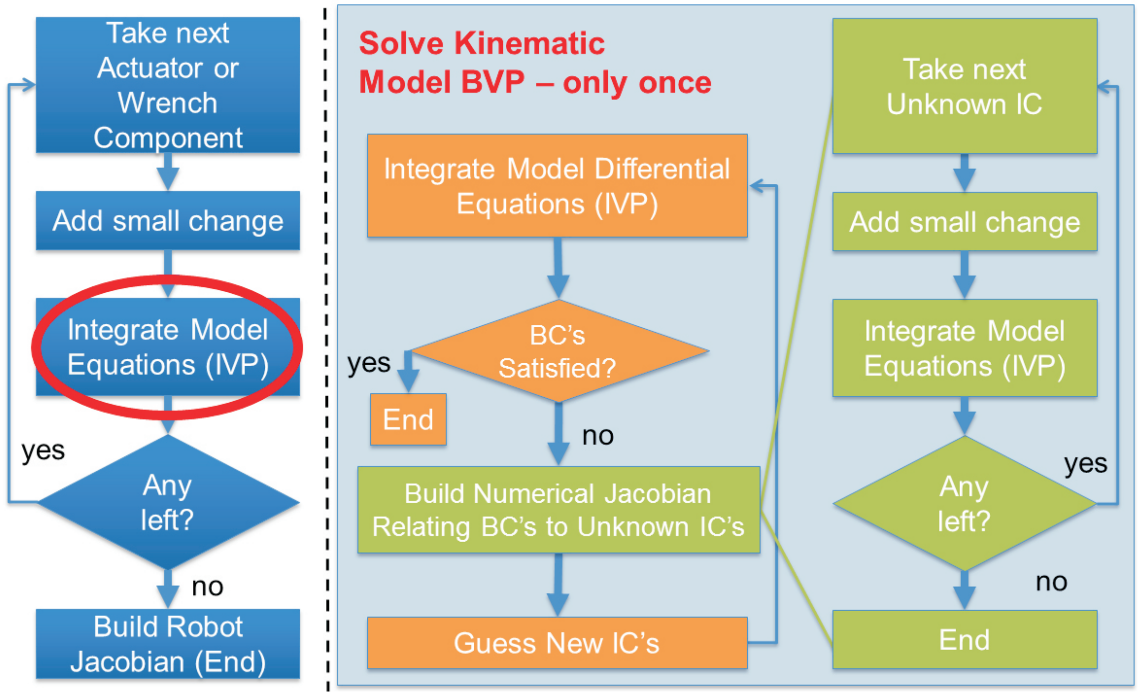

Figure 5.2: The above block diagram details the steps involved in computing the manipulator Jacobian and compliance matrices via the method of performing finite difference calculations on the model IVP. Though much more efficient than the method of BVP finite differences, the derivative propagation method provides an even greater increase in efficiency.

5.1.4 Derivative Propagation Approach

As a brief aside to illustrate our basic approach in derivative propagation, consider a simple example IVP,

$$\boldsymbol{y}(0) = \boldsymbol{h}(\boldsymbol{q}), \quad \boldsymbol{y}' = \boldsymbol{f}(s, \boldsymbol{y}), \tag{5.10}$$

and suppose that we are interested in obtaining a matrix V describing how $\boldsymbol{y}$ changes with respect to $\boldsymbol{q}$, namely,

$$V = \frac{\partial \boldsymbol{y}}{\partial \boldsymbol{q}}.$$

We can differentiate V with respect to s, and use (5.10) to obtain

$$\frac{dV}{ds} = \frac{d}{ds}\left(\frac{\partial \boldsymbol{y}}{\partial \boldsymbol{q}}\right) = \frac{\partial}{\partial \boldsymbol{q}}\left(\frac{d\boldsymbol{y}}{ds}\right) = \frac{\partial \boldsymbol{f}}{\partial \boldsymbol{q}} = \frac{\partial \boldsymbol{f}}{\partial \boldsymbol{y}}\frac{\partial \boldsymbol{y}}{\partial \boldsymbol{q}}.$$

Then, taking the partial derivative of the initial conditions, we obtain an IVP that defines V,

$$V(0) = \frac{\partial \boldsymbol{h}}{\partial \boldsymbol{q}}, \qquad \frac{dV}{ds} = \frac{\partial \boldsymbol{f}}{\partial \boldsymbol{y}}V. \tag{5.11}$$

The above technique is often used in the implementation of shooting methods to supply derivative information for the update step (to obtain B_u), and we will adapt this technique in the subsection below to obtain E and B for the IVP in (5.5).

5.1.5 IVP Matrices Via Derivative Propagation

We wish to obtain a differential equation which defines the matrix E. Considering the i^{th} column of the matrix E,

$$E_{q,i} = \left(\frac{\partial g}{\partial x_i}g^{-1}\right)^{\vee}, \tag{5.12}$$

we can derive an expression for its arc length derivative as follows:

$$\begin{aligned}\frac{d}{ds}E_i &= \left(\frac{\partial}{\partial x_i}\left(\frac{dg}{ds}\right)g^{-1} + \frac{\partial g}{\partial x_i}\frac{d}{ds}\left(g^{-1}\right)\right)^{\vee} \\ &= \left(\frac{\partial g}{\partial x_i}\widehat{\boldsymbol{\xi}}g^{-1} + g\frac{\partial \widehat{\boldsymbol{\xi}}}{\partial x_i}g^{-1} + \frac{\partial g}{\partial x_i}\frac{d}{ds}\left(g^{-1}\right)\right)^{\vee} \\ &= \left(g\frac{\partial \widehat{\boldsymbol{\xi}}}{\partial x_i}g^{-1}\right)^{\vee} = Ad_g\frac{\partial \boldsymbol{\xi}}{\partial x_i},\end{aligned}$$

where we have used $g' = g\widehat{\boldsymbol{\xi}}$, and the fact that

$$\frac{d}{ds}\left(g^{-1}\right) = -\widehat{\boldsymbol{\xi}}g^{-1}.$$

Ad_g is the adjoint transformation of g, defined as

$$Ad_g = \begin{bmatrix} R & \widehat{\boldsymbol{p}}R \\ 0 & R \end{bmatrix}.$$

By expanding $\frac{\partial \boldsymbol{\xi}}{\partial x_i}$, we can express E_i' as

$$E_i' = Ad_g \left(\frac{\partial \boldsymbol{\xi}}{\partial \boldsymbol{y}} V_i + \frac{\partial \boldsymbol{\xi}}{\partial \mathrm{vec}(g)} \mathrm{vec}\left(\widehat{E}_i g \right) \right) \tag{5.13}$$

where we have used (5.12) to substitute in for $\frac{\partial g}{\partial x_i}$, vec() simply reshapes a matrix into a column vector, and

$$V = [V_q \;\; V_w \;\; V_u] = \frac{\partial \boldsymbol{y}}{\partial \boldsymbol{x}}.$$

Similarly, we find that the columns of B can be expressed as

$$B_i = \frac{\partial \boldsymbol{b}()}{\partial \boldsymbol{y}} V_i + \frac{\partial \boldsymbol{b}()}{\partial \mathrm{vec}(g)} \mathrm{vec}\left(\widehat{E}_i g \right) + \frac{\partial \boldsymbol{b}()}{\partial x_i}. \tag{5.14}$$

where we use $\partial \boldsymbol{b}()$ to denote the partial derivative of the function $\boldsymbol{b}(\boldsymbol{y}(\ell), g(\ell), \boldsymbol{q}, \boldsymbol{w})$ with respect to the argument appearing in the given term's denominator. This notation is necessary for clarity because $\boldsymbol{q}$ and $\boldsymbol{w}$ affect the value of $\boldsymbol{b}$ both directly and also indirectly through changes in $\boldsymbol{y}(\ell)$ and $g(\ell)$.

We now only need an equation for V to have a complete set of equations defining E and B. Thus, we obtain

$$V_i' = \frac{\partial \boldsymbol{f}()}{\partial \boldsymbol{y}} V_i + \frac{\partial \boldsymbol{f}()}{\partial \mathrm{vec}(g)} \mathrm{vec}\left(\widehat{E}_{x,i} g \right) + \frac{\partial \boldsymbol{f}()}{\partial x_i}, \tag{5.15}$$

At $s = 0$ it is straightforward to calculate the $V(0)$ and $E(0)$ from the initial conditions:

$$\begin{aligned} V(0) &= \begin{bmatrix} \frac{\partial \boldsymbol{y}(0)}{\partial \boldsymbol{q}} & \frac{\partial \boldsymbol{y}(0)}{\partial \boldsymbol{w}} & \frac{\partial \boldsymbol{y}(0)}{\partial \boldsymbol{y}_u(0)} \end{bmatrix} \\ E_{q,i}(0) &= \left(\frac{\partial H}{\partial q_i} g(0)^{-1} \right)^{\vee}, \\ E_{w,i}(0) &= \left(\frac{\partial H}{\partial w_i} g(0)^{-1} \right)^{\vee}, \\ E_{u,i}(0) &= \left(\frac{\partial H}{\partial y_{u,i}(0)} g(0)^{-1} \right)^{\vee} \end{aligned} \tag{5.16}$$

We now have an IVP, consisting of (5.13), (5.14), (5.15), and (5.16), which when integrated simultaneously with the equations in (5.5), yields the initial value matrices E and B from which we can obtain J^s and C^s using (5.8) and (5.9). Furthermore, we obtain the matrix B_u, which we can use in our shooting method to solve the boundary value problem efficiently. The resulting derivative propagation algorithm is summarized in the diagram in Figure 5.3.

5.2 Example: The Concentric-Tube Robot Model with External Loading

In this section we apply the methods derived above to obtain a continuous set of Jacobians and compliance matrices along the length of a concentric-tube robot, or active cannula. A model for the statics of an active cannula under external loads was derived in Chapter 3, and we give a brief, self-contained statement of those model equations here before applying the methods of Section 5.1.4.

For the loaded model example, we consider the case of n tubes with piecewise-constant pre-curvature, $\boldsymbol{u}_i = [k_i \;\; 0 \;\; 0]^T$, and zero distributed loads, with a point

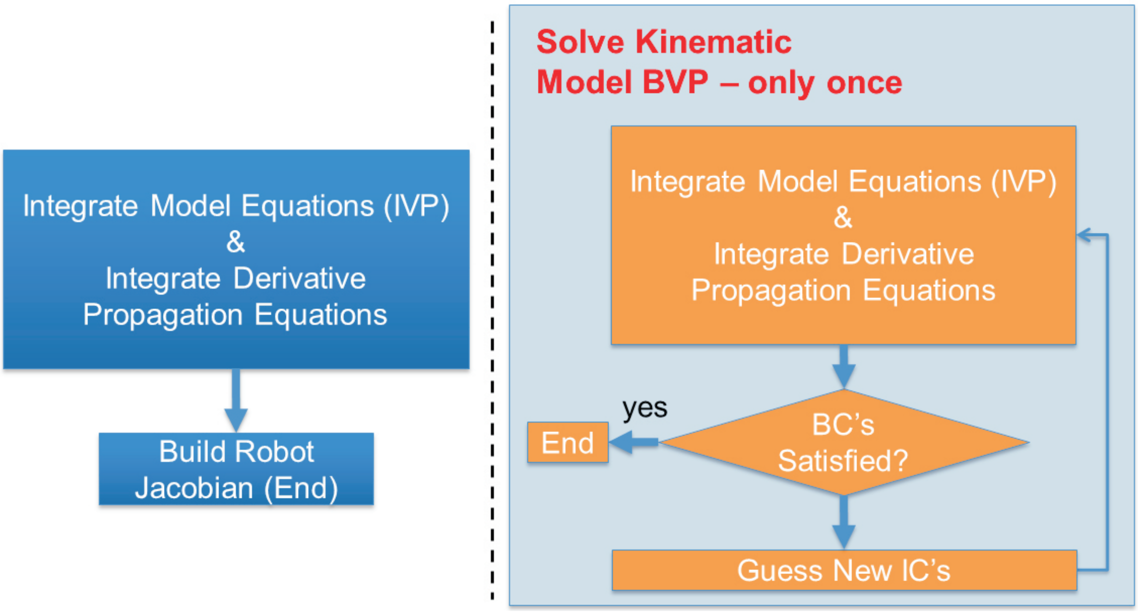

Figure 5.3: The above block diagram details the steps involved in computing the manipulator Jacobian and compliance matrices via the method of obtaining IVP matrices through derivative propagation. This method eliminates all finite difference loops, and appears to be more computationally efficient than either BVP finite differences or IVP finite differences.

wrench $\boldsymbol{w}$ applied to the tip of the robot, consisting of a point force $\boldsymbol{F}$ and a point moment $\boldsymbol{L}$. In this case, the loaded model equations in (3.58) reduce to

$$\begin{aligned} \dot{\boldsymbol{p}}_1 &= R_1 \boldsymbol{e}_3 \\ \dot{R}_1 &= R \widehat{\boldsymbol{u}}_1 \\ \dot{\theta}_i &= u_{iz} - u_{1z} \qquad \text{for } i = 2...n \\ \dot{u}_{iz} &= -\frac{k_i E_i I_i}{G_i J_i} u_{iy} \quad \text{for } i = 1...n \\ \dot{\boldsymbol{m}}^b_{xy} &= \left(-\widehat{\boldsymbol{u}}_1 \boldsymbol{m}^b - \widehat{\mathbf{e}}_3 R_1^T \boldsymbol{F}\right)_{xy} \end{aligned} \tag{5.17}$$

where the following relationships are used to obtain m^b_z, $\boldsymbol{u}_{1xy}$, and $\boldsymbol{u}_{iy}$ from the state variables:

$$\begin{aligned} m_z^b =& \sum_{i=1}^{n} G_i J_i u_{iz}, \\ \boldsymbol{u}_{1xy} =& \frac{1}{\sum_{i=1}^{n} E_i I_i} \left(\boldsymbol{m}_{xy}^b + \sum_{i=1}^{n} \left[\begin{smallmatrix} \cos\theta_i \\ \sin\theta_i \end{smallmatrix} \right] E_i I_i k_i \right), \\ u_{iy} =& [\sin\theta_i \quad \cos\theta_i]\, \boldsymbol{u}_{1xy}. \end{aligned} \tag{5.18}$$

The initial conditions at $s = 0$ are

$$\begin{aligned} \boldsymbol{p}_1(0) =& [0\ 0\ 0]^T, \\ R_1(0) =& \left[\begin{smallmatrix} \cos(\alpha_1 - \beta_1 u_{1z}(0)) & -\sin(\alpha_1 - \beta_1 u_{1z}(0)) & 0 \\ \sin(\alpha_1 - \beta_1 u_{1z}(0)) & \cos(\alpha_1 - \beta_1 u_{1z}(0)) & 0 \\ 0 & 0 & 1 \end{smallmatrix} \right], \\ \theta_i(0) =& \alpha_i - \alpha_1 - (\beta_i u_{iz}(0) - \beta_1 u_{1z}(0)). \end{aligned} \tag{5.19}$$

and the boundary conditions are

$$\begin{aligned} 0 &= G_1 J_1 u_{1z}(\ell_1) - \boldsymbol{e}_3^T R_1^T \boldsymbol{L} \\ 0 &= G_i J_i u_{iz}(\ell_i), \qquad\qquad \text{for } i = 2...n \\ 0 &= \boldsymbol{m}_{xy}^b(\ell_1) - \left(R_1^T \boldsymbol{L} \right)_{xy}. \end{aligned} \tag{5.20}$$

Thus, for this system, $\boldsymbol{y} = \left[\theta_2, ..., \theta_n, u_{1z}, ..., u_{nz}, m_x^b, m_y^b \right]^T$, the actuator variables are $\boldsymbol{q} = [\alpha_1, ...\alpha_n, \beta_1, ...\beta_n]^T$, the vector of unknown initial conditions is $\boldsymbol{y}_u(0) = \left[u_{1z}(0), ..., u_{nz}(0), m_x^b(0), m_y^b(0) \right]^T$, and the boundary condition function is

$$\begin{aligned} \boldsymbol{b} = \Big[& G_1 J_1 u_{1z}(\ell_1) - \boldsymbol{e}_3^T R_1^T \boldsymbol{L}, \\ & G_2 J_2 u_{2z}(\ell_2), ...G_n J_n u_{nz}(\ell_i), \\ & m_x(\ell_1) - \left(R_1^T \boldsymbol{L} \right)_x, \\ & m_y(\ell_1) - \left(R_1^T \boldsymbol{L} \right)_y \Big]^T, \end{aligned} \tag{5.21}$$

For clarity, we further define a vector $\boldsymbol{x}$ to contain all the variables with respect to which we are interested in obtaining the partial derivatives, namely

$$\boldsymbol{x} = \left[\boldsymbol{q}^T, \boldsymbol{F}^T, \boldsymbol{L}^T, \boldsymbol{y}_u^T(0) \right]^T \tag{5.22}$$

The k^{th} column of V contains the following partial derivatives

$$\begin{aligned}
\frac{\partial \dot{\theta}_i}{\partial x_k} =& \frac{\partial u_{iz}}{\partial x_k} - \frac{\partial u_{1z}}{\partial x_k} \\
\frac{\partial \dot{u}_{iz}}{\partial x_k} =& -\frac{k_i E_i I_i}{G_i J_i} \frac{\partial u_{iy}}{\partial x_k} \\
\frac{\partial \dot{\boldsymbol{m}}^b_{xy}}{\partial x_k} =& \Big(-\frac{\partial \widehat{\boldsymbol{u}}_1}{\partial x_k} \boldsymbol{m}^b - \widehat{\boldsymbol{u}}_1 \frac{\partial \boldsymbol{m}^b}{\partial x_k} - \widehat{\boldsymbol{e}}_3 \frac{\partial R_1^T}{\partial x_k} \boldsymbol{F} - \widehat{\boldsymbol{e}}_3 R_1^T \frac{\partial \boldsymbol{F}}{\partial x_k} \Big) \Big|_{xy},
\end{aligned} \tag{5.23}$$

and the derivative of the k^{th} column of E is

$$\dot{E}_k = Ad_g \begin{bmatrix} \mathbf{0} \\ \\ \frac{\partial \boldsymbol{u}_1}{\partial x_k} \end{bmatrix} \tag{5.24}$$

The quantities $\frac{\partial m_z}{\partial x_k}$, $\frac{\partial u_{iy}}{\partial x_k}$, $\frac{\partial \boldsymbol{u}_{1xy}}{\partial x_k}$, and $\frac{\partial R_1}{\partial x_k}$ are used in the above computations. They can each be obtained from the elements of V and E as follows:

$$\begin{aligned}
\frac{\partial m_z}{\partial x_k} =& \sum_{i=1}^{n} G_i J_i \frac{\partial u_{1z}}{\partial x_k} \\
\frac{\partial u_{iy}}{\partial x_k} =& \frac{\partial \theta_i}{\partial x_k} \left[-\cos\theta_i \quad \sin\theta_i \right] \boldsymbol{u}_{1xy} + \left[-\sin\theta_i \quad \cos\theta_i \right] \frac{\partial \boldsymbol{u}_{1xy}}{\partial x_k} \\
\frac{\partial \boldsymbol{u}_{1xy}}{\partial x_k} =& \frac{1}{\sum_{i=1}^{n} E_i I_i} \left(\frac{\partial \boldsymbol{m}^b_{xy}}{\partial x_k} + \sum_{i=1}^{n} \left[\begin{smallmatrix} -\sin\theta_i \\ \cos\theta_i \end{smallmatrix} \right] E_i I_i k_i \right) \\
\frac{\partial R_1}{\partial x_k} =& \left(\left[0_{3x3} \ I_{3x3} \right] E_k \right)^{\wedge} R_1.
\end{aligned} \tag{5.25}$$

We obtain initial conditions for E and V at $s = 0$ by directly differentiating the initial conditions.

We note that the state variables in (5.17) are continuous along the entire robot, but their derivatives are discontinuous at points where tubes end or undergo step-changes in pre-curvature. If the arc-length location of a particular discontinuity is a function of β_i, and it can be shown that the columns V_{β_i} and E_{β_i} undergo transitions across the boundary as follows:

$$V^+_{\beta_i} = V^-_{\beta_i} + \dot{\boldsymbol{y}}^- - \dot{\boldsymbol{y}}^+$$

$$E^+_{\beta_i} = E^-_{\beta_i} + Ad_g \boldsymbol{\xi}^- - Ad_g \boldsymbol{\xi}^+.$$

where $-$ and $+$ superscripts indicate a value as approached from the left and the right, respectively. At the end of the robot, the same transition occurs with $\dot{\boldsymbol{y}}^+ = 0$ and $\boldsymbol{\xi}^+ = 0$.

After integrating V and E, the columns of the matrix $B = \frac{\partial \boldsymbol{b}}{\partial \boldsymbol{x}}$ can be calculated as

$$\begin{aligned}
\frac{\partial \boldsymbol{b}}{\partial x_k} =& \Big[G_1 J_1 \frac{\partial u_{1z}(\ell_1)}{\partial x_k} - \boldsymbol{e}_3^T \left(\frac{\partial R_1^T(\ell_1)}{\partial x_k} \boldsymbol{L} + R_1^T(\ell_1) \frac{\partial \boldsymbol{L}}{\partial x_k} \right), \\
& G_2 J_2 \frac{\partial u_{2z}(\ell_2)}{\partial x_k}, \ldots, G_n J_n \frac{\partial u_{nz}(\ell_n)}{\partial x_k}, \\
& \frac{\partial m_x^b(\ell_1)}{\partial x_k} - \left(\frac{\partial R_1^T(\ell_1)}{\partial x_k} \boldsymbol{L} \right)_x - \left(R_1^T(\ell_1) \frac{\partial \boldsymbol{L}}{\partial x_k} \right)_x, \\
& \frac{\partial m_y^b(\ell_1)}{\partial x_k} - \left(\frac{\partial R_1^T(\ell_1)}{\partial x_k} \boldsymbol{L} \right)_y - \left(R_1^T(\ell_1) \frac{\partial \boldsymbol{L}}{\partial x_k} \right)_y \Big]^T.
\end{aligned} \tag{5.26}$$

5.2.1 Simulations Evaluating Computational Efficiency

We now provide simulation results using the model above for a concentric-tube robot with three tubes. Each tube has a straight section at its proximal end followed by a distal section with constant curvature. The diameters, lengths, curvatures, and mechanical properties of the tubes used in our simulation are provided in Table 5.1.

We used the derivative propagation approach to solve the inverse kinematics problem via simple resolved rate servoing, commanding tip velocities in the desired direction. We commanded the tip of the cannula to trace the outline of the letter “V”, as shown in Figure 5.4 (left). To illustrate the correctness of the Jacobian when the robot is experiencing an external load, we performed the same simulation with a 0.4 N downward force applied to the tip of the cannula. Results of this simulation are shown in Figure 5.4 (right). Intuition suggests that the body of the robot will have

Table 5.1: Physical Parameters for Tubes used in Simulations

	Tube 1 (Inner)	Tube 2 (Middle)	Tube 3 (Outer)
Inner Diameter (mm)	0.50	1.25	2.00
Outer Diameter (mm)	1.00	1.75	2.50
Straight Length (mm)	450	250	100
Curved Length (mm)	150	150	100
Curvature (m^{-1})	20	10	5
Young's Mod. (E) (GPa)	60	60	60
Shear Mod. (J) (GPa)	23.1	23.1	23.1

to extend further upward in order to compensate for the load at its tip, and this behavior is visible in the figure.

We further compared the computational efficiency of the three approaches in this chapter in a series of experiments, the results of which are shown in Table 5.2. The Jacobian was calculated at 100 evenly distributed configuration-space points using three numerical integration schemes with a fixed arc length step size of 0.01 m: a fourth/fifth order Runge Kutta scheme, a second/third order Runge-Kutta scheme, and a fourth order Adams-Bashforth multi-step method. All were implemented in MATLAB, running in the Windows operating system, on a laptop computer with a 2.8 GHz dual core processor. In these results, the derivative propagation approach shows a clear advantage over the other methods. By implementing the model and derivative-propagating approach in C++, we were able to compute the model solution and the

Table 5.2: Computation Times for Proposed Methods

Integration Scheme	BVP Finite Differences	IVP Finite Differences	Derivative Propagation
RK 4/5	2.594 s	0.457 s	0.137 s
RK 2/3	1.494 s	0.251 s	0.076 s
AB 4	0.940 s	0.161 s	0.040 s

Jacobian at a rate of 1000 Hz. Thus, the investment in developing computationally efficient algorithms in this section will be essential to our efforts to create of a high-performance kinematic control system.

5.3 Control Algorithms for Concentric-Tube Robots

In this section we outline an algorithm for quasi-static control of concentric-tube robots. Though concentric-tube robots have dynamics, the prototypes developed thus far have all had high stiffness and low mass characteristics, so that that their dynamic are typically stable and very fast. Therefore, we are primarily concerned with the quasi-static inverse kinematics problem, namely how to determine the static actuator values (rotations and translations of the tube bases) that will produce a desired end-effector pose in steady-state. Since we can obtain forward kinematic solutions and Jacobians at 1000 Hz, our approach to solving this problem in the context of human-input teleoperation will be to adapt differential-inverse-kinematics strategies from the well-established body of literature on kinematic control to our

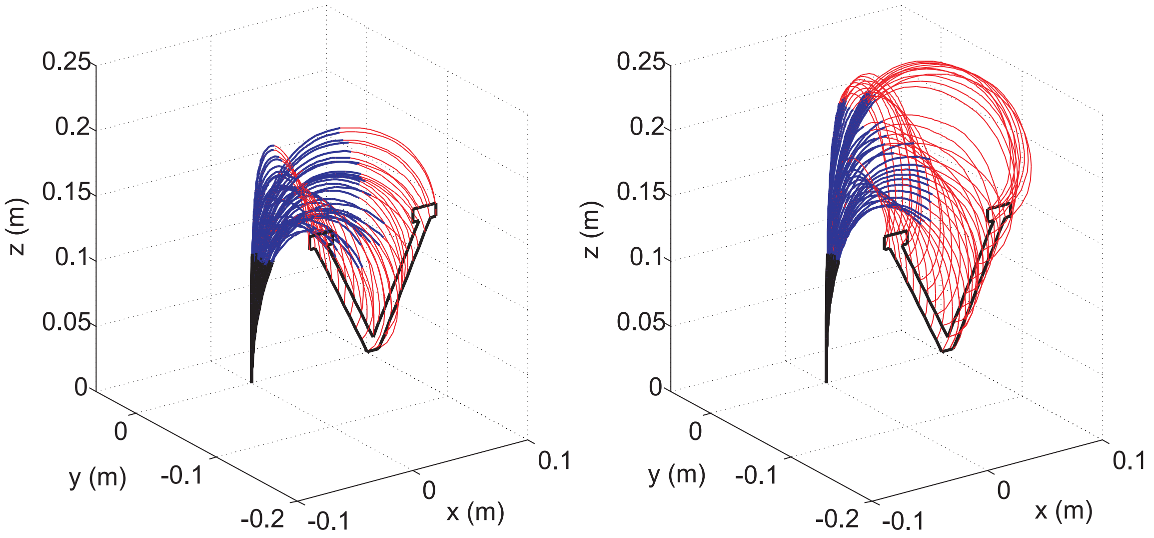

Figure 5.4: The three tube active cannula described in Table 5.1 traces the outline of the letter “V”, with no external load (left), and while under a constant tip force of 0.4 N in the negative z-direction (right). The inverse kinematic solution is achieved by computing the Jacobian and compliance matrix using the proposed approach. The inner, middle, and outer tubes are shown in red, blue, and black respectively.

particular robot architecture. Using the robot Jacobian, we implementing a general “resolved-rates” type of algorithm in order to quickly converge on inverse-kinematics solutions in real time.

5.3.1 General Damped-Least-Squares (DLS) Formulation

Perhaps the earliest work on differential-inverse-kinematics is that of Whitney [96], who coined the phrase “resolved rates” to describe the process of converting desired workspace velocities into their corresponding actuator-space velocities. This and other early works have been summarized in a review paper by Arati and Walker [6]. Difficulties that arise when trying to control robots along the general non-pre-planned trajectories that arise in teleoperation include (1) maintaining algorithm stability and avoiding extremely high actuator velocities when the robot is near a singular configuration, (2) avoiding joint limits, and (3) dealing with the issue of non-homogeneous units that arises when controlling both position and orientation, and when different actuator types are used, and (4) resolving any redundant degrees of freedom.

In order to resolve all of these issues we have adopted a generalized "damped-least-squares" approach to the differential-inverse-kinematics problem as proposed by Wampler in [88] and reviewed in [6]. The basic approach is to convert the problem to finding the actuator velocities which minimize a custom-built objective function which takes into account all of the competing goals (accurately tracking the desired trajectory, maintaining stability, limiting actuator velocities, and avoiding actuator limits and other undesirable configurations). The form of our general objective function is shown below:

$$F = \frac{1}{2}\left(\underbrace{\left(J\dot{\boldsymbol{q}} - \dot{\boldsymbol{\xi}}_0\right)^T W_0 \left(J\dot{\boldsymbol{q}} - \dot{\boldsymbol{\xi}}_0\right)}_{\text{Weighted Tracking Accuracy}} + \sum_{i=1}^{m} \underbrace{\left(\dot{\boldsymbol{q}} - \boldsymbol{v}_i\right)^T W_i \left(\dot{\boldsymbol{q}} - \boldsymbol{v}_i\right)}_{\text{Damping \& Avoiding}}\right), \tag{5.27}$$

where $\dot{\boldsymbol{q}}$ is the vector of actuator velocities, and $\dot{\boldsymbol{\xi}}_0$ is the desired end-effector velocity vector (which may contain both linear and angular components). The $\boldsymbol{v}_i$ are desired actuator velocity vectors, which may be set to zero to achieve damping, or to the scaled gradient of an objective function which penalizes closeness to undesirable configurations, and W_i are non-negative symmetric weighting matrices which may be constant or configuration dependent. Setting $\frac{\partial F}{\partial \dot{\boldsymbol{q}}} = 0$, we find that the necessary condition for $\dot{\boldsymbol{q}}$ to minimize F is

$$\dot{\boldsymbol{q}} = \left(J^T W_0 J + \sum_{i=1}^{m} W_i\right)^{-1} \left(J^T W_0 \dot{\boldsymbol{\xi}}_0 + \sum_{i=1}^{n} W_i \boldsymbol{v}_i\right). \tag{5.28}$$

In the case where $m = 1$, $W_0 = I$, $\boldsymbol{v}_1 = 0$ and $W_1 = \lambda I$, this solution reduces to the standard damped-least-squares pseudo-inverse solution

$$\dot{\boldsymbol{q}} = \left(J^T J + \lambda I\right)^{-1} J^T \dot{\boldsymbol{\xi}}_0 = J^{\#} \dot{\boldsymbol{\xi}}_0. \tag{5.29}$$

5.3.2 Specific DLS Algorithm for a Concentric-Tube-Robot

We now discuss a specific case of (5.28) used to teleoperate a three-tube concentric-tube robot prototype. In our implementation, we consider 5.27 in a discrete sense, using $\dot{\boldsymbol{q}}$ to represent the finite actuator displacements that we will command in the next time-step, and $\boldsymbol{v}_0$ to represent the desired linear and angular end-effector displacements to be achieved in the next time step. Assuming that we want to eliminate all tracking error in a single step, we can compute $\boldsymbol{v}_0$ as the difference between the commanded end-effector frame, g_c, and the most recent model-predicted frame, g_p by using the first-order approximation to the constant-twist solution as follows:

$$\boldsymbol{\xi}_0 = \left(g_p^{-1} g_c - I\right)^{\vee}. \tag{5.30}$$

We obtain the commanded frame g_c from a master input device by first defining a start time t_0 (when the operator "clutches in" by pressing a button). Then, as the master device moves, we apply its relative motion to the predicted frame at t_0, so that

$$g_c = g_p(t_0) g_m^{-1}(t_0) g_m, \tag{5.31}$$

where g_m is the master device frame. We note that this formulation gives $\boldsymbol{\xi}_0$ in coordinates of g_p, so the body-frame Jacobian should be used in (5.28). A schematic block diagram of our control framework is given in Fig. 5.5.

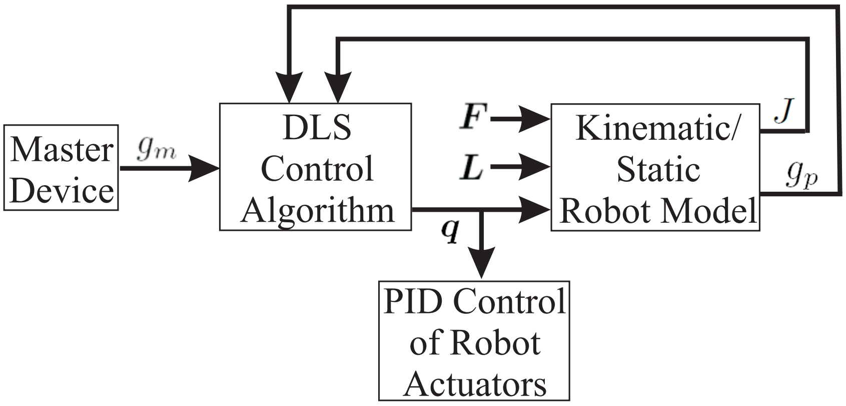

Figure 5.5: A schematic block diagram of the control framework.

In addition to the clutching, we have implemented motion scaling in order to allow the operator to make more precise movements with the robot end effector. The scaling is achieved by altering the commanded relative motion $g_m^{-1}(t_0)g_m$, which appears in (5.31). The relative position command is simply scaled by a multiplicative factor less than one, and the rotation matrix is scaled by first transforming to the axis-angle representation, scaling the angle by the same multiplicative factor, and then returning to the rotation matrix representation. The singularity at the identity in the map from rotation matrices to the axis-angle representation is handled by not performing the scaling for relative rotations are very small.

Our implementation includes the kinematic control and damping terms in (5.28). By iteratively testing our algorithm with various values for the weighting matrices W_0 and W_1 (setting $\boldsymbol{v}_1 = \mathbf{0}$ for damping), we have selected ones that perform well for our choice of units (we used meters for translation and radians for rotation) and our kinematic model loop rate of approximately 250 Hz.

Our end-effector tracking accuracy weighting matrix, W_0 is chosen such that 1

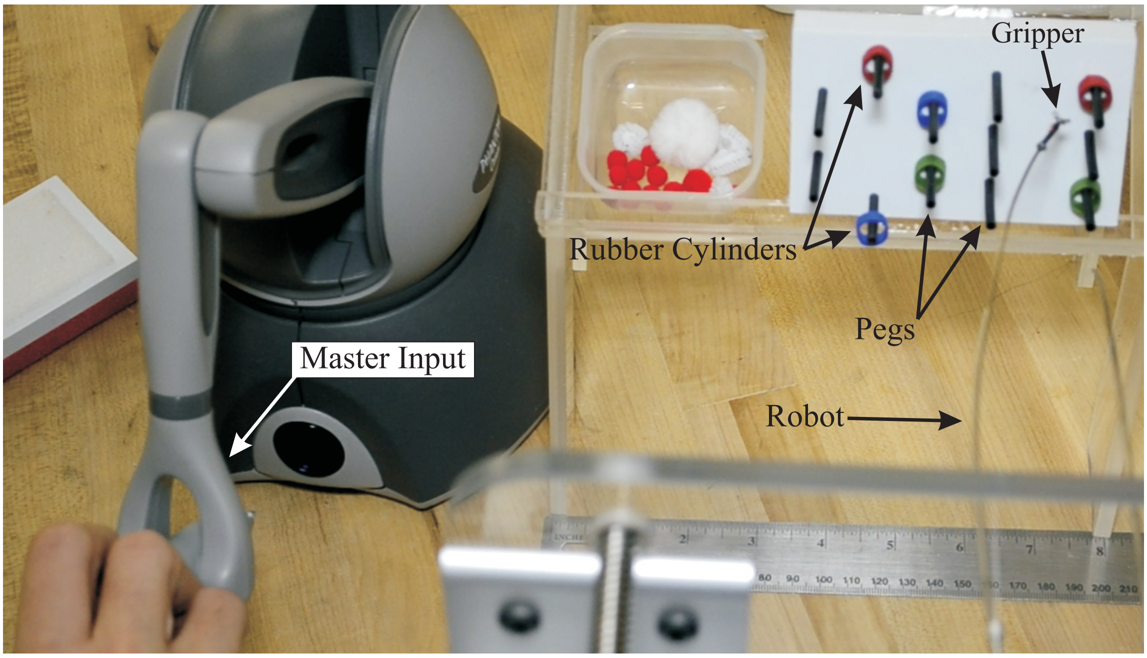

Figure 5.6: Experimental setup for our user study in which subjects completed a laparoscopic dexterity evaluation task. The task consisted of a pick-and-place excise where users removed the rubber cylinders from the pegs on the right, and placed them on the pegs arranged in a hexagon on the left. This was accomplished by teleoperating a prototype concentric-tube robot with a gripper-type end-effector.

mm of positional error is as "important" as 2° of angular error. This yields

$$W_0 = \begin{bmatrix} 10^6 & 0 & 0 & 0 & 0 & 0 \\ 0 & 10^6 & 0 & 0 & 0 & 0 \\ 0 & 0 & 10^6 & 0 & 0 & 0 \\ 0 & 0 & 0 & (90/\pi)^2 & 0 & 0 \\ 0 & 0 & 0 & 0 & (90/\pi)^2 & 0 \\ 0 & 0 & 0 & 0 & 0 & (90/\pi)^2 \end{bmatrix} \tag{5.32}$$

We choose W_1 such that 3° of rotational movement is damped as much as 1 mm of translational movement, and we weight the damping term by an additional factor of 40.

$$W_1 = 40 \begin{bmatrix} (60/\pi)^2 & 0 & 0 & 0 & 0 & 0 \\ 0 & (60/\pi)^2 & 0 & 0 & 0 & 0 \\ 0 & 0 & (60/\pi)^2 & 0 & 0 & 0 \\ 0 & 0 & 0 & 10^6 & 0 & 0 \\ 0 & 0 & 0 & 0 & 10^6 & 0 \\ 0 & 0 & 0 & 0 & 0 & 10^6 \end{bmatrix} \tag{5.33}$$

5.3.3 Experimental Validation

The above framework was implemented in C++ to teleoperate an active cannula robot. The robot chosen for the experiments consists of three Nitinol tubes, the physical parameters of which are given in Table 5.3. Each tube is composed of a straight segment followed by a circular arc, and the inner tube has a wire-actuated gripper affixed to the end. A Sensable PHANTOM Omni haptic display (Sensable, USA) device was used for the master input, with the two buttons on the stylus mapped to the teleoperation "clutch" and the gripper actuator.

Table 5.3: Tube parameters for the active cannula robot

	Inner	Middle	Outer
Straight Length [mm]	435.6	241.4	94.6
Curved Length [mm]	39.4	54.6	53.4
Curvature [mm^{-1}]	0.0070	0.0059	0.0032
Inner Radius [mm]	0.381	0.673	0.933
Outer Radius [mm]	0.584	0.842	1.162

The program is able to evaluate the kinematic model, including computation of the Jacobian and Compliance matrices, at approximately 200 to 300 Hz on a PC with a 2.5GHz Xeon processor, which we have observed to be fast enough for smooth teleoperation. The integration of the differential equations is performed by the Adams-Bashforth-Moulton 4th order predictor-corrector method, with the number of integration steps chosen to balance speed and model error. We used approximately one integration point for every three millimeters of arc length. The unloaded model of Chapter 3 can be solved runs considerably faster, but the model with tip loading will be useful for achieving accurate control when the robot is in contact with objects in its workspace or carrying loads via its gripper. For the experiments in this paper, we used our loaded model implementation with the tip load assumed to be zero.

Using this system we conducted an experimental trial that consisted of users moving small rubber cylinders from six initial pegs to six final pegs. This setup is shown in Fig. 5.6. The criteria evaluated were (1) the number of cylinders successfully moved and (2) the total time required to complete the transfers. Users were given some time before the experiment to adjust to the robot, but no formal training period was given. Data from three users was recorded. There was a 100% success rate in task completion; all users succeeded in moving all six cylinders to the desired locations without dropping them. The completion times for the individual trials were 270, 244, 965, and 237 seconds. The first two trials were performed by two individual users. The latter two trials were performed by the same user, who experienced a large improvement between the first and second trials, indicating that this user's initial acclimatization period may not have been sufficiently long before the first trial.

5.3.4 Control Conclusions

We have presented a Jacobian-based teleoperation method for concentric tube robots that enables external loads to be explicitly considered. The kinematic model and teleoperation framework presented were successfully implemented on hardware at a rate 200-300 Hz in our experiments, which includes a complete kinematic model computation (solution of the model boundary value problem) at every iteration of the control loop. Our user studies demonstrated that this teleoperation method with clutching and motion scaling enabled users to successfully complete laparoscopic dexterity assessment trials. We believe this teleoperation framework will enable many of the surgical applications foreseen for concentric-tube robots to be accomplished in practice. Future work will include evaluation studies in anthropomorphic phantoms and cadaveric specimens with physicians, to ensure that our teleoperation methods perform as well in surgical scenarios as they have in our initial benchtop evaluation studies.

5.4 Probabilistic Deflection-Based Force Sensing

In this section, we develop techniques for using sensed robot deflections to estimate external forces applied to the robot via the compliance matrix. Our approach is probabilistic, based on the well-known Extended-Kalman-Filter. We demonstrate in simulation the feasibility of determining unknown forces applied at the tip of a flexible tendon-actuated robot using only uncertain measurements of the tip pose and an uncertain kinematic-static model for the robot.

5.4.1 Problem Statement

We assume that a robot model exists in the form

$$\boldsymbol{p} = \boldsymbol{g}(\boldsymbol{\tau}, \boldsymbol{F}), \tag{5.34}$$

and that the robot's Jacobian J and compliance matrix C can be obtained, where $\boldsymbol{\tau}$ is a vector of actuator values, $\boldsymbol{F}$ is an externally applied force, and $\boldsymbol{p}$ is the robot's pose. We note that the force sensing methodology and algorithms developed herein can be used with any flexible robot as long as a model of this form exists for the robot's kinematics and static deformation.

Then, our problem statement can be formulated as follows: The state of the robot at a given time is defined by the vector $\boldsymbol{x} = [\boldsymbol{p} \quad \boldsymbol{\tau} \quad \boldsymbol{F}]^T$. Given an input Gaussian probability distribution (defined by μ_{input}, and Σ_{input}) which contains the current measurements of the pose and actuator values, a previous estimate of the force, and the uncertainty in those measurements and estimates, find the actual probability distribution for $\boldsymbol{x}$ (defined by μ_t, and Σ_t), which represents the best combined estimate of the actual pose, actuator values, and applied force, at time t, and the uncertainty in that estimation.

5.4.2 Simplified Example Robot Model

For our purposes in this section (demonstrating proof of concept for probabilistic force sensing), we will use a simplified model of a tendon-driven manipulator in our simulations by restricting the robot's motion to a plane, neglecting transverse shear strain and axial extension, and considering external loads only at the end effector. Specifically, this results in a special case of the general model developed in Chapter 4. It it is similar to models used in much of Gravagne and Walker's work [33, 37], where the robot structure consists of a planar elastica acted on by actuator torques

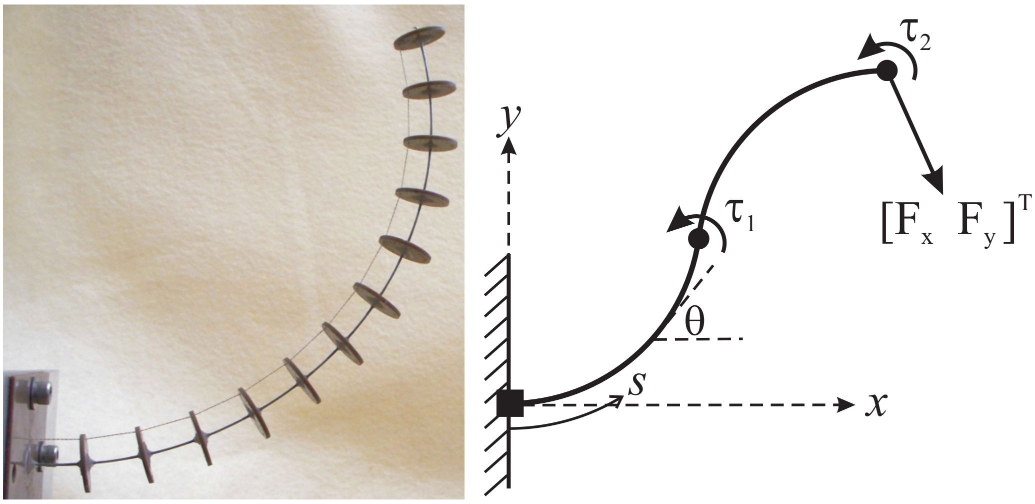

Figure 5.7: Left - A tendon driven continuum robot prototype. Right - Schematic of our planar robot model with actuation torques and tip forces.

at discrete points along the length. In the case where there are no external loads, this model reduces to the piecewise constant-curvature result that has been experimentally validated by several groups (see, e.g. [16, 33]) using robots driven by tendon wires, such as the one shown in Figure 5.7-right.

Our simplified robot model is pictured in Figure 5.7-right with its kinematic variables x, y, the tangent angle θ, actuator torques τ_1, τ_2, and external tip force components F_x and F_y. Assuming a linear constitutive law, the internal bending moment in the backbone at s is proportional to the curvature

$$\boldsymbol{m} = [0 \;\; 0 \;\; EIu] \tag{5.35}$$

where E is Young's modulus, I is the second moment of area of the backbone cross section about the z axis, and $u(s) \equiv \frac{d\theta}{ds}$ is the curvature of the rod. Assuming that there are no distributed loads, the internal force vector will be

$$\boldsymbol{n} = [F_x \;\; F_y \;\; 0], \tag{5.36}$$

and the backbone position is differentially related to the tangent angle θ as follows:

$$\begin{aligned}\boldsymbol{r} =& [x \ \ y \ \ 0],\\ \dot{\boldsymbol{r}} =& [\cos(\theta) \ \ \sin(\theta) \ \ 0].\end{aligned} \tag{5.37}$$

Thus, using (2.10), we arrive at a set of first order differential equations describing the shape of the robot as follows:

$$\begin{aligned}\dot{x} =& \cos(\theta)\\ \dot{y} =& \sin(\theta)\\ \dot{\theta} =& u\\ \dot{u} =& \frac{1}{EI}\left(F_x \sin(\theta) - F_y \cos(\theta)\right).\end{aligned} \tag{5.38}$$

The boundary conditions for this system are given by:

$$\begin{aligned}x(0) =& 0\\ y(0) =& 0\\ \theta(0) =& 0\\ u^{+}(L/2) =& u^{-}(L/2) - \frac{\tau_1}{EI}\\ u(L) =& \frac{\tau_2}{EI},\end{aligned} \tag{5.39}$$

where $-$ and $+$ superscripts indicate the value as approached from the left and the right.

The procedure for solving the boundary value problem to calculate the robot's end effector pose $\boldsymbol{p} = [x \quad y \quad \theta]^T$ as a function of the actuator values $\boldsymbol{\tau} = [\tau_1 \quad \tau_2]^T$ and applied loads $\boldsymbol{F} = [F_x \quad F_y]^T$ will hereafter be referred to as the forward kinematic mapping $\boldsymbol{p} = \boldsymbol{g}(\boldsymbol{\tau}, \boldsymbol{F})$.

The robot Jacobian relates how the pose changes with respect to changes in the actuation variables τ_1, and τ_2, as

$$J = \begin{bmatrix} \frac{\partial x}{\partial \tau_1} & \frac{\partial x}{\partial \tau_2} \\ \frac{\partial y}{\partial \tau_1} & \frac{\partial y}{\partial \tau_2} \\ \frac{\partial \theta}{\partial \tau_1} & \frac{\partial \theta}{\partial \tau_2} \end{bmatrix}. \tag{5.40}$$

Similarly, the compliance matrix relates kinematic changes to changes in the external loads F_x, and F_y, as

$$C = \begin{bmatrix} \frac{\partial x}{\partial F_x} & \frac{\partial x}{\partial F_y} \\ \frac{\partial y}{\partial F_x} & \frac{\partial y}{\partial F_y} \\ \frac{\partial \theta}{\partial F_x} & \frac{\partial \theta}{\partial F_y} \end{bmatrix}. \tag{5.41}$$

J and C can be efficiently obtained using the methods outlined in the first section of this chapter. These matrices are used in the prediction step of our Extended Kalman Filter algorithm to map an uncertainty in the actuator and force values to a resulting uncertainty in the pose, as discussed in the next section.

5.4.3 Robot Parameters and Uncertainty

In this section, we will define some specific robot parameters in order to investigate and visualize the effects of actuation and applied force uncertainty on the robot. For the prototype robot shown in Figure 5.7-left, its central backbone is a spring steel rod (ASTM A228) of length $L = 242$ mm and diameter $d = 0.8$ mm with a Young's modulus of $E = 210$ GPa. This results in a bending stiffness of $EI = .0042\ Nm^2$.

Suppose that $\boldsymbol{F} = [0 \quad 0]^T$ is known, and the uncertainty in $\boldsymbol{\tau} = [\tau_1 \quad \tau_2]^T$ is

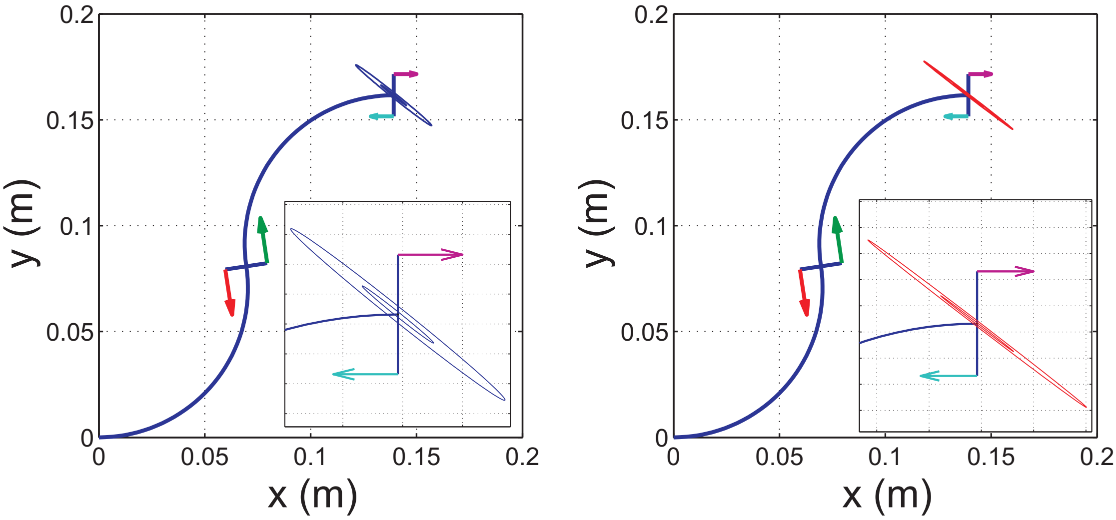

Figure 5.8: Left - The σ and 3σ Gaussian uncertainty ellipses for the tip position are plotted assuming the symmetric Gaussian distribution for τ_x and τ_y given in (5.42). Right - The σ and 3σ Gaussian uncertainty ellipses for the tip position are plotted assuming the symmetric Gaussian distribution for F_x and F_y given in (5.44).

Gaussian with mean and covariance,

$$\begin{aligned} \boldsymbol{\mu}_\tau =& [120 \quad -60]^T \quad mNm \\ \Sigma_\tau =& \begin{bmatrix} 1 & 0 \\ 0 & 1 \end{bmatrix} \quad (mNm)^2. \end{aligned} \tag{5.42}$$

Then, using a linearized approximation of the forward kinematic mapping (which is assumed to be a good approximation over the region of uncertainty) the resulting probability distribution for $\boldsymbol{p}$ will be Gaussian with mean and covariance given by the model prediction step of the conventional EKF, using the forward kinematic mapping and the Jacobian matrix,

$$\begin{aligned} \boldsymbol{\mu_p} =& \boldsymbol{g}(\boldsymbol{\mu}_\tau, \boldsymbol{0}) \\ \Sigma_p =& J\Sigma_\tau J^T. \end{aligned} \tag{5.43}$$

The eigenvectors of Σ_p provide the directions of the principal axes of an uncertainty ellipsoid for $\boldsymbol{p}$, and the square roots of the corresponding eigenvalues give the axis lengths for one standard deviation, σ, away from the mean. Plotting the resulting σ and 3σ uncertainty ellipses for the robot's tip position in Figure 5.8-left, we see that the resulting tip uncertainty is much larger in one direction, illustrating that the Jacobian is ill-conditioned.

Similarly, if $\boldsymbol{\tau}$ is known, and the uncertainty in the applied force is described by a Gaussian distribution with mean and covariance,

$$\begin{aligned} \boldsymbol{\mu}_F =& [0 \quad 0]^T \quad mN \\ \Sigma_F =& \begin{bmatrix} 100 & 0 \\ 0 & 100 \end{bmatrix} \quad mN^2, \end{aligned} \tag{5.44}$$

then the resulting mean and covariance for $\boldsymbol{x}$ are

$$\begin{aligned} \boldsymbol{\mu_p} =& \boldsymbol{g}(\boldsymbol{\mu}_\tau, \boldsymbol{\mu}_F, \mathbf{0}) \\ \Sigma_p =& C\Sigma_F C^T, \end{aligned} \tag{5.45}$$

and the resulting position ellipses are plotted in Figure 5.8-right. The ill-conditioned nature of J and C exhibited in both plots makes position-based force sensing a challenging task. A small amount of inaccuracy in the measurements of the tip location may lead to large errors in a force estimation depending on the direction. Thus, a probabilistic approach is needed to take these effects into account and quantify the uncertainty of any estimates that are based on measurements of the tip pose.

5.4.4 Extended Kalman Filter Approach

The conventional Extended Kalman Filter algorithm is based on a Hidden Markov Model for the robot, where the current robot state $\boldsymbol{x}_t$ is a function of the previous state

$\boldsymbol{x}_{t-1}$ and the current control input $\boldsymbol{u}_t$. The EKF determines a Gaussian probability distribution for the current state given the previous state distribution, the current control input, and the current measurement $\boldsymbol{z}_t$ of some quantities related to the states, i.e.,

$$(\boldsymbol{\mu}_t, \boldsymbol{\Sigma}_t) = \text{EKF}\left(\boldsymbol{\mu}_{t-1}, \boldsymbol{\Sigma}_{t-1}, \boldsymbol{u}_t, \boldsymbol{z}_t\right). \tag{5.46}$$

For a flexible serial robot, the probability distributions for the pose $\boldsymbol{p}$, actuators $\boldsymbol{\tau}$, and forces $\boldsymbol{F}$ should be dependent on each other because these quantities are related through the forward kinematic model. This leads us to define the following "state" vector,

$$\boldsymbol{x} = [\boldsymbol{p} \;\; \boldsymbol{\tau} \;\; \boldsymbol{F}]^T, \tag{5.47}$$

which will allow us to estimate the most likely combination of pose, actuator values, and tip forces simultaneously. In this formulation, there is no "control input", $\boldsymbol{u}_t$, since all of the kinematic model inputs have been included in the state, $\boldsymbol{x}_t$. We account for any modeling inaccuracy by assuming Gaussian uncertainty in $\boldsymbol{\tau}$), and we assume that noisy measurements of the tip pose and actuator values are available.

Specifically, this formulation leads to the following EKF algorithm:

$$
\begin{aligned}
(\boldsymbol{\mu}_t, \boldsymbol{\Sigma}_t) &= \mathrm{EKF}(\boldsymbol{\mu}_{input}, \boldsymbol{\Sigma}_{input}, \boldsymbol{z}_t) \\
\overline{\boldsymbol{\mu}} &= \begin{bmatrix} \boldsymbol{g}(\boldsymbol{\mu}(4:5), \boldsymbol{\mu}(6:7)) \\ \boldsymbol{\mu}(4:5) \\ \boldsymbol{\mu}(6:7) \end{bmatrix} \\
G &= \begin{bmatrix} 0_{3\times3} & J & C \\ 0_{4\times3} & \multicolumn{2}{c}{I_{4\times4}} \end{bmatrix} \\
\overline{\Sigma}_t &= G\Sigma_{input}G^T \\
K_t &= \overline{\Sigma}_t H_t^T (H_t \overline{\Sigma}_t H_t^T + Q_t)^{-1} \\
\boldsymbol{\mu}_t &= \overline{\boldsymbol{\mu}}_t + K_t(\boldsymbol{z}_t - \boldsymbol{h}(\overline{\boldsymbol{\mu}}_t)) \\
\Sigma_t &= (I - K_t H_t)\overline{\Sigma}_t
\end{aligned}
\tag{5.48}
$$

where H is the Jacobian matrix of the measurement function $\boldsymbol{z} = \boldsymbol{h}(\boldsymbol{x}) + \delta = H\boldsymbol{x} + \delta$,

$$
H = \begin{bmatrix} I_{5\times5} & 0_{5\times2} \end{bmatrix}, \tag{5.49}
$$

Q is the covariance matrix of the Gaussian measurement noise δ, (we used the one below in our simulations),

$$
Q = \begin{bmatrix}
1\ mm^2 & 0 & 0 & 0 & 0 \\
0 & 1\ mm^2 & 0 & 0 & 0 \\
0 & 0 & 1\ deg^2 & 0 & 0 \\
0 & 0 & 0 & 1\ (mNm)^2 & 0 \\
0 & 0 & 0 & 0 & 1\ (mNm)^2
\end{bmatrix}, \tag{5.50}
$$

$\boldsymbol{\mu}_{input}$ consists of the current measured values for x, y, θ, τ_1, and τ_2, and the previous estimate of the force components,

$$
\boldsymbol{\mu}_{input} = \begin{bmatrix} \boldsymbol{z}_t & \boldsymbol{\mu}_{t-1}(6:7) \end{bmatrix}, \tag{5.51}
$$

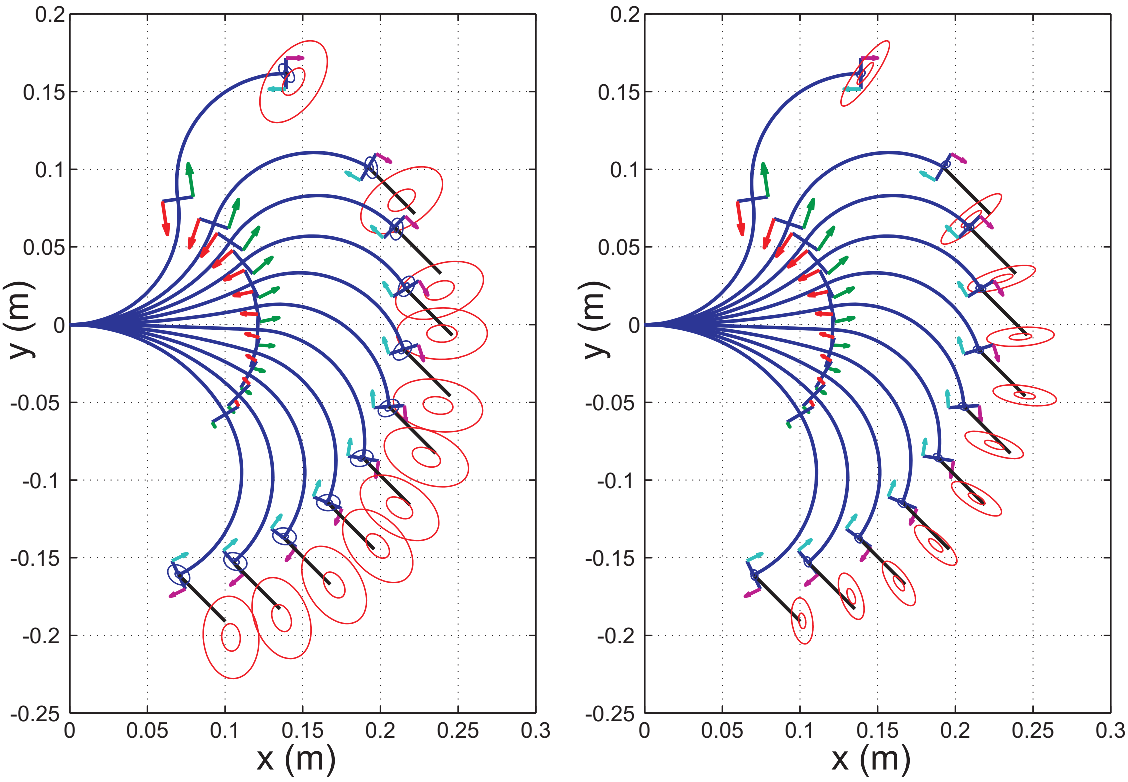

Figure 5.9: The applied tip force suddenly changes from zero to $[30 \;\; 30]^T \; mN$, after which point the robot's actuators continually move the robot. Left: The Q matrix from (5.50) is used. Right: the last ten measurements are averaged, and Q/10 is used in the algorithm.

and Σ_{input} is the prior state covariance which is given below for our simulation cases,

$$\Sigma_{input} = \begin{bmatrix} Q & 0 & 0 \\ 0 & 100 \; mN^2 & 0 \\ 0 & 0 & 100 \; mN^2 \end{bmatrix}. \tag{5.52}$$

5.4.5 Force Sensing Simulation Results

We tested the algorithm given in Section 5.4.4 with simulated noisy measurements of the tip coordinates and actuator values sampled from Gaussian distributions. Two test cases were performed. The first simulates a sudden change in the applied force from zero to $[30 \quad 30]^T \ mN$. After this, the forces remain constant but the robot's actuators continually move the robot. This case is illustrated in Figure 5.9. The robot's ground truth shape is plotted, along with a black vector at the tip which represents the magnitude and direction of the applied force. The blue ellipses are the σ and 3σ uncertainty ellipses for the tip position, and the red ellipses are the σ and 3σ uncertainty ellipses for the location of the tip of the force vector.

Figure 5.9-left shows the result when the Q defined in (5.50) is used. In Figure 5.9-right, the previous ten measurements were averaged at each time step, and the Q from (5.50) was accordingly replaced with $Q/10$ (since the variance of the sample mean of a Gaussian scales inversely with the number of samples). The result in Figure 5.9-right is higher accuracy, but the accuracy is more dependent on the direction, as shown by the smaller, flatter ellipses.

The second test case is shown in Figure 5.10-left, and 5.10-right. The actuators remain at fixed values, and the force was increased from 0 to $[100 \quad 100]^T \ mN$ in increments of $[20 \quad 20]^T \ mN$ at each time step. This represents a difficult scenario for force estimation, since the force is applied in a direction in which the robot is much stiffer (corresponding to the short axis of the ellipse in Figure 5.8-right). In this case, Figure 5.10-left shows that the measurement accuracy (Q in (5.50)) is insufficient to for good convergence of the EKF algorithm. In Figure 5.10-right, the previous 100 measurements were averaged at each time step, and $Q/100$ was used in the EKF. Thus, increasing the measurement accuracy helps the algorithm to converge more quickly in this scenario.

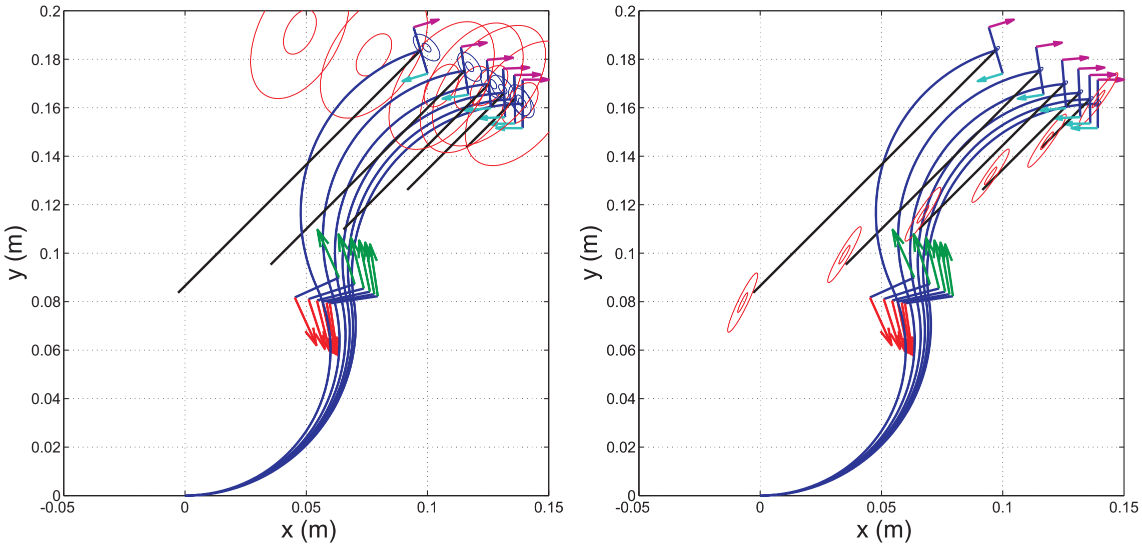

Figure 5.10: The applied tip force continually increases in a direction in which the robot is extremely stiff. Left: The Q matrix from (5.50) is used. Right: the last 100 measurements are averaged, and Q/100 is used in the algorithm.

5.4.6 Conclusions

The results in Section 5.4.5 provide an indication that our Extended Kalman Filter approach is suitable for position-based force sensing in flexible continuum robots, which, as we showed in Section 5.4.2, typically have ill-conditioned compliance matrices and Jacobians. There is much future work to be done, including developing rules for how accurate sensors must be for various kinds of robots in various configurations to achieve force sensing, and when it may not be possible in certain directions (this is analogous to the sensable and insensable wrenches seen in prior continuum robot work [102]). Also, experimental validation of sensed forces against known applied forces is essential, and experiments will be conducted in the near future. We also intend to extend this work to consider forces along the robot (not just at the tip), apply the method to continuum robots that are actuated by mechanisms other than tendons, and apply it to non-planar robot configurations. The work in this chapter serves as a first step toward these future goals.

Chapter 6

Conclusions and Future Work

This dissertation has presented several main contributions to the established, yet growing body of knowledge about continuum robots. Having laid foundations in modeling, control, and sensing for continuum robots, there are a variety of promising directions, outlined in the following sections, in which future research could proceed, using the work in this dissertation as a foundation.

6.1 Future Work in Modeling an Design

The models for concentric tube robots developed in Chapters 3 and 4 capture the essential physical phenomena governing the deformed shape of a general concentric-tube robot and have been shown to be accurate for several prototype robots. However, to obtain greater model accuracy, it may be necessary in the future to consider additional effects which are not represented in the current modeling frameworks. First, in practice there is usually a small amount of “non-tangency” of tube centerlines allowed by the clearance between concentric tubes. For robot configurations in which the inner tubes extend far beyond the ends of outer tubes, this effect may account for a significant portion of the total model error. Second, the effect of static friction between tubes introduces a hysteresis effect which, although usually small, may be non-negligible in some cases. Third, the effects of transverse shear deformation and extension could be incorporated, although these effects are minimal for robots constructed from long, slender, metal tubes. Fourth, incorporating more accurate, nonlinear, constitutive laws may be advantageous, especially for materials with known nonlinear constitutive behavior, like Nitinol.

Finding alternate model formulations may also be a fruitful area of future inquiry. In the case of the model in Chapter 5 for a general tendon-actuated robot, it would be useful to have an computationally efficient model which does not require the tendon tensions, but rather the tendon displacements as inputs. This could conceivably be accomplished by minimizing the potential energy functional subject to a tendon-length constraint. Real-time numerical implementation of the dynamic model presented in Chapter 5 would also be valuable towards facilitating inverse-dynamic control.

Future novel robot designs and architectures may also provide a perfect setting in which to apply rod-mechanics-based approaches like the ones presented in this work. Specifically, one can envision a hybrid robot which combines the actuation strategies of concentric tubes and embedded tendons. The dexterity of such a design may have the capability to exceed that of designs which use concentric tubes or tendons alone, and many of the results in this dissertation may be directly applied in order to generate a model for it. Furthermore, the optimization of workspace volume or dexterity measures by selecting design parameters has been relatively understudied for continuum robots, and the models in this dissertation should serve as efficient computational tools for studying these types of problems.

6.2 Future Work in Control and Sensing

In the area of control and sensing, the strategies outlined in Chapter 5 lay the groundwork for further work. One key idea which has not been considered is the bifurcation behavior of continuum robots described in [94]. Bifurcation may be addressed by a combination of design, planning, and control strategies. Specifically on-line detection and avoidance of potential bifurcation behavior during teleoperation may be possible by examining certain properties of the model and the robot Jacobian.

To facilitate using concentric-tube robots as steerable needles and to traverse tubular anatomical cavities, future work should also address insertion along desired paths (so that the body of the robot conforms or approximately conforms to the path at each point during the insertion). This problem may also be addressed by a combination of design, planning, and control.

The probabilistic approach to deflection-based force sensing may also be expanded and validated in future work. Implementation on concentric-tube robot hardware with external sensing, and incorporation of intrinsic wrench sensing into the proposed control framework are the necessary next steps toward a teleoperation system with intrinsic haptic feedback. In addition, the sensing of multiple loads located at different points along the continuum robot may be desirable to facilitate compliant interaction with sensitive structures.

6.3 Conclusions

This dissertation has presented 5 main contributions to the established, yet growing body of knowledge about continuum robots. In Chapter 3, we derived and experimentally validated two generalized, mechanics-based models for concentric-tube robots, which describe the shape of a general robot both in free-space under external loads. In Chapter 4, we derived and experimentally validated a new mechanics-based model for continuum robots actuated by tendon wires with general routing, and acted on by external loads. In Chapter 5, we developed a method for efficiently obtaining robot Jacobians and compliance matrices directly from a general set of model equations, and we showed how to use them to achieve inverse-kinematic control and probabilistic, deflection based force sensing.

The symbiotic relationship between robotics and continuum mechanics has had a long and fruitful history. We hope that the work in this dissertation provides a small contribution to this tradition that future work may build upon, and we anticipate that the overlap between the two will continue to generate both intriguing theoretical questions and solutions to practical problems in both fields.

Bibliography

[1] William F. Ames. *Nonlinear Ordinary Equations in Transport Processes.* Academic Press Inc., 1968.

[2] V. Anderson and R. Horn. Tensor arm manipulator design. *ASME Transactions*, 67-DE-57(2):1–12, 1967.

[3] Stuart S. Antman. *Nonlinear Problems of Elasticity.* Springer Science, 2nd edition, 2005.

[4] Stuart S. Antman and Russell C. Browne. *Applications of Methods of Functional Analysis to Problems in Mechanics: Local invertibility conditions for geometrically exact nonlinear rod and shell theories*, volume 503 of *Lecture Notes in Mathematics.* Springer Berlin / Heidelberg, 1976.

[5] T. Aoki, A. Ochiai, and S. Hirose. Study on slime robot: development of the mobile robot prototype model using bridle bellows. *IEEE International Conference on Robotics and Automation*, 3:2808 – 2813, 2004.

[6] S. D. Arati and I. D. Walker. Overview of damped least-squares methods for inverse kinematics of robot manipulators. *Journal of Intelligent Robotic Systems*, 14:43–68, 1995.

[7] K. S. Arun, T. S. Huang, and S. D. Blostein. Least-squares fitting of two 3-D point sets. *IEEE Transactions on Pattern Analysis and Machine Intellegence*, 9(5):698–700, 1987.

[8] Y. Bailly and Y. Amirat. Modeling and control of a hybrid continuum active catheter for aortic aneurysm treatment. *IEEE International Conference on Robotics and Automation*, pages 924–929, 2005.

[9] A. Bajo and N. Simaan. Finding lost wrenches: Using continuum robots for contact detection and estimation of contact location. *IEEE International Conference on Robotics and Automation*, pages 3666–3673, 2010.

[10] M. Bergou, M. Wardetzky, S. Robinson, B. Audoly, and E. Grinspun. Discrete elastic rods. *ACM Transactions on Graphics*, 27(3), 2008.

[11] R. L. Bishop. There is more than one way to frame a curve. *The American Mathematical Monthly*, 82(3):246–251, 1975.

[12] J.-Y. Bouguet. Camera calibration toolbox for matlab. `http://www.vision.caltech.edu/bouguetj/calib_doc /index.html`. Last acessed March 2010.

[13] M. Brand and M. B. Rubin. A constrained theory of a cosserat point for the numerical solution of dynamic problems of non-linear elastic rods with rigid cross-sections. *International Journal of Non-Linear Mechanics*, 42:216–232, 2007.

[14] R. Buckingham and A. Graham. Reaching the unreachable - snake arm robots. *International Symposium of robotics*, 2003. Available via OCRobotics Ltd. http//www.ocrobotics.com.

[15] D. B. Camarillo, C. R. Carlson, and J. K. Salisbury. Task-space control of continuum manipulators with coupled tendon drive. *11th International Symposium on Experimental Robotics*, 54:271–280, 2008.

[16] D. B. Camarillo, C. F. Milne, C. R. Carlson, M. R. Zinn, and J. K. Salisbury. Mechanics modeling of tendon-driven continuum manipulators. *IEEE Transactions on Robotics*, 24(6):1262–1273, 2008.

[17] G. S. Chirikjian. Hyper-redundant manipulator dynamics: A continuum approximation. *Advanced Robotics*, 9(3):217–243, 1995.

[18] G. S. Chirikjian. Kinematic synthesis of mechanisms and robotic manipulators with binary actuators. *Journal of Mechanical Design*, 117:573–580, 1995.

[19] G. S. Chirikjian and J. W. Burdick. A modal approach to hyper-redundant manipulator kinematics. *IEEE Transactions on Robotics and Automation*, 10(3):343–353, June 1994.

[20] G. S. Chirikjian and J. W. Burdick. Kinematically optimal hyper-redundant manipulator configurations. *IEEE Transactions on Robotics and Automation*, 11(6):794–806, December 1995.

[21] G.S. Chirikjian and A.B. Kyatkin. *Engineering Applications of Noncommutative Harmonic Analysis*. CRC Press, Boka Raton, FL, 2001.

[22] R. Cieslak and A. Morecki. Elephant trunk type elastic manipulator-a tool for bulk and liquid materials transportation. *Robotica*, 17:11–16, 1999.

[23] P. Dario, M. C. Carrozza, M. Marcacci, S. D'Attanasio, B. Magnami, and G. Megali O. Tonet. A novel mechatronic tool for computer-assisted arthroscopy. *IEEE Transactions on Information Technology in Biomedicine*, 4(1):15–29, 2000.

[24] W. Daum. A deflectable needle assembly, 2003. Patent 6,572,593.

[25] J. H. Davis and R. M. Hirschorn. A model for the embedded tendon control of a slender three-dimensional flexible robot link. *Dynamics and Control*, 4(2):185–208, April 1994.

[26] A. Degani, H. Choset, A. Wolf, T. Ota, and M. A. Zenati. Percutaneous intrapericardial interventions using a highly articulated robotic probe. In *IEEE / RAS-EMBS International Conference on Biomedical Robotics and Biomechatronics*, pages 7 – 12, February 2006.

[27] P. E. Dupont, J. Lock, and E. Butler. Torsional kinematic model for concentric-tube robots. *IEEE International Conference on Robtics and Automation*, pages 3851 – 3858, 2009.

[28] Pierre E. Dupont, Jesse Lock, Brandon Itkowitz, and Evan Butler. Design and control of concentric-tube robots. *IEEE Transactions on Robotics*, 26:209–225, 2010.

[29] R. Ebrahimi, S. Okazawa, R. Rohling, and S. E. Salcudean. Hand-held steerable needle device. *Medical Image Computing and Computer-Assisted Intervention*, 2003.

[30] K. Ediz and N. Olgac. Microdynamics of the piezo-driven pipettes in icsi. *IEEE Transactions on Biomedical Engineering*, 51(7):1262 – 1268, 2004.

[31] J. Furusho, T. Katsuragi, T. Kikuchi, T. Suzuki, H. Tanaka, Y. Chiba, and H. Horio. Curved multi-tube systems for fetal blood sampling and treatments of organs like brain and breast. *Journal of Computer Assisted Radiology and Surgery*, pages 223–226, 2006.

[32] I. A. Gravagne. *Design, Analysis and Experimentation: the Fundamentals of Continuum Robotic Manipulators*. PhD thesis, Clemson University, 2002.

[33] I. A. Gravagne, C. D. Rahn, and I. D. Walker. Large-deflection dynamics and control for planar continuum robots. *IEEE/ASME Transactions on Mechatronics*, 8(2):299–307, June 2003.

[34] I. A. Gravagne and I. D. Walker. Kinematic transformations for remotely-actuated planar continuum robots. *IEEE International Conference on Robotics and Automation*, pages 19–26, 2000.

[35] I. A. Gravagne and I. D. Walker. Kinematics for constrained continuum robots using wavelet decomposition. *Robotics 2000, Proc. 4th Int. Conf. and Exposition/Demonstration on Robotics for Challenging Situations and Environments*, pages 292–298, 2000.

[36] I. A. Gravagne and I. D. Walker. On the structure of minimum effort solutions with application to kinematic redundancy resolution. *IEEE Transactions on Robotics and Automation*, 19(6):855–863, December 2000.

[37] I. A. Gravagne and I. D. Walker. Manipulability, force, and compliance analysis for planar continuum robots. *IEEE Transactions on Robotics and Automation*, 18(3):263–273, June 2002.

[38] M. W. Hannan and I. D. Walker. Kinematics and the implementation of an elephant's trunk manipulator and other continuum style robots. *Journal of Robotic Systems*, 20(2):45–63, 2003.

[39] K. Harada, Z. Bo, S. Enosawa, T. Chiba, and M.G. Fujie. Bending laser manipulator for intrauterine surgery and viscoelastic model of fetal rat tissue. *IEEE International Conference on Robotics and Automation*, pages 611–616, 2007.

[40] S. Hirose. *Biologically Inspired Robots, Snake-Like Locomotors and Manipulators*. Oxford University Press, 1993.

[41] K. Ikuta, M. Tsukamoto, and S. Hirose. Shape memory alloy servo actuator system with electric resistance feedback and application for active endoscope. *IEEE International Conference on Robotics and Automation*, pages 427–430, 1988.

[42] G. Immega and K. Antonelli. The ksi tentacle manipulator. *IEEE International Conference on Robotics and Automation*, pages 3149–3154, 1995.

[43] M. Ivanescu, M.C. Florescu, N. Popescu, and D. Popescu. Coil function control problem for a hyperredundant robot. *IEEE/ASME International Conference on Advanced Intelligent Mechatronics*, pages 1–6, 2007.

[44] B. Jones, R. Gray, and K. Turlapati. Three dimensional statics for continuum robotics. *IEEE/RSJ International Conference on Intelligent Robots and Systems*, pages 2659–2664, 2009.

[45] B. A. Jones and I. D. Walker. Kinematics for multisection continuum robots. *IEEE Transactions on Robotics*, 22(1):43–55, 2006.

[46] B. A. Jones and I. D. Walker. Practical kinematics for real-time implementation of continuum robots. *IEEE Transactions on Robotics*, 22(6):1087–1099, Dec. 2006.

[47] S. Kehrbaum and J. H. Maddocks. Elastic rods, rigid bodies, quaternions and the last quadrature. *Philosophical Transactions: Mathematical, Physical and Engineering Sciences*, 355:21172136, 1997.

[48] R. Kumar, A. Kapoor, and R. H. Taylor. Preliminary experiments in robot/human cooperative microinjection. *IEEE/RSJ International Conference on Intelligent Robots and Systems*, pages 3186– 3191, 2003.

[49] C. Li and C. D. Rahn. Design of continuous backbone, cable-driven robots. *ASME Journal of Mechanical Design*, 124(2):265–271, 2002.

[50] J. Lock, G. Laing, M. Mahvash, and P. E. Dupont. Quasistatic modeling of concentric tube robots with external loads. *IEEE/RS*, pages 2325–2332, 2010.

[51] M. Loser. A new robotic system for visually controlled percutaneous interventions under X-ray or CT-fluoroscopy. Master's thesis, The Albert-Ludwig-University, Freiburg, Germany, 2002.

[52] H. Mochiyama and H. Kobayashi. The shape jacobian of a manipulator with hyper degrees of freedom. *IEEE International Conference on Robotics and Automation*, pages 2837–2842, 1999.

[53] Richard M. Murray, Zexiang Li, and S. Shankar Sastry. *A Mathematical Introduction to Robotic Manipulation.* CRC Press, Boca Raton, FL, 1994.

[54] Y. Nakamura, A. Matsui, T. Saito, and K. Yoshimoto. Shape-memory-alloy active forceps for laparoscopic surgery. *IEEE International Conference on Robotics and Automation*, pages 2320–2327, 1995.

[55] R. Ohta. Results of R&D on catheter-type micromachine. *International Symposium on Micromechatronics and Human Science*, pages 5–12, 2001.

[56] K. Osuka and H. Kitajima. Development of mobile inspection robot for rescue activities: MIORA. *IEEE/RSJ International Conference on Intelligent Robots and Systems*, pages 3373–3377, 2003.

[57] E. Paljug, T. Ohm, and S. Hayati. The JPL serpentine robot: a 12-DOF system for inspection. *IEEE International Conference on Robotics and Automation*, pages 3143–3148, 1995.

[58] J. Park and W.-K. Chung. Geometric integration on euclidean group with application to articulated multibody systems. *IEEE Transactions on Robotics*, 21(5):850–863, 2005.

[59] L. Phee, D. Accoto, A. Menciassi, C. Stefanini, M. C. Carrozza, and P. Dario.

Analysis and development of locomotion devices for the gastrointestinal tract. *IEEE Transactions on Biomedical Engineering*, 49(6):613–616, 2002.

[60] G. Robinson and J. B. C. Davies. Continuum robots – a state of the art. *IEEE International Conference on Robotics and Automation*, pages 2849–2854, 1999.

[61] D. C. Rucker, J. M. Croom, and R. J. Webster III. Aiming surgical lasers with an active cannula. *ASME Journal of Medical Devices*, page 027506, 2009.

[62] D. C. Rucker, B. A. Jones, and R. J. Webster III. A geometrically exact model for externally loaded concentric-tube continuum robots. *IEEE Transactions on Robotics*, 26:769–780, 2010.

[63] D. C. Rucker, B. A. Jones, and R. J. Webster III. A model for concentric tube continuum robots under applied wrenches. *IEEE International Conference on Robtics and Automation*, pages 1047–1052, 2010.

[64] D. C. Rucker and R. J. Webster III. Mechanics-based modeling of bending and torsion in active cannulas. *IEEE RAS/EMBS International Conference on Biomedical Robotics and Biomechatronics*, pages 704–709, 2008.

[65] D. C. Rucker and R. J. Webster III. Parsimonious evaluation of concentric-tube continuum robot equilibrium conformation. *IEEE Transactions on Biomedical Engineering*, 56(4):2308 – 2311, 2009.

[66] D. C. Rucker and R. J. Webster III. Mechanics of continuum robots with general tendon routing paths under external loading. *12th International Symposium on*

Experimental Robotics 2010, Springer Tracts in Advanced Robotics, 2010. (In Press).

[67] D. C. Rucker and R. J. Webster III. Computing jacobians and compliance matrices for externally loaded continuum robots. *IEEE International Conference on Robotics and Automation*, 2011.

[68] D. C. Rucker and R. J. Webster III. Deflection-based force sensing for continuum robots: A probabilistic approach. *IEEE/RSJ International Conference on Intelligent Robots and Systems*, pages 3764–3769, 2011.

[69] D. C. Rucker and R. J. Webster III. Statics and dynamics of continuum robots with general tendon routing and external loading. *Transactions on Robotics*, IEEE Early Access:DOI: 10.1109/TRO.2011.2160469, 2011.

[70] D. C. Rucker, R. J. Webster III, G. S. Chirikjian, and N. J. Cowan. Equilibrium conformations of concentric-tube continuum robots. *International Journal of Robotics Research*, 29:1661–1683, 2010. (In Press).

[71] D. C. Rucker and Robert J. Webster III. Mechanics of bending, torsion, and variable precurvature in multi-tube active cannulas. *IEEE International Conference on Robotics and Automation*, pages 2533–2537, 2009.

[72] P. Sears and P. E. Dupont. A steerable needle technology using curved concentric tubes. *IEEE/RSJ International Conference on Intelligent Robots and Systems*, pages 2850–2856, 2006.

[73] P. Sears and P. E. Dupont. Inverse kinematics of concentric tube steerable needles. *IEEE International Conference on Robotics and Automation*, pages 1887–1892, 2007.

[74] B. Siciliano and O. Khatib, editors. *Springer Handbook of Robotics.* Springer, 2008.

[75] N. Simaan, R. H. Taylor, and P. Flint. High dexterity snake-like robotic slaves for minimally invasive telesurgery of the upper airway. *MICCAI 2004 - the 7th International Conference on Medical Image Computing and Computer-Assisted Intervention*, pages 17–24, 2004.

[76] N. Simaan, K. Xu, W. Wei, A. Kapoor, P. Kazanzides, P. Flint, and R. Taylor. Design and integration of a telerobotic system for minimally invasive surgery of the throat. *International Journal of Robotics Research special issue on medical robotics*, 28:1134–1153, 2009.

[77] N. Simaan, J. Zhang, J.T. Roland Jr., and S. Manolidis. Steerable continuum robot design for cochlear implant surgery. *IEEE International Conference on Robotics and Automation (ICRA) Workshop*, 2010.

[78] J. C. Simo and L. Vu-Quoc. A three-dimensional finite strain rod model. part ii. computational aspects. *Computational aspects, Comput. Meth. Appl. Mech. Eng.*, 58:79116, 1986.

[79] Y. Sun and B. J. Nelson. Biological cell injection using an autonomous micro-

robotic system. *The International Journal of Robotics Research*, 21(10-11):861–868, 2002.

[80] K. Suzumori, S. Wakimoto, and M. Takata. A miniature inspection robot negotiating pipes of widely varying diameter. *IEEE International Conference on Robotics and Automation*, pages 2735–2740, 2003.

[81] M. Takahashi, I. Hayashi, N. Iwatsuki, K. Suzumori, and N. Ohki. The development of an in-pipe microrobot applying the motion of an earthworm. *International Symposium on Micro Machine and Human Science*, pages 35–40, 1994.

[82] M. Terayama, J. Furusho, and M. Monden. Curved multi-tube device for path-error correction in a needle-insertion system. *International Journal of Medical Robotics and Computer Assisted Surgery*, 3(2):125–134, 2007.

[83] M. W. Thring. *Robots and Telechirs; Manipulators with Memory; Remote Manipula- tors; Machine Limbs for the Handicapped.* Ellis Horwood, 1983.

[84] D. Trivedi, A. Lotfi, and C.D. Rahn. Geometrically exact models for soft robotic manipulators. *IEEE Transactions on Robotics*, 24:773 – 780, 2008.

[85] Deepak Trivedi, Christopher D. Rahn, William M. Kierb, and Ian D. Walker. Soft robotics: Biological inspiration, state of the art, and future research. *Applied Bionics and Biomechanics*, 5(3):99 – 117, September 2008.

[86] H. Tsukagoshi, A. Kitagawa, and M. Segawa. Active hose: an artifcial elephant's

nose with maneuverability for rescue operation. *IEEE International Conference on Robotics and Automation,*, 3:2454 – 2459, 2001.

[87] Y. Wakahara, K. Asano, and T. Tsuchihashi. A computer aided manipulation system for a multijoint inspection robot. *Transactions of the American Nuclear Society*, 47:455–456, 1984.

[88] C. W. Wampler II. Manipulator inverse kinematic solutions based on vector formulations and damped least-squares methods. *IEEE TRANSACTIONS ON SYSTEMS, MAN, AND CYBERNETICS*, 16:93–101, 1986.

[89] R. J. Webster III. *Design and Mechanics of Continuum Robots for Surgery.* Mechanical engineering, Johns Hopkins University, Baltimore, MD, December 2007. PhD Thesis.

[90] R. J. Webster III and B. A. Jones. Design and kinematic modeling of constant curvature continuum robots: A review. *International Journal of Robotics Research*, 29:1661–1683, 2010.

[91] R. J. Webster III, J. S. Kim, N. J. Cowan, G. S. Chirikjian, and A. M. Okamura. Nonholonomic modeling of needle steering. *International Journal of Robotics Research*, 25(5/6):509–526, May/June 2006.

[92] R. J. Webster III, A. M. Okamura, and N. J. Cowan. Toward active cannulas: Miniature snake-like surgical robots. *IEEE/RSJ International Conference on Intelligent Robots and Systems*, pages 2857–2863, 2006.

[93] R. J. Webster III, J. M. Romano, and N. J. Cowan. Kinematics and calibration of active cannulas. *IEEE International Conference on Robotics and Automation*, pages 3888–3895, 2008.

[94] R. J. Webster III, J. M. Romano, and N. J. Cowan. Mechanics of precurved-tube continuum robots. *IEEE Transactions on Robotics*, 25(1):67–78, 2009.

[95] P. M. White. Stress induced interposed connector, 2001. Patent 6,257,593.

[96] D. E. Whitney. The mathematics of coordinated control of prosthetic arms and manipulators. *ASME J. Dyn. Syst., Meas. Control*, 94:303–309, 1972.

[97] J.F. Wilson and U. Mahajan. The mechanics of positioning highly flexible manipulator limbs. *J. Mechanisms, Transmissions, Autom. Des.*, 111:232–237, 1989.

[98] A. Wolf, H. B. Brown, R. Casciola, M. Schwerin A. Costa, E. Shamas, and H. Choset. A mobile hyper redundant mechanism for search and rescue tasks. *IEEE/RSJ International Conference on Intelligent Robots and Systems*, pages 2889–2895, 2003.

[99] K. Xu and N. Simaan. Actuation compensation for flexible surgical snake-like robots with redundant remote actuation. *IEEE International Conference on Robotics and Automation*, pages 4148–4154, 2006.

[100] K. Xu and N. Simaan. An investigation of the intrinsic force sensing capabilities of continuum robots. *IEEE Transactions on Robotics*, 24(3):576–587, 2008.

[101] K. Xu and N. Simaan. Analytic formulation for kinematics, statics and shape restoration of multi-backbone continuum robots via elliptic integrals. *ASME Journal of Mechanisms and Robotics*, 2(1):011006–1 to 011006–13, 2010.

[102] K. Xu and N. Simaan. Intrinsic wrench estimation and its performance index for multisegment continuum robots. *IEEE Transactions on Robotics*, 26(3):555–561, 2010.

[103] G. Zadno and T. Duerig. Linear and non-linear superelasticity in niti. *MRS International Meeting on Advanced Materials*, 9:201–209, 1989.